Correlations between the standard and alternative definitions of the beam quality factor

by

Hencharl Johan Strauss

Thesis presented in partial fulfilment of the requirements for the degree of Master of Science at the University of Stellenbosch

Supervisors: **Prof. H.M. von Bergmann**
Dr E.G. Rohwer

April 2005

Declaration

I, the undersigned, hereby declare that the work contained in this thesis is my own original work and that I have not previously in its entirety or in part submitted it in any university for a degree.

Signature

Date

Abstract

The beam quality factor (M^2) of a laser is important because it describes both the quality of a laser beam as well as its propagation. Particular applications require that the beam radii (from which the M^2 factor is determined) be defined in a specific way. The International Standards Organisation (ISO) recently standardised the theoretically correct, but practically difficult second moment definition of the beam radius.

This thesis aims to establish correlations between the second moment definition and other more practical definitions. Chapter 2 presents a systematic introduction of moment theory for general beams. Beam centre and radius definitions as well as beam classification are derived by means of second and mixed moments. In Chapter 3 simple laser beams are modelled by means of a resonator approach. The infinite number of solutions of this model is called Gaussian solutions, which are found to be different for rectangular and cylindrical symmetric resonators. The zero order solution for both symmetries is identified as the ideal solution to which all others can be compared to for quality determinations. Chapter 4 presents different beam scanning devices, beam radius definitions and correlations between these definitions. The theoretical basis for a new correlation theory is also given. Chapter 5 describes programs and computations used to verify existing correlation methods and to calculate correlation factors for a newly proposed theory. Chapter 6 presents the results of the computations for both circular and rectangular symmetric beams. The ISO's correlation theories are tested first. Newly proposed correlation functions between the second moment and alternative definitions as well as theoretical error graphs are given for various beams. A novel method to correlate several important beam subclasses is also presented. Chapter 7 describes the experimental setup, automation software and post processing techniques that were used to characterise a modified CO_2 TEA laser. It is further shown how the theory developed in previous chapters could be applied to the experimental data. Chapter 8 presents the experimental results of the beam characterisation measurements performed on two different beams that emanated from the CO_2 TEA laser. Existing and newly developed correlation theories are applied to the experimental data and the corresponding results are compared. In Chapter 9, conclusions and suggestions with respect to the initial aims identified in the first chapter are made. Several suggestions for future work are also made.

Samevatting

Die bundel kwalitietsfaktor (M^2) is baie belangrik omdat dit beide die kwaliteit en voortplanting van ‘n laser bundel beskryf. Bundel radiusse (waarvan die M^2 faktor bepaal word) word verskillend gedefinieer vir spesifike toepassings. Die teoreties korrekte, maar minder praktiese tweede moment definisie is onlangs deur die Internasionale Standaard Organisasie (ISO) gestandariseer.

Hierdie tesis se hoofdoel is om die tweede moment definisie en ander meer praktiese definisies te korreleer. Hoofstuk 2 stel die moment teorie van bundels sistematies bekend. Dit word gewys hoe die senter en radius van ‘n bundel deur tweede en gemengde momente gedefinieer kan word. In Hoofstuk 3 word laser bundels gemodeleer deur middel van resonator aanslag. Die oneindige aantal oplossings wat verkry word heet Gaussiese oplossings en is verskillend vir reghoekige en silindriese simmetriese resonators. Dit word gewys dat die ideale bundel, waarmee alle ander bundels vergelyk word, die zero orde oplossing van beide simmetrieë is. Hoofstuk 4 stel verskillende bundel skanderings apparaat, bundel radius definisies en korrelasies tussen die definisies bekend. Die teoretiese basis vir ‘n nuwe korrelasie teorie word ook gegee. Hoofstuk 5 beskryf die rekenaarprogramme en berekeninge wat gebruik word om huidige korrelasie teorie mee te toets asook om nuwes mee te skep. Hooftuk 6 gee die resultate van die berekeninge van die rekenaarprogramme vir beide reghoekig en silindriese simmetrie. Die ISO se korrelasies word eerste getoets voordat nuwe teorieë bekend gestel word. In Hoofstuk 7 word die eksperimentele opstelling, outomisasie sagteware en post-prosessering tegnieke gewys wat gebruik was om ‘n aangepaste CO_2 TEA laser te karakteriseer. Verder word dit gewys hoe die teorie wat in voorafgaande hoofstukke ontwikkel is op eksperimentele data toegepas kan word. Hoofstuk 8 gee die eksperimentele resultate van die bundel karakterisering van twee verskillende bundels vanaf die CO_2 TEA laser. Bestaande en nuwe korrelasie metodes word gebruik om die bundels te korreleer en die resultate van elke metode word dan met mekaar vergelyk. In Hoostuk 9 word afleidings gemaak. Daar word ook voorstelle gemaak vir potensiële toekomstige werk.

Acknowledgements

I wish to express my sincere gratitude to

Prof. H.M. von Bergmann for supervising and guiding me through the many challenges the experimental and computational work presented.

Mr. T Stehmann for his support and motivation without which I probably never would have finished this thesis.

My parents and brother for their support, encouragement and for providing the personal computer that was used in the computational part of the project.

Dr. C.M. Steenkamp for assisting me with the layout of this thesis.

Mr. M. Bartolini for his speedy development of the various electronic and automation parts of the project.

Mr U.G.K. Deutschlander for his help and expertise at all stages of the project at all times of the day and night.

Mr R.T. Gordon who always provided help and support and his attentiveness to our needs.

The personnel of the mechanical workshop of the Physics Department who manufactured so many experimental apparatus and replacement parts for the laser.

Scientific Development and Integration (SDI) for providing financial support and the CO_2 TEA laser.

All the personnel and fellow students of the Physics Department and Laser Group for the years of support and friendship.

Contents

Chapter 1

Problem statement and overview

1.1 Introduction and problem statement

Laser researchers have sought ways to measure the spatial properties of beams since T. H. Maiman first demonstrated the laser in 1960. The first simplistic methods used for the spatial evaluation of laser beams were burn-paper marks, acrylic mode burns and direct viewing of diffuse reflected beams [10]. These methods did not, however, provide reproducible results.

In answer to this problem, mechanical scanning devices such as knife-edges, slits and variable apertures were developed to obtain accurate beam profiles. Charged coupled device cameras (CCD cameras) currently dominate the laser characterisation market, but still employ virtual slits or knife-edges in their post-analysis programs [9], [49].

The definition of the beam radius, rather than its accurate measurement, has been the main point of contention over the years. It is extremely important to use correct and accurate beam radii since they determine the energy density, divergence and quality of laser beams. Good quality lasers can be focussed to smaller spot sizes, their depth of focus is longer, they can be collimated for longer distances and their energy density distribution has a Gaussian distribution. The beam quality therefore needs to be determined accurately and reliably by using a standard definition of the beam radius. Several attempts have been made over the years to agree on such a standard definition [7], [8],[24], [27], [46], [56].

Different groups contended for years about which definition is best because different definitions are best suited for specific applications. The second moment definition is excellent for assessment of the beam quality and provides a sound theoretical base for all types of beams, but gives beam radii that have no connection with the beam energy that they contain.

An extensive introduction to this powerful theory is given later in this thesis because it can describe an immense variety of beams. Energy density definitions accurately track nodes and other features in beams' energy density profiles, but give inconsistent radii when the energy is concentrated in the wings of the beam. Energy content definitions are the only definitions from which the important energy flux parameter can be calculated, but give inconsistent values for the theoretical beam quality or M^2 factor. The definition of the beam radius must therefore be chosen according to the information that is required. Because of this controversy laser beam radii were only standardized in 1999 (almost forty years after Maiman) by the International Standards Organisation (ISO) using only the theoretical second moment definition (ISO 11146). The organisation largely ignored the other more practical definitions stating only that "[o]ther definitions of beam widths and divergence angles may be helpful for other applications, but must be shown to be equivalent to the second moment definition" [24].

In many instances, the second moment radii cannot be obtained directly. Siegman [46] showed that there is an unavoidable uncertainty when the second moment definition radius is determined from a knife-edge energy level radius. People have tried for years to minimise this correlation error. The ISO provided experimentally obtained correlation functions between the second moment and alternative definitions (the slit, knife-edge and variable aperture definitions) without stating that each must be used for different applications. These correlation functions were obtained by Johnston [27] from only a few measurements and were hardly shown to be representative of most lasers. The ISO also failed to mention the inevitable correlation error and in fact abandoned the goal of finding a general correlation method with little or no errors when they adopted Johnston's correlation method.

Siegman took the correlation error into account [46] when he used a graphical approach to determine the optimum knife-edge clip-level and factor for correlating the second moment and knife-edge definitions. His method was more general than the ISO's because his approach was theoretical. Due to the large number of beams he used it was also valid for a larger range of quality values. However, Siegman's graphical method largely ignored practical beams, opting rather for theoretically pure "unmixed" beams. The ISO specifically took this mixing into account even though it was only for a few beams.

1.2 Aims

This thesis aims to develop a comprehensive beam correlation theory that incorporates previous methods and provides a better understanding of the relations between different beam radius definitions for a broad range of laser systems.

Secondly this thesis aims to modify and characterise an experimental CO_2 transverse excited atmospheric (TEA) laser [40] for material processing using a knife-edge method. This part of the project therefore had a dual focus. The beam quality of a laser source had to be accurately known in order to evaluate the modified resonator. Accurate values of the beam's energy distribution were also needed for material processing applications. A newly developed correlation theory can be used to obtain both these goals.

No beam scanner was available to characterise the laser, necessitating the development of one. The mechanical knife-edge scanning method that was chosen, made the scanner wavelength and power independent so that it could potentially be used for other pulsed laser systems in the department. The successful development and demonstration of this beam scanner became another aim of this thesis.

1.3 Terms of Reference

Terminology used in this thesis relates to pulses since CO_2 TEA lasers operate in a pulsed mode. Terms that will be used a lot are energy density and energy. This is because the integrated energy per pulse is usually measured when characterising a beam. The power of a laser beam is the amount of energy in J per s that it transfers to a power meter. Power and power density (intensity) are therefore more commonly used to describe continuous wave (CW) laser characteristics.

Many articles and books use beam diameters instead of radii. This thesis will use beam radii and beam diameters will only be used when material specific to a particular reference is presented.

Chapter 2

General beam theory

The objective of this chapter is to give a systematic introduction to a comprehensive beam theory, called moment theory. This theory is so widely applicable that it can describe both coherent and non-coherent beams.

2.1 Moment theory

2.1.1 First order moments

The first order spatial energy density moment for a two-dimensional slice in the x and y transverse directions of a beam somewhere along its propagation direction is given by the following integral [24, [23]:

$$\langle x \rangle = \frac{1}{P} \int_{-\infty}^{+\infty} \int_{-\infty}^{+\infty} x \cdot I(x, y, z) dx dy \tag{2.1}$$

with P the total energy of the beam

$$P = \int_{-\infty}^{+\infty} \int_{-\infty}^{+\infty} I(x, y) dx dy \tag{2.2}$$

x an arbitrary transverse direction and $I(x, y, z)$ the energy density distribution.

The first angular energy density moment is given by the following integral:

$$\langle q_x \rangle = \frac{1}{P} \int_{-\infty}^{\infty} \int_{-\infty}^{\infty} q_x I_{Fourier}(q_x, q_y) dq_x dq_y \tag{2.3}$$

with $I_{Fourier}(q_x, q_y)$ the Fourier transform of the energy density distribution, l the wavelength and q_x the direction of the wave front from an arbitrary x direction.

$\langle x^{1st} \rangle$ is defined as the *centre of mass* of a slice of a beam profile. This is identical to the definition of the centroid of an area [36]. $\langle q_x \rangle$ is defined as the *propagation direction* of this centre of mass in the x-z plane. A beam can be simplified to a ray, which obeys the ABCD law of geometrical optics, by using the centre of mass and propagation direction of several slices in the propagation direction [23]. This reduction can be seen in Figure 2-1, which illustrates the direction $\langle q_x \rangle$ of a typical beam and the centre of mass $\langle x^{1st} \rangle$ of one slice.

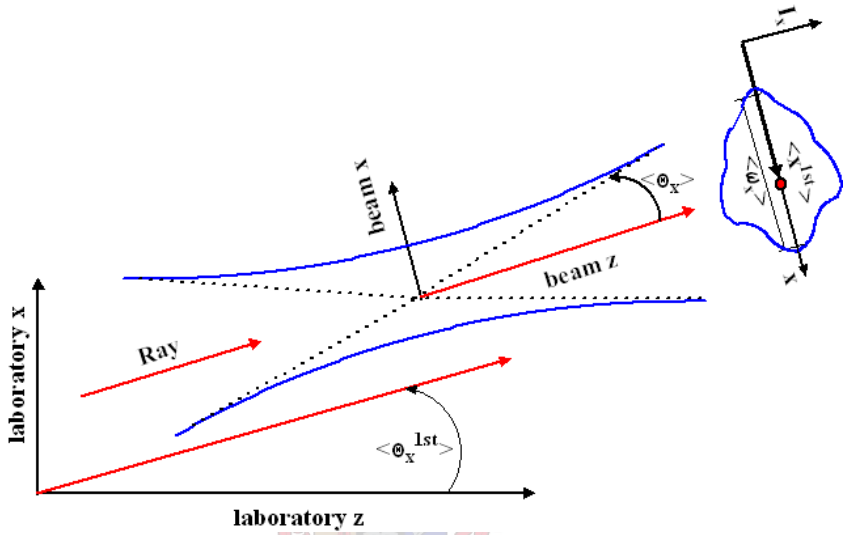

Figure 2-1: Illustration of first and second order beam moments of a three-dimensional beam.

2.1.2 Second order moments

The second order spatial intensity moment is defined in rectangular symmetry as [23], [24]

$$\langle x^2 \rangle(z) = \sqrt{\frac{\int_{-\infty}^{+\infty}\int_{-\infty}^{+\infty} \left(x - \langle x \rangle\right)^2 \cdot I(x,y)dxdy}{P}} \tag{2.4}$$

and in cylindrical symmetry* as [24]:

$$\langle r^2 \rangle(z) = \sqrt{\frac{\iint r^2 \cdot I(r) r dr dj}{P}} \tag{2.5}$$

* In this thesis rectangular symmetry will mostly be used to define quantities. Quantities are also defined in circular symmetry if they are required in future chapters. The arbitrary x direction will also be used to present most definitions.

$\langle x^2 \rangle$ can be equated with the moment of inertia of an area with the same shape as the beam profile [36]. A beam radius can be defined as

$$\langle w_x \rangle = 2 \times \langle x^{2nd} \rangle \text{ or } \langle w_r \rangle = 2 \times \langle r^{2nd} \rangle . \tag{2.6}$$

Beam radii can be determined at any position along the beam propagation direction by integrating Equation (2.4) or (2.5) over the two-dimensional energy density profiles.

The second order angular intensity moment is defined as

$$\langle q_x^2 \rangle = \sqrt{\frac{\int_{-\infty}^{\infty}\int_{-\infty}^{\infty} \left(q_x - \langle q_x^{1st} \rangle\right)^2 \cdot l^2 I_{Fourier}(q_x, q_y) dq_x dq_y}{P}} . \tag{2.7}$$

The far field divergence angle of the beam in the x direction is defined as twice this value [24]:

$$\langle \Theta_x \rangle = 2 \times \langle q_x^2 \rangle . \tag{2.8}$$

This divergence in one of the principle axes can be practically determined with the following equation

$$\langle \Theta_x \rangle = \lim_{z \to \infty} \frac{\langle w_x(z) \rangle}{z} . \tag{2.9}$$

Figure 2-1 also illustrates a general beam's second moment radius and divergence.

2.1.3 Mixed Moments

Mixed moments arise because the electric field distributions $E(x, y)$ are described by complex functions. The exact mathematical definitions of the mixed moments can be found on page 100 of reference 23.

The physical attributes of the mixed moment are as follows [18], [23].

- $\langle x \; q_x \rangle$ is related to the radius of curvature
- $\langle x \; q_y \rangle$ describes the rotation of the beam while propagating
- $\langle x \; y \rangle$ characterises the orientation of the near field energy density ellipse with respect to the reference frame
- $\langle q_x q_y \rangle$ characterises the orientation of the far field energy density ellipse with respect to the reference frame.

The last three attributes are illustrated in Figure 2-2.

Only $\langle x\, q_x \rangle$, which is related to the radius of curvature, is found in beams originating from simple laser resonators.

a

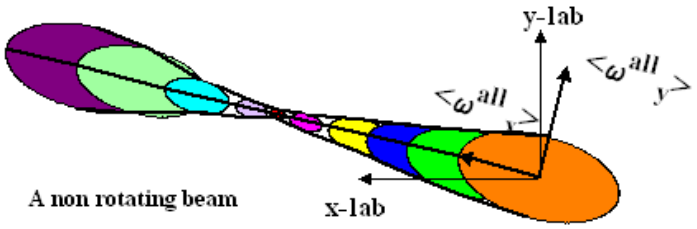

b

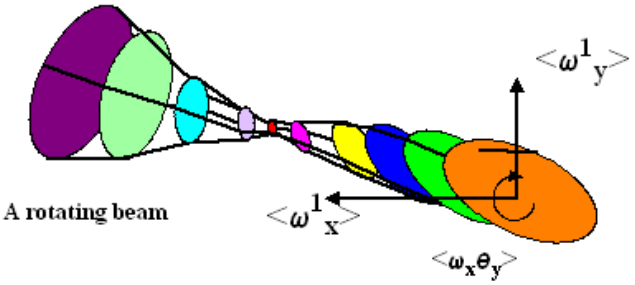

c

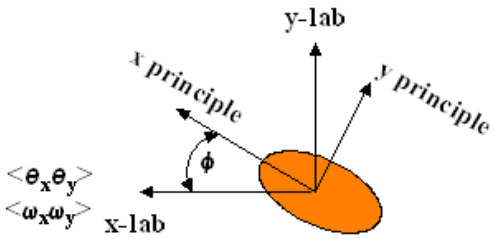

Figure 2-2 :Illustration of the mixed moments. (a) shows a non-rotating beam, (b) a rotating beam and (c) the near field ellipse orientation to the reference frame.

2.1.4 The general ABCD law

The three moment types of Sections 2.1.1 to 2.1.3 can now be combined to fully describe beams in three dimensions using the general ABCD law. The general ABCD law for one-dimensional optics is only valid for beams when the moment definition is used to define their beam properties. This is mainly because beams defined by moment theory can be simplified to rays (Section 2.1.1) and can also be proved by applying the Collins integral to the definitions of the beam radii and divergence angles [23], (Section 2.1.2).

A few properties following from the ABCD law are defined in Table 2-1. All these properties can be determined by carefully measuring the beam radius at various positions (slices) along the beam propagation.

Minimum beam radius (minimum spot size)	$\langle w_0 \rangle$	(2.10)
Rayleigh Range	$\langle z_0 \rangle = \frac{\langle w_0 \rangle}{\langle q \rangle}$	(2.11)
Propagation Equation (beam radius) **à** for divergence angles less than 0.8 radians.	$\langle w(z) \rangle = \langle w_0 \rangle \sqrt{\left[1 + \left(\frac{z}{\langle z_0 \rangle}\right)^2\right]}$	(2.12)
Real radius of curvature $\frac{1}{q(z)} = \frac{1}{R(z)} + \frac{il}{pw^2(z)}$	$R_{gen} = \frac{\langle w^2 \rangle}{\langle wq \rangle}$	(2.13)
Complex radius of curvature	$q_{gen} = \frac{\langle wq \rangle}{\langle w^2 \rangle} + i\frac{l}{p\langle w(z) \rangle^2}$	(2.14)
Divergence angle	$\langle \Theta \rangle = \frac{\langle w_0 \rangle}{\langle z_0 \rangle}$	(2.15)
The generalized ABCD law with $\langle w_1 \rangle^2 = \langle w_{01} \rangle^2$ the beam waist and $\langle w_1 q_1 \rangle = 0$	$q_{gen,2} = \frac{Aq_{gen1} + B}{Cq_{gen1} + D}$ With ABCD the elements of any geometrical ray matrix.	(2.16)

Table 2-1: Properties derived from the moment definitions using the general ABCD law.

The principle planes of propagation, defined as XZ and YZ, are the planes containing the major and minor axes of the beam profile ellipse (see Figure 2-2). The azimuth angle j is defined as the angle between one of these two planes and the laboratory-measuring plane. Only one angle is required because the two planes are orthogonal. In most cases, this angle is unknown due to the unknown symmetry within the laser cavity and can be calculated using the following mixed moment equation on the two-dimensional beam profile,

$$j = \frac{1}{2}\arctan\left(\frac{2\langle w_x w_y \rangle^2}{\langle x^2 \rangle^2 - \langle y^2 \rangle^2}\right) \tag{2.17}$$

This equation is only valid for two-dimensional energy density distributions. There are also other manual methods for one-dimensional profiles, which will be given in a later chapter (Section 4.4.6).

2.2 Second moment matrices

2.2.1 General structure

The second order moments (pure and mixed) can be arranged in a 4×4 matrix called the second order moment matrix V [23], [18], [43].

$$V=\begin{pmatrix} \langle x^2\rangle & \langle x\,y\rangle & \langle x\,q_x\rangle & \langle x\,q_y\rangle \\ \langle x\,y\rangle & \langle y^2\rangle & \langle y\,q_x\rangle & \langle y\,q_y\rangle \\ \langle x\,q_x\rangle & \langle y\,q_x\rangle & \langle q_x^2\rangle & \langle q_x q_y\rangle \\ \langle x\,q_y\rangle & \langle y\,q_y\rangle & \langle q_x q_y\rangle & \langle q_y^2\rangle \end{pmatrix} \tag{2.18}$$

For clarity the symbols are replaced with their physical meanings in the following representation of the second moment matrix [18]:

$$V=\begin{pmatrix} \text{width-x} & \text{orientation near field ellipse} & \text{radius of curvature-x} & \text{propagation rotation} \\ \text{orientation near field ellipse} & \text{width-y} & \text{propagation rotation} & \text{radius of curvature-y} \\ \text{radius of curvature-x} & \text{propagation rotation} & \text{divergence-x} & \text{orientation far field ellipse} \\ \text{propagation rotation} & \text{radius of curvature-y} & \text{orientation far field ellipse} & \text{divergence-y} \end{pmatrix}$$

Beams can be completely classified according to the structure of their second moment matrices. This will be done in the following sections for a few simple beam types.

2.2.2 Stigmatic beams

All circular symmetric beams are classified as stigmatic and have the following second moment matrix structure [23],

$$V_{\text{Simple stigmatic}}=\begin{pmatrix} \langle x^2\rangle & 0 & \langle xq\rangle & 0 \\ 0 & \langle x^2\rangle & 0 & \langle xq\rangle \\ \langle xq\rangle & 0 & \langle q^2\rangle & 0 \\ 0 & \langle xq\rangle & 0 & \langle q^2\rangle \end{pmatrix}. \tag{2.19}$$

These beams are naturally unchanged by rotation due to their circular symmetry. All the terms of the second moment matrix that are related to rotation are therefore zero. Before classifying a beam as stigmatic, it must first be determined whether the beam indeed has circular symmetry. A simple test to do this is to determine the ratio between the radii on the principle directions. If this ratio does not exceed 1:1.15 the beam can be considered stigmatic [24].

The most elemental example of stigmatic beams is simple stigmatic beams, which are commonly referred to as Gaussian, or TEM_{00} beams. Simple stigmatic beams can be fully characterised by only two parameters, namely the waist radius w_0 and the radius of curvature R. Their beam radii and the divergence angles are indirectly proportional to each other [33]:

$$[\langle\Theta\rangle\langle w_0\rangle] = \Theta w_0 = \frac{l}{p} \tag{2.20}$$

This product of the beam radius and divergence is called the beam parameter product.

General stigmatic beams are also circular symmetric but do not have a specific relationship between w and q. Their beam parameter product (k_{stig}) is not necessarily a constant ($l \backslash p$) [23]. The beam parameter product is now defined as:

$$[\langle w_0\rangle\langle\Theta\rangle] = k_{stig}. \tag{2.21}$$

Their beam parameter product (k_{stig}) has to be measured and is always equal to or larger than the value for simple stigmatic beams ($l \backslash p$). A closely related, but extremely useful parameter, called the beam quality factor (M^2 factor), can now be defined by rewriting k_{stig} to compare it with simple stigmatic beams, which are the ideal beam type. The beam parameter product can be rewritten by using Equation (2.20),

$$\left[\langle w_0\rangle\langle\Theta\rangle\right] = M^2\frac{l}{p} \tag{2.22}$$

or using Equation (2.11)

$$M^2 = \frac{p}{l}\frac{\langle w_0\rangle^2}{\langle z_0\rangle} \tag{2.23}$$

The M^2 factor is always larger or equal to one, with one indicating a perfect simple stigmatic beam. General stigmatic beams are therefore characterised by three parameters. These are the waist radius w_0, the radius of curvature R and the beam quality factor M^2.

2.2.3 Astigmatic beams

Astigmatic beams are defined as noncircular, implying that they have two principle directions with no set relationship between w, R and M^2 in each direction. The most elementary of these are the simple astigmatic beams, which are non-rotating and do not change their energy density profile during propagation. Their beam parameter product (in one of the two principle directions) is defined as [23]

$$\left[\left\langle w_{0,x}\right\rangle\left\langle \Theta_x\right\rangle\right] = M_x^{\,2}\frac{l}{p} \tag{2.24}$$

Simple astigmatic beams need seven parameters to characterise them. These are the waist radii $w_{0,x}$ and $w_{0,y}$, the radii of curvature R_x and R_y, the beam quality factors M_x^2 and M_y^2 and the azimuth angle j between the x-axis of the beam coordinate system and the x-axis of the laboratory coordinate system (See Figure 2-2). General astigmatic beams can rotate or change their energy density profile function or shape as they propagate. Only their second moment radii changes as the beam propagates o that the profile scale with propagation distance. All the elements of their second moment matrices (Equation (2.18)) are non-zero [23].

2.2.4 The scope of this thesis

Laser beams that originate from simple stable resonators, and that have not been changed by special optics, fall into the simple astigmatic category. Most of the theory on beam characterisation has been developed for this type of beam [34], [8], [44], [24]. Any more complex beam falls outside the scope of this thesis. A test is given in the next section to determine if a beam is part of this subset, as beams that fall outside it are regularly encountered in practise.

2.3 The Kurtosis parameter

In many cases, confirmation is needed that a beam is simple astigmatic. The Kurtosis parameter can be very useful to determine this and is defined as follows [38], [28], [2]:

$$K = \frac{\left\langle x^{4th}\right\rangle}{\left(\left\langle x^{2nd}\right\rangle\right)^2} = \frac{\int_{-\infty}^{\infty}\left(x-\left\langle x^{1st}\right\rangle\right)^4\cdot I(x)dx \int_{-\infty}^{\infty} I(x)dx}{\left(\int_{-\infty}^{\infty}\left(x-\left\langle x^{1st}\right\rangle\right)^2\cdot I(x)dx\right)^2}. \tag{2.25}$$

This Kurtosis parameter is a measure of how “sharp” a beam’s energy density profile is. The following three types of beam profiles can be identified. Simple astigmatic beams that have an exact Gaussian profile are called mesokurtic and have a Kurtosis parameter (K) of 3. Beams that have sharper profiles than a stigmatic beam, have K values that are higher than 3 and are called leptokurtic. Beams that have flatter profiles than simple stigmatic beams have K values that are smaller than 3 and are called platikurtic [38]. Beams that change their K value in either of the two principle directions as they propagate either rotate or change their beam profile and can therefore not be simple astigmatic. To determine whether there is a change in K, profile measurements must be done in the near and the far field. Measuring errors must be taken into account when comparing the two K values as well as the fact that there is a small chance that the beam could have rotated with an angle that was a multiple of p . If the beam rotated by p most beam profiles appears identical because they are usually symmetrical around the centre of mass $\langle x \rangle$.

2.4 Summary

The framework from which to approach beam analysis was laid down by means of the second moment theory. Different types of beams have been classified by means of a mathematically elegant second moment matrix. The scope of this thesis has been identified and a test for rotational moments and non-orthogonality has been given. This chapter was intended to be sufficiently general to apply to all kinds of beams, not necessarily only to laser beams. The next chapter will focus specifically on the development of a theory for laser beams that originate from simple resonators.

Chapter 3

Modelling of simple laser beams

Many ways have been found to model energy density distributions of laser beams since they were first observed. These models can be divided into two different methods according to their approach. The first focused on the generalisation of the two classical spherical and plane wave models [33], [45]. Another method focused on the laser resonator and tried to find stable energy density distributions or eigen-values for it [33], [23]. Not surprisingly, the solutions to both approaches (after some simplifications) consist of the same basis functions. The resonator approach and its solutions will be summarised in this chapter because it provides additional information specific to laser beams.

3.1 The resonator approach to model laser beams

Electromagnetic field distributions in stable resonators can be accurately calculated with the well-known Huygens Fresnel summation [23].

An electric field distribution at a point A $\vec{E}(A)$ propagates into space in such a way that each point on the wave front is considered a source of a small spherical wavelet. At another point B in space, the resulting electric field is a superposition of all these spherical wavelets and can be found by the following equation.

$$\vec{E}(B) = Ce^{-iwt}\sum_{j=1}^{N} E(x_j, y_j)\frac{e^{ikr_j}}{r_j}\cos q_j \Delta x \Delta y \qquad (3.1)$$

With w the angular frequency, k the wavenumber, r_j the distance between the two points and q_j the angle between the points and a reference direction. Resonator outputs can be numerically simulated by starting off with an arbitrary beam profile and then applying this

summation for a large finite number of round trips to obtain stable electric field distributions within the resonator. This has first been calculated on a digital computer by Fox and Li in the 1960s [19]. Their calculations showed that after about 300 round trips a wave front profile that appeared cosine remained stable. This was later established to be the energy density distribution of the fundamental mode. A more sophisticated procedure called the Prony method [45] also yielded mixtures of higher order modes. The numerical profiles are, however, impractical because they cannot be used in analytical calculations even though they were generated in the same way a real laser resonator would generate laser beams.

Some approximations have to be made to obtain analytical results, which can be used in further calculations. The Huygens Fresnel summation (Equation (3.1)) reduces to the Kirchoff integral (Equation (3.2)) when the paraxial approximation* is used [45], [23]:

$$E(B) = -\frac{i}{l\,e^{iwt}} \int_a \frac{E_1(Q)ge^{(ikr)}}{r} dA \tag{3.2}$$

Instead of using a point source an area source of size Q is used in the integral.

When ray transfer matrices [23], [45] are incorporated into the Kirchoff integral (Equation (3.2)), it becomes the Collins integral (this is valid because ray transfer matrices are also based on the paraxial approximation).

$$E_2(x_2, y_2) = -i / l\,Be^{(ikL)} \iint E_1(x_1, y_1) e^{\left[i\frac{p}{lB}(Ax_1^2 + Dx_2^2 - 2x_1x_2 + Ay_1^2 + Dy_2^2 - 2y_1y_2 \right]} dx_1 dy_1 \tag{3.3}$$

A, B, D are the matrix elements of the ray transfer matrix $M = \begin{pmatrix} A & B \\ C & D \end{pmatrix}$.

The ray transfer matrix for one round trip in the simple resonator pictured in Figure 3-1 is [23], [45]:

$$M_{\text{simple resonator}} = \begin{pmatrix} G & 2Lg_2 \\ (G^2 - 1)/2Lg_2 & G \end{pmatrix} \tag{3.4}$$

with

$$G = 2g_1g_2 - 1 \tag{3.5}$$

and

$$g_i = 1 - L / r_i \tag{3.6}$$

where r_i is the curvature of mirror i (i =1 or 2).

* This approximation is usually valid for most laser beams and only breaks down when a laser beam is focused too tightly (i.e. where $\sin q$ can no longer be approximated as q)

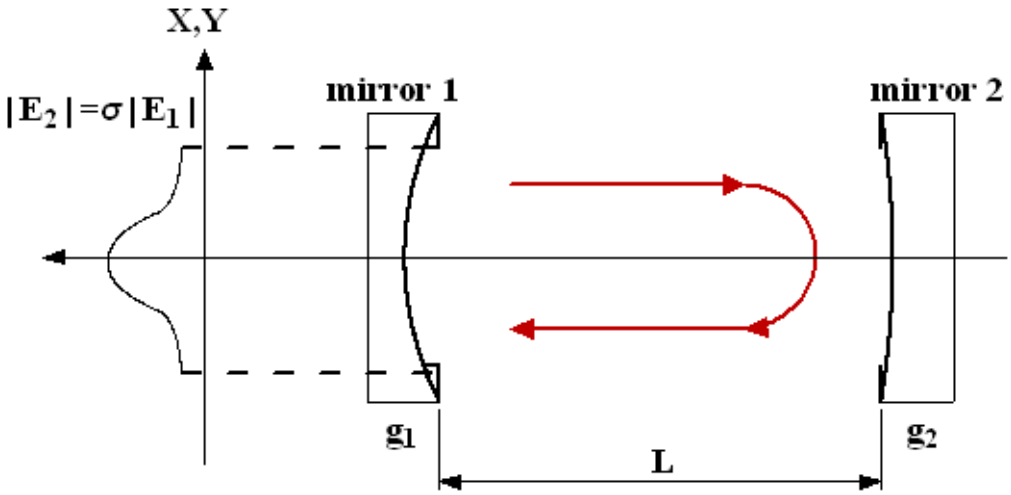

Figure 3-1: Simple resonator of length L and g parameters g_1 and g_2 with $g_i = 1 - L / r_i$.

Inserting the elements of matrix (3.4) into Equation (3.3) it is found that

$$E_2(x_2, y_2) = \frac{-ie^{(ikL)}}{2Lg_j l} \iint E_1(x_1, y_1) e^{\left[i\frac{p}{2Lg_j l}\left(G(x_1^2+y_1^2+x_2^2+y_2^2)-2(x_1x_2+y_1y_2)\right)\right]} dx_1 dy_1 \tag{3.7}$$

This integral is an eigen-value problem with the following restrictions [23], [45].

1. The electric field profile must remain unchanged after a full round trip

$$E(x, y, 2L) = s_{mn} e^{-2ikL} E(x, y, 0) \tag{3.8}$$

where s_{mn} is the complex eigen-value of order m and n.

$$s_{mn} = |s_{mn}| e^{if_{mn}} \tag{3.9}$$

The real part of the eigen-value ($|s_{mn}|$) is smaller than one and is indicative of the losses in the system. An extra phase shift of f_{mn} is introduced to the normal free space propagation over the 2L distance because the eigen-value (s_{mn}) is complex [45]. The total single period phase shift therefore becomes

$$\Delta f_{mn} = 2kL + f_{mn} \tag{3.10}$$

2. This total round-trip phase must undergo a phase change of $2p$. This is in accordance with normal theory on standing waves, which states that for any standing wave an integer number of half wavelengths must fit into the distance L it is contained in.

$$2p\,q = \Delta f_{mn} = 2kL + f_{mn} \tag{3.11}$$

If $2pu/c$ is substituted for k (the wave number), the resonator eigen, or resonance frequencies are obtained

$$u_{qmn} = \frac{c}{2L}\left[q + \frac{f_{mn}}{2p}\right]. \tag{3.12}$$

These frequencies produce longitudinal and transverse mode beating in laser outputs.

3. The resonator symmetry must be taken into account when the integral (3.7) is solved.

3.2 Solutions to the Collins integral

The standard and elegant Gaussian functions are solutions when the Collins integral is solved with the restrictions respectively [5] of the previous section. These solutions consist of two distinct parts, namely a defining function f and a Gaussian function part, G,

$$E = fe^{-iG} \tag{3.13}$$

The elegant functions have a complex argument for both the Gaussian function part where the standard solutions only have a real function part. This thesis will focus mainly on the standard solutions since beams originating from simple stable resonators can usually be described by them [45]. Whenever the term Gaussian is used, it will refer to all the standard solutions.

3.2.1 The standard Gaussian solutions

The standard Hermite (Equation (3.14)) and Laguerre Gaussian (Equation (3.15)) solutions are obtained when rectangular and cylindrical symmetry are respectively used in the base functions [23], [29]:

$$E(x,y,z) = \frac{E_0}{\sqrt{1+\left(z/z_0\right)^2}} e^{-\left[(x^2+y^2)/w^2_{00}\right]} H_m\left[\frac{\sqrt{2}x}{w_{00}(z)}\right] H_n\left[\frac{\sqrt{2}y}{w_{00}(z)}\right] e^{-ik\left[\frac{(x^2+y^2)}{2R(z)}\right]} e^{i\left[-kz+(m+n+1)\tan^{-1}(z/z_0)\right]} \tag{3.14}$$

and

$$E(r,\Phi,z) = \frac{E_0}{\sqrt{1+\left(z/z_0\right)^2}} e^{-\left[\frac{r^2}{w_{00}(z)^2}\right]} \left[\frac{\sqrt{2}r}{w_{00}(z)}\right]^{\mathbf{l}} L_{p\mathbf{l}}\left[\frac{2r^2}{w_{00}(z)^2}\right] \begin{Bmatrix}\cos(\mathbf{l}\Phi)\\ \sin(\mathbf{l}\Phi)\end{Bmatrix} e^{-\left[ikr^2/2R(z)\right]} e^{i\left[-kz+(2p+\mathbf{l}+1)\tan^{-1}(z/z_0)\right]} \tag{3.15}$$

with z_0 the Rayleigh Range, w_{00} the Gaussian beam radius, $R(z)$ the Radius of curvature, k the wave number of a plane wave, H_n the Hermite polynomial of order n and L_{pl} the Laguerre polynomials of order p and l.

The Hermitian polynomials are [52]:

$$H_0 = 1$$
$$H_1(x) = 2x$$
$$H_2(x) = 4x^2 - 2...$$

They obey the recursion rule

$$H_{n+1}(x) = 2xH_n(x) - 2nH_{n-1}(x)\,. \tag{3.16}$$

The Laguerre polynomials are [53]:

$$L_0(x) = 1$$
$$L_1(x) = -x + 1$$
$$L_2(x) = 0.5(x^2 - 4x + 2)...$$

They obey the recursion rule

$$(n+1)L_{n+1}(x) = (2n+1-x)L_n(x) - nL_{n-1}(x)\,. \tag{3.17}$$

Resonators that have small defects on windows and mirrors automatically have rectangular symmetry. The majority of lasers have small defects and are therefore best-described using Hermitian polynomials. However, high quality CW CO_2, HeNe and several other sealed off laser systems often display cylindrical symmetry.

The energy density is a much more practical quantity than the electric field. It is proportional to the square of the amplitude of the electric field.

$$I(r) = \frac{ce_0}{2}\left[\mathrm{Re}(E)\right]^2. \tag{3.18}$$

The energy density distribution for rectangular symmetry can be found by inserting Equation (3.14) into Equation (3.18).

$$\mathrm{I}_{mn}\left[x,y,z\right] = \frac{ce_0}{2}\left|E_0\right|^2\left[\frac{1}{\sqrt{1+\left(z/z_0\right)^2}}\right]^2 H^2{}_m\left[\frac{\sqrt{2}x}{w_{00}(z)}\right]H^2{}_n\left[\frac{\sqrt{2}y}{w_{00}(z)}\right]e^{-2\left(\frac{(x^2+y^2)}{w^2{}_{00}}\right)} \tag{3.19}$$

and for cylindrical symmetry using Equation (3.15) it is similarly found that

$$I_{pl}\left[r,f,z\right] = \frac{ce_0}{2}\left|E_0\right|^2\left[\frac{1}{\sqrt{1+\left(z/z_0\right)^2}}\right]^2\left[\frac{2r^2(z)}{w_{00}{}^2(z)}\right]^l L^2_{p,l}\left[\frac{2r^2(z)}{w_{00}{}^2(z)}\right]e^{-\frac{2r^2(z)}{w_{00}{}^2(z)}}\begin{cases}\cos^2(lf)\\ \sin^2(lf)\end{cases}. \tag{3.20}$$

Multiple solutions can be found by inserting integers into m and n of Equation (3.19) or into p and l of Equation (3.20). These solutions are referred to as Transverse Electromagnetic modes (TEM) of lasers because they describe the variation of the optical fields in the cross-

sectional planes perpendicular to the propagation axis. The electric field of any arbitrary paraxial beam can be expanded using the Hermitian or Laguerre functions which are orthogonal to each other. The intensity of this electric field will therefore not have cross terms because of the orthonormality condition.

$$\int_{-\infty}^{\infty} u_n^*(x,z)\tilde{u}_n(x,z)dx = d_{nm} \qquad (3.21)$$

Where

$\tilde{u}_n$ is the either the Hermitian or Laguerre functions [45].

Real laser beams therefore consist of a linear combination of these solutions in either of the symmetries [45]. The next few sections will discuss these solutions in more detail.

3.2.1.1 The fundamental TEM_{00} mode

Figure 3-2 shows the energy density distributions of the first or fundamental TEM_{00} mode for both the Hermite and Laguerre Gaussian solutions. This solution is found when setting $m = n = 0$ for rectangular symmetry or $p = l = 0$ for cylindrical symmetry.

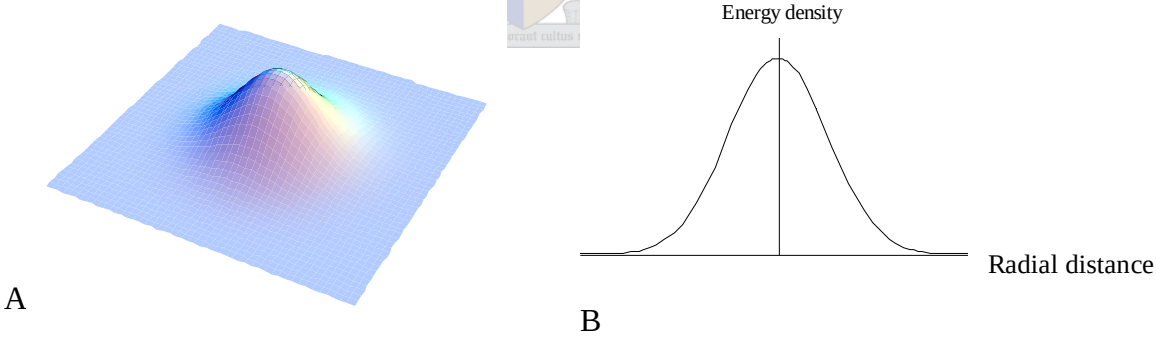

Figure 3-2: TEM_{00} energy density distribution in two (A) and one (B) spatial dimension(s).

The radial distribution of the TEM_{00} mode is called a Gaussian distribution. The TEM_{00} mode is therefore commonly referred to as the Gaussian mode. It is classified as simple stigmatic and is considered the ideal to which all other beams are compared (Section 2.2.2).

A TEM_{00} beam is preferred in many high precision applications since

- it has the lowest divergence,

- it can be focused the tightest,
- it has no local points of high energy density (hot spots),
- its circular profile is sought after in many applications (to drill holes for example) and
- it couples well into waveguides.

The Gaussian beam radius $w_{00}(z)$ is defined as the lateral distance from the z-axis where the energy density is $1/e^2$ (~13.5%) of the maximum M-value on the axis. It is found by integration that the energy that is contained within a circle with this radius centred on the z-axis is 86.5%. This beam radius also corresponds exactly to the second moment radius $\langle w \rangle$ of the TEM_{00} mode. $w_{00}(z)$ is a logical definition for the beam radius since it occurs naturally in the exponent of both solutions of Equations (3.14) and (3.15).

The following properties follow naturally from the Gaussian solutions and are illustrated in Figure 3-3 [33], [23], [45].

- The TEM_{00} beam radius $w_{00}(z)$ varies hyperbolically in the propagation direction z according to the following relation:

$$w_{00}(z) = w_{00,0}\sqrt{1+\left(z^2 / z_0{}^2\right)} \tag{3.22}$$

  where the minimum beam radius is $w_{00,0}$.

- The Rayleigh Range (z_0) is a measure of the extent of the waist region and is defined as the length where the beam area has doubled from that at the waist:

$$w_{00}(z_0) = w_{00,0}\sqrt{2} \tag{3.23}$$

or

$$z_0 = \frac{p w_{00,0}^2}{l} \tag{3.24}$$

- $q(z)$ is the termed the beam parameter or complex radius of curvature. Its amplitude changes as the beam propagates.

$$\frac{1}{q(z)} = \frac{1}{R(z)} + \frac{i\,l}{p w_{00}^2(z)} \tag{3.25}$$

- $R(z)$ is the real part of $q(z)$ and is commonly referred to as the radius of curvature. It is infinitively large at the waist position.

$$R(z) = z + \frac{z_0^2}{z} \tag{3.26}$$

- The angle of divergence Θ is defined as the half angle between the propagation direction and one of the asymptotes to the beam radius hyperbole:

$$\Theta = \lim_{z\to\infty} \frac{w_{00}(z)}{z} \tag{3.27}$$

The TEM_{00} mode is simple stigmatic so that $\Theta w_0 = l / p$ [54] or

$$\Theta = \frac{l}{p w_{00,0}} = \frac{w_{00,0}}{z_0}. \tag{3.28}$$

- It can be proved that the ABCD law of geometrical optics can be used to change the complex radius of curvature q(z) as the beam propagates [23].

$$q_f = \frac{Aq_i + B}{Cq_i + D} \tag{3.29}$$

where A, B, C and D are the elements of any geometrical ray matrix.

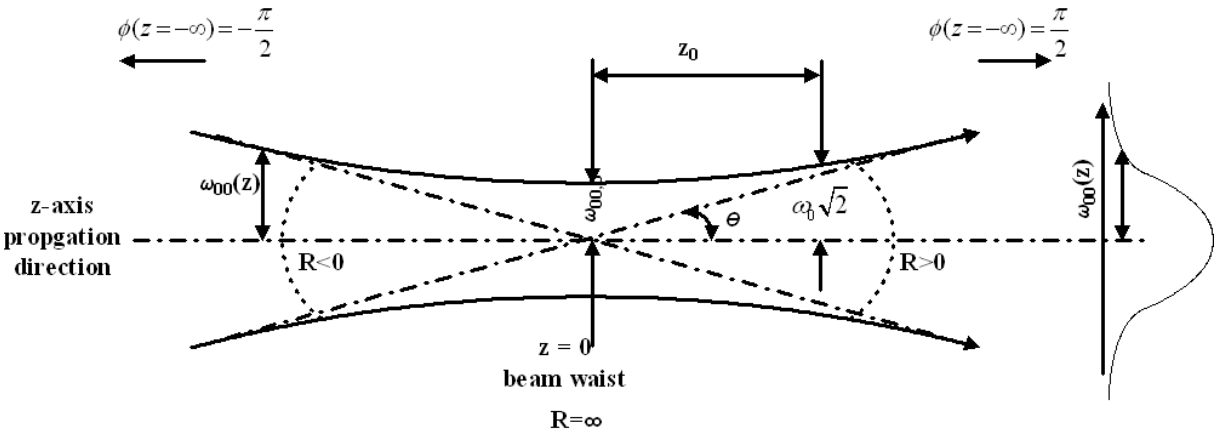

Figure 3-3: Hyperbolic variation of the beam radius of a TEM_{00} beam and the illustration of other beam properties.

3.2.1.2 Rectangular symmetric higher order modes

All the pure rectangular TEM_{xy} modes with the exception of the fundamental mode are referred to as higher order rectangular or Hermitian modes. Equation (3.19) is plotted in one and two spatial dimensions for fixed m and n values in Figure 3-4 and Figure 3-5. It can be seen that that there is a direct relationship between the higher order mode number and the number of nodes or zero points of the energy density distribution.

The energy density profiles of the TEM_{xy} X0 and TEM_{xy} 0Y modes are completely separable in Cartesian coordinates due to their rectangular symmetry. This implies that the normalised profile obtained by setting $y = 0$ in Equation (3.19) (Figure 3-4 B) and that obtained by integrating in the y direction are identical. The graphical proof of this can be seen in Appendix C. Whenever these solutions are used in further calculations (like integrals), rectangular coordinates must be used.

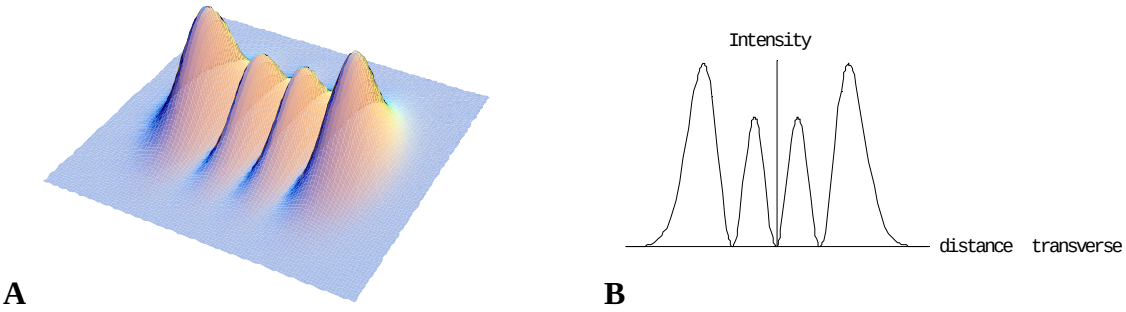

A **B**

Figure 3-4: The energy density distribution of the TEM_{xy} 03 mode in two (A) and one (B) spatial Cartesian dimension(s).

The rectangular nature of the Hermitian functions is more apparent in mode structures consisting of the same higher order mode number in both the transverse directions. This can be seen in Figure 3-5 B. The rectangular shape also becomes more noticeable as the mode number is increased.

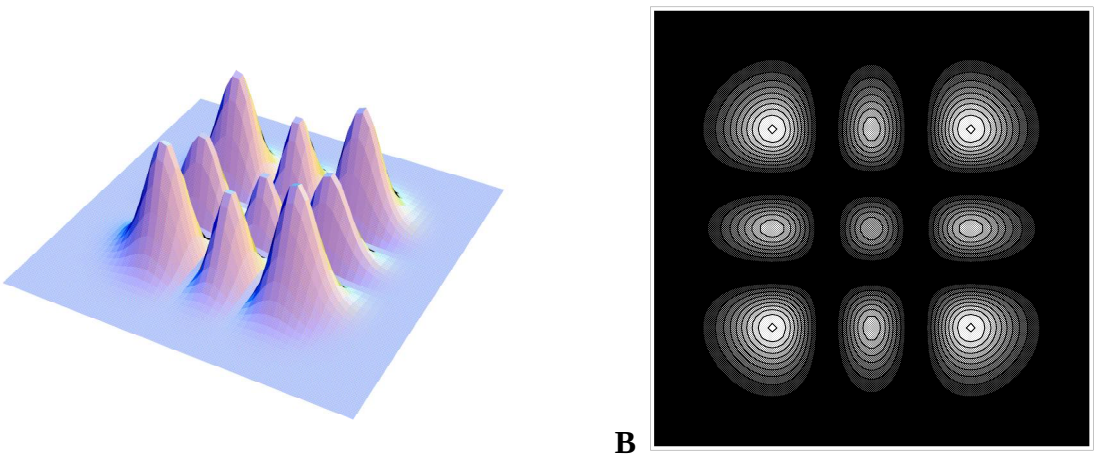

A **B**

Figure 3-5: The energy density distribution of the TEM_{xy} 22 mode in two spatial dimensions (A) and a contour graph (B) of it in two spatial dimensions.

3.2.1.3 Cylindrical symmetric higher order modes

All the pure cylindrical symmetric TEM_{pl} PL modes with the exception of the fundamental are referred to as higher order cylindrical symmetric or Laguerrian modes. The energy density distributions for a few cylindrical symmetric TEM_{pl} PL modes are shown in Figure 3-6. Plots of the full two-dimensional energy density distributions of Equation (3.20) can be seen to the left and their respective contour plots to the right. These contour plots will also be the patterns, which are observed on a carbon block or thermal paper when a high power laser beam impinges on it.

For cylindrical symmetric modes the differences between pure modes in the two principle directions are more apparent than in rectangular symmetry. The higher order mode number is again related to the number of nodes. The first mode number p, gives the number of node rings in the azimuthal direction (See Figure 3-6 A and B). Because of these ring patterns the pure azimuthal TEM_{pl} P0 modes have the appearance of a droplet hitting a liquid surface.

The second mode number l is related to the number of node lines in the radial direction, which gives the pure radial TEM_{pl} 0L modes a star-like appearance (see Figure 3-6 E). An asterisk after this mode number indicates that the sine instead of the cosine is used in the generating function Equation (3.20) the difference between using the cosine and the sine being that the position of the peaks and nodes are interchanged for even mode numbers because of the $p/2$ phase difference between sine and cosine functions. This difference is purely artificial since any radial mode that permanently remains in any one azimuthal position would favour a Cartesian direction. The modes could therefore only temporarily form in one azimuthal direction since there should be no restriction on them to form in any other azimuthal direction. A mixture of radial and azimuthal mode structures gives the temporary energy density pattern a flower like appearance (See Figure 3-6 G and H).

These cylindrical symmetric solutions are not separable in the Cartesian coordinates in contrast to the Hermitian modes. Whenever these solutions are used in further calculations (like integrals), cylindrical coordinates must be used.

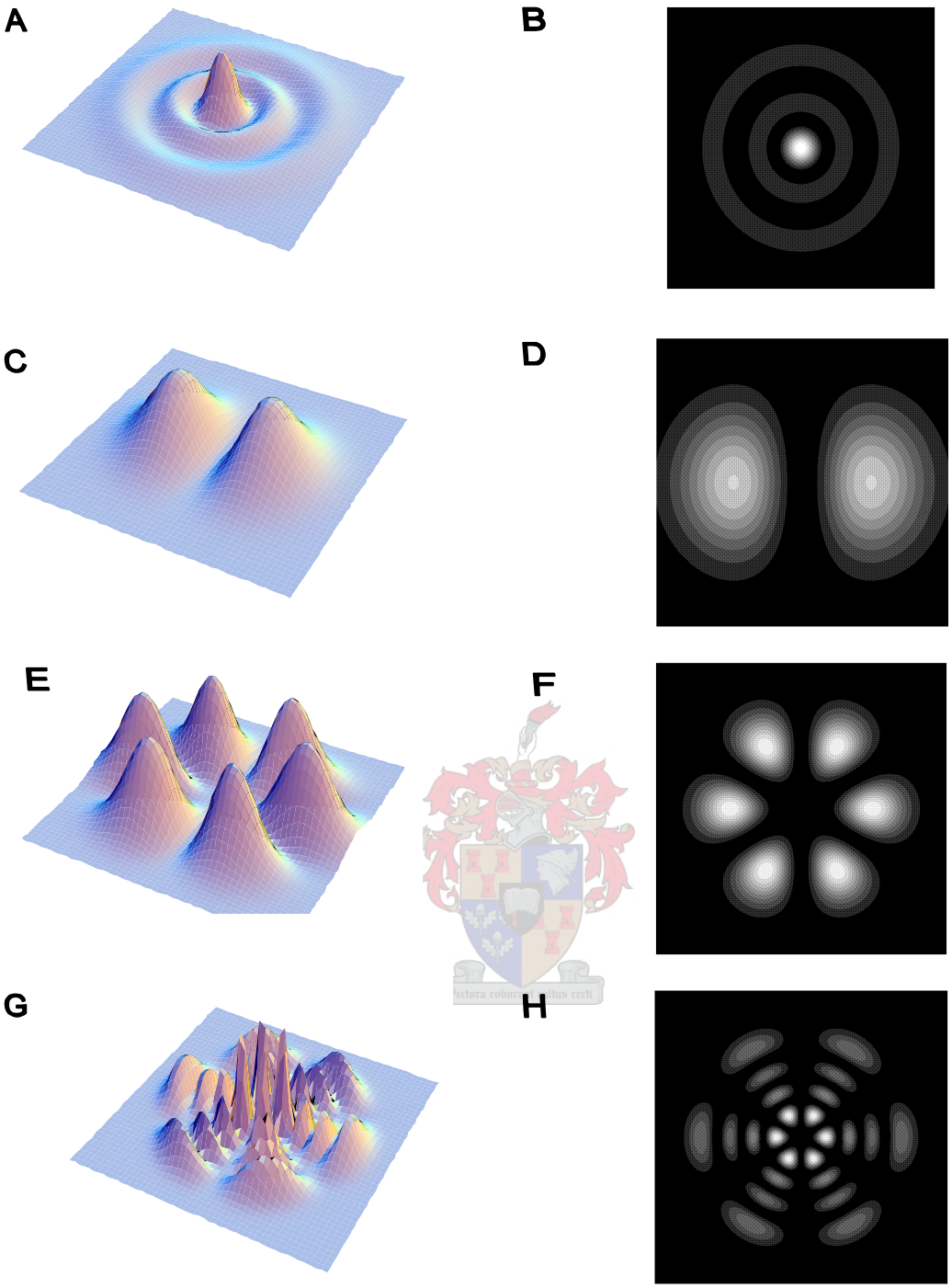

Figure 3-6: Three-dimensional energy density distributions (left) and carbon block patterns (right) of various pure cylindrical symmetric modes. A and B are TEM_{pl} 20, C and D are is TEM_{pl} 01, E and F are TEM_{pl} 03 and G and H are TEM_{pl} 33.

3.2.2 Classification of Gaussian beams according to the second moment matrix

The fundamental or TEM_{00} mode of both symmetries qualifies as simple stigmatic. All cylindrical symmetric beams are stigmatic by definition (Section 2.2.2). Any rectangular higher order mode combination that passes the circularity test is naturally general stigmatic. An example of this is pure double rectangular modes where $m = n$. All the other rectangular higher order modes are simple astigmatic.

It is commonly thought that simple astigmatic beams are the most undesirable kind of beams that can emanate from simple resonators. Large defects on the optics can, however, cause phase instabilities so that the standard Gaussian solutions are no longer valid. The test for simple astigmatic beams (Section 2.2.2) should always be applied if the optics are degraded, of low quality or if other diffractive elements are present.

3.3 Application of second moment theory to Gaussian modes

The moment integral and definitions were derived to describe beams in general. The eigen-functions for the standard Gaussian beams were derived from the Huygens Fresnel equation. Relations for the radii, divergence and M^2 values of the pure higher order modes can be determined by substituting their energy density eigen-functions into the integral definitions of Chapter 2.

3.3.1 The general second moment radius

The rectangular energy density distribution (Equation (3.19)), substituted into the equation for the second moment radius (Equation (2.4) and (2.6) with $\langle x^{1st} \rangle$ set to zero), gives a relation for the second moment beam radius for rectangular symmetric modes:

$$\langle w_x \rangle = 2\sqrt{\frac{\int_{-\infty}^{+\infty} x^2 H_m^2\left[\sqrt{2}x/w_{00}\right] e^{-2\left(x^2/w_{00}^2\right)} dx}{\int_{-\infty}^{+\infty} H_m^2\left[\sqrt{2}x/w_{00}\right] e^{-2\left(x^2/w_{00}^2\right)} dx}} \tag{3.30}$$

The two integrals in Equation (3.30) are standard solutions for the quantum mechanical one-dimensional harmonic oscillator (Equations 7.15 and 7.17 of [22]). Inserting the solutions for

these integrals into Equation (3.30) provides the relationship between the radius of a rectangular higher order mode and that of the TEM_{00} mode,

$$\langle w_x \rangle = \sqrt{2m+1}\, w_{00}\,. \tag{3.31}$$

Similarly, when inserting the cylindrical energy density distribution (Equation (3.20)) into Equation (2.5) it is found that

$$\langle w_{pl} \rangle = \sqrt{2p+l+1}\, w_{00} \tag{3.32}$$

The second moment radii of the rectangular TEM_{xy} 01 and cylindrical TEM_{pl} 01 modes differ substantially even though in text books their two-dimensional energy density profiles are given as identical [23] , (Figure 3-6 C and D). The reason for this is that cylindrical symmetric modes are not allowed a preferential azimuthal direction, which makes cylindrical integration different from rectangular integration. The practical implications of this will be discussed in more detail Section 5.1.2.2.

3.3.2 The general second moment divergence

The general second moment divergence for pure rectangular symmetric modes is found by inserting Equation (3.31) into Equation (3.22) and using the result in the equation for the angle of divergence (Equation (2.9)), yielding

$$\langle \Theta_m \rangle = \frac{\sqrt{2m+1}}{w_{00,0}} \frac{l}{p}\,. \tag{3.33}$$

Similarly for cylindrical symmetry, inserting Equation (3.32) into Equation (3.22) gives

$$\langle \Theta_{p,l} \rangle = \frac{\sqrt{2p+l+1}}{w_{00,0}} \frac{l}{p}\,. \tag{3.34}$$

3.3.3 The beam quality factor (M^2) for Gaussian laser beams

General beam theory states that according to Equation (2.22)

$$M_x^2 = \frac{p\left[\langle w_{0x} \rangle \mathbf{g} \langle \Theta_x \rangle\right]}{l} \tag{3.35}$$

Inserting Equations (3.31) and (3.33) into Equation (3.35) it is found that

$$M_m{}^2 = p\left[\sqrt{2m+1} w_{00,0} \mathbf{g} \frac{\sqrt{2m+1}}{w_{00,0}} \frac{l}{p}\right] / \, l \tag{3.36}$$

so that

$$M_m^2 = 2m+1. \tag{3.37}$$

Similarly, for cylindrical symmetry it is found that

$$M_{p,l}{}^2 = 2p+l+1. \tag{3.38}$$

M^2 is called the beam quality factor, which is always larger or equal to one (Section 2.2.3). $M^2 = 1$ indicates a perfect TEM_{00} beam. It can also be proven when inserting Equations (3.37) and (3.38) into Equations (3.31) and (3.32) respectively that

$$\langle w_x \rangle = M w_{00}. \tag{3.39}$$

The M-value therefore indicates how much larger than the ideal TEM_{00} beam a measured beam is. Note that Equation (2.12) has to be used when the M^2 factor is determined by measurement of the beam propagation.

3.4 Summary

Beams originating from simple resonators with cylindrical and rectangular symmetry were modelled from basic diffractive principles. A theoretical framework is now in place to evaluate real laser beams. In the next chapter, various methods to measure the beam quantities discussed in this and the previous chapter are presented.

Chapter 4

Measurement, definition and correlation of laser beam radii

The spatial properties of a beam can be determined by measuring its radius at several positions along the beam propagation axis. It is therefore very important to measure the radii carefully and to use a consistent definition of the beam radius. This chapter will give an overview of different beam measuring techniques, which are closely related to different beam radius definitions. It will also present correlations between the different beam radius definitions and their resulting beam quality (M^2) values.

4.1 General measuring technique

The term “beam characterisation” refers to the measurement of the beam propagation as defined in Equation (2.12). The beam radius at any other z position (along the propagation axis), the beam quality factor (Equation (3.35)) and the divergence (Equation (2.9)) can be calculated from the measured beam propagation.

The beam propagation is obtained by measuring the beam radius at several z positions. Usually the waist is not accessible so that an artificial one needs to be created with a focusing lens [23]. Johnston proposed that measurements at only four positions along the beam propagation direction are necessary [25]. The ISO [24] specifies that at least ten are necessary and that at least half the measuring points should be within the estimated waist region and the other half should be distributed beyond two Rayleigh range lengths (Equation (2.11)) from the beam waist position. The frequency of the measuring points should also be doubled in the waist region [24]. This ratio and frequency has not been proven and can possibly be the

subject of future study. Figure 4-1 illustrates the generation of an artificial waist of a beam propagating from a laser source as well as the ISO recommended measuring points.

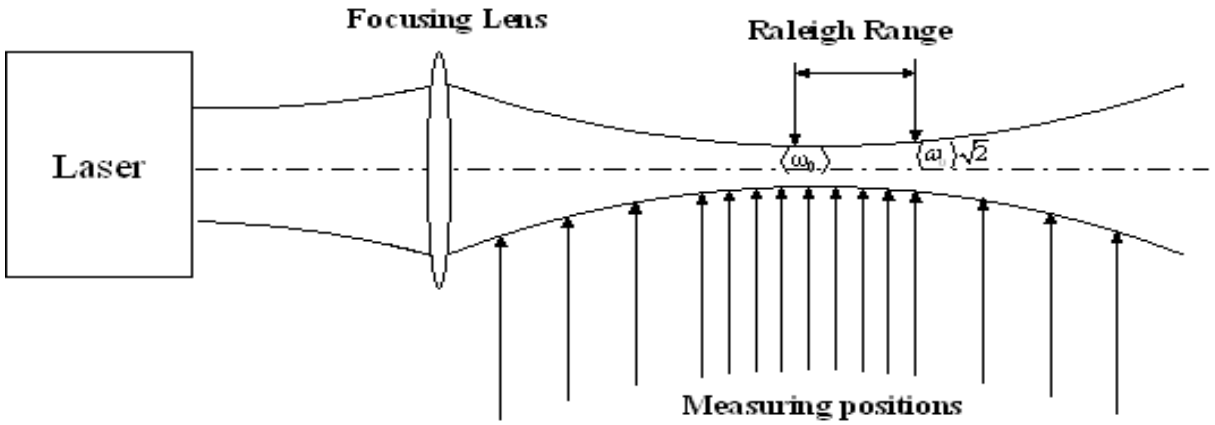

Figure 4-1: The artificial waist method. The arrows indicate the suggested measuring positions according to the ISO standard.

The ISO further specifies that at least five measurements should be performed at each measuring position along the propagation direction and the mean taken as the beam radius. This is not always possible with slow, low frequency measurements. The hyperbola of Equation (2.12) is then fitted onto the measured radii, which should be weighed inversely proportional to their magnitude, by means of a least squares method. The beam propagation properties are then obtained from the fitted functions. In the next section, several methods are discussed to measure the beam energy and energy density profiles at the different locations from which the beam radii can be determined.

4.2 Detection of beam profiles

Different beam profiles are closely related to different beam radius definitions. The profiles and ways to measure them are therefore discussed before the beam radius definitions are presented.

4.2.1 CCD cameras

Most modern beam analysers make use of cameras containing charge coupled device (CCD) detector arrays. The images are read into a computer where they are post-processed by software so that they can be viewed in one or two spatial dimensions (See Figure 4-2). The

beam radii are then calculated directly from these one or two-dimensional energy density distributions. The working range of these cameras typically extends from 100 nm in the ultra violet to 10 mm in the far-infrared when broadband coatings are applied [50]. Most broadband cameras are, however, not linear at 10 mm so that specialised pyro-electric cameras have to be used in this range.

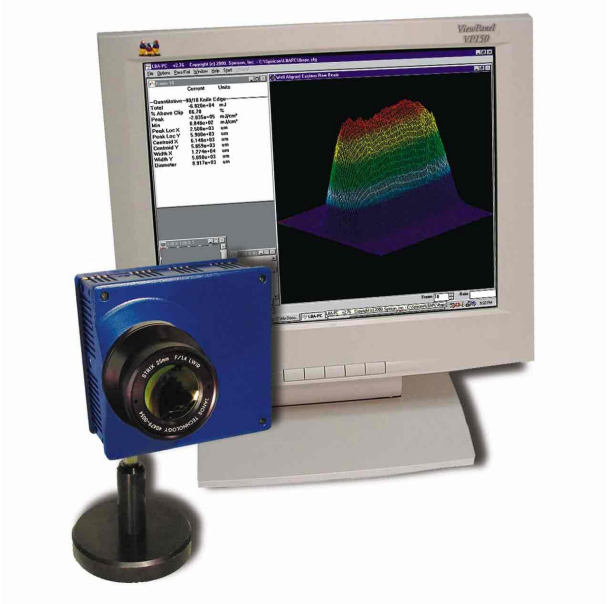

Figure 4-2: CCD camera and a two-dimensional energy density profile on a personal computer screen [50].

CCD camera profilers have the following advantages:

- They provide almost instantaneous two-dimensional information.
- They can perform single shot measurements in pulsed lasers.
- They are a relatively low cost solution for lasers emitting in the visible and UV wavelengths.
- They are available in different models and software packages.

CCD camera profilers also have the following disadvantages:

- Their resolution is limited by the pixel size (15-20 µm).
- Measurements from CCD cameras in focus positions can be inaccurate.
- Methods to attenuate high-power laser beams to protect CCD cameras can distort the beam.
- CCD cameras are expensive when designed for far-infrared wavelengths.

4.2.2 Moving pinhole method

A pinhole is used to scan across a beam in front of a large area detector to obtain either one or two-dimensional energy density profiles. This is the time consuming mechanical equivalent of a camera or linear diode array.

The pinhole method has the following advantages:

- The pinhole method is a cheap way to obtain a two-dimensional profile of a beam.
- The method can be applied for a wide range of lasers.
- Pinhole profilers can be used for high power lasers.
- The method can measure beam profiles very accurately.

The pinhole method also has the following disadvantages:

- The method usually has a very low signal to noise ratio.
- Pinhole profile scans can miss anomalies when performing one-dimensional scans.
- The method is slow when compared to cameras.

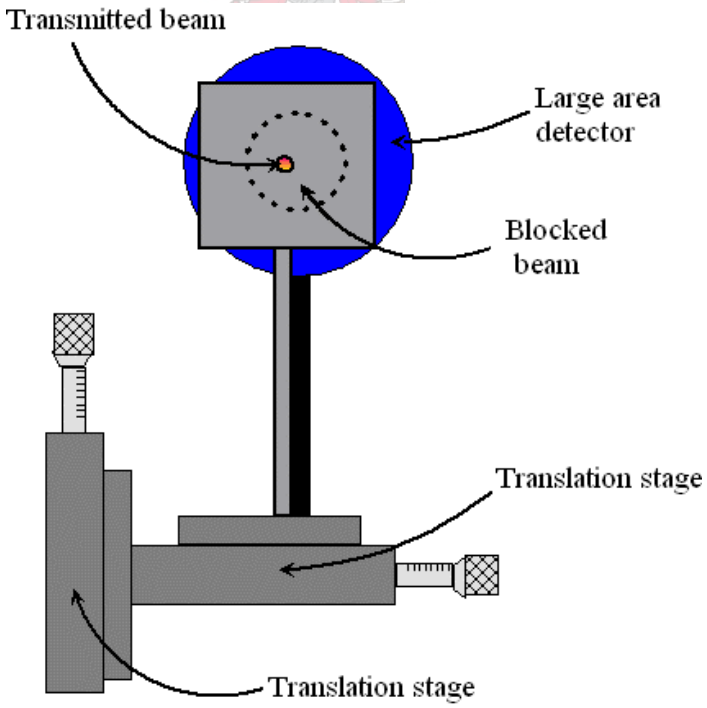

Figure 4-3: A pinhole that is mounted on two translation stages allowing only a fraction of the beam to fall onto large area detector.

4.2.3 Moving slit method

The moving slit method is the most widely used and straightforward technique to measure beam radii. A slit that is no wider than approximately $1/20^{th}$ (5%) of the beam diameter cuts the beam laterally by means of a mounted translation stage in front of a large area detector. The transmitted energy is then measured as a function of the position of the slit (See Figure 4-4. The length of the slit must at least cover the diameter of the detector and be no less than twice the beam diameter. The energy density is integrated in the direction perpendicular to the movement of the translation stage. The resulting profile can therefore be referred to as the slit integrated profile in the direction of the movement of the translation stage. For conciseness, these profiles will only be referred to as slit profiles.

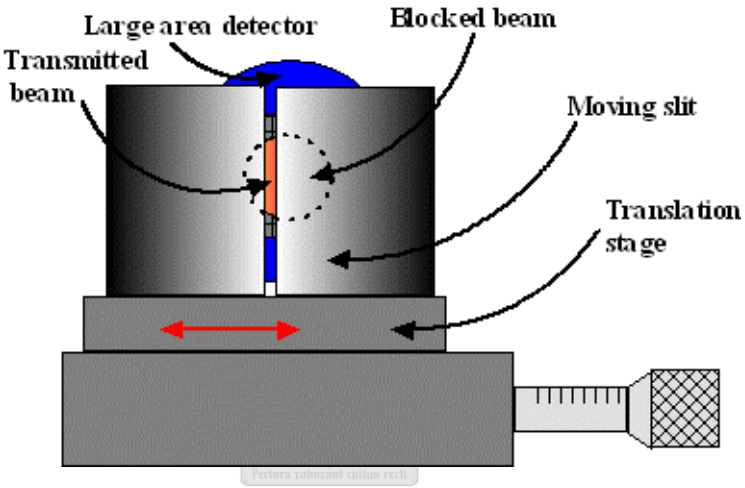

Figure 4-4: A slit that is mounted on a translation stage allowing only a fraction of the beam to fall onto large area detector.

The energy transmitted by a slit can be mathematically modelled.

When a slit of length 2L and width 2W is scanned in the x direction across a beam with a two-dimensional energy density distribution $F(x,y)$, the transmitted energy at an arbitrary position x_p is

$$E_{\text{slit}}(x) = \int_{-L}^{+L} \int_{x_p-W}^{x_p+W} F(x,y)\,dx\,dy\,. \qquad (4.1)$$

The implications of varying the slit width are now demonstrated by inserting a two-dimensional TEM_{00} energy density distribution (Equation (3.19) with the mode indices $m = n = 0$) into Equation (4.1). It is found that for a specific z position

$$E_{\text{slit}}(x) = \frac{ce_0}{2}\left|E_0\right|^2 \int_{-\infty}^{\infty} e^{\frac{-2y^2}{w_{00}^2(z)}} dy \int_{x_p-W}^{x_p+W} e^{\frac{-2x^2}{w_{00}^2(z)}} dx \tag{4.2}$$

and after integration it is found that [56]

$$E_{\text{slit}}(x) = k\left(\frac{1}{2} erf\left[\sqrt{2}\frac{(x_p - x_0)+W}{w_{00,x}}\right] + \frac{1}{2} erf\left[\sqrt{2}\frac{-(x_p - x_0)+W}{w_{00,x}}\right]\right) \tag{4.3}$$

with

$$erf(x) = \frac{2}{\sqrt{p}}\int_0^x e^{-x^2} dx \tag{4.4}$$

where k is the constant arising from the definite integral in the y direction.

Figure 4-5 A depicts the slit profiles of a TEM_{00} beam with a Gaussian radius of 1mm calculated with Equation (4.3) using various slit widths. It can be seen that at a slit width of 25% of the beam diameter, it becomes difficult to distinguish the slit profile from the theoretical TEM_{00} profile (dashed).

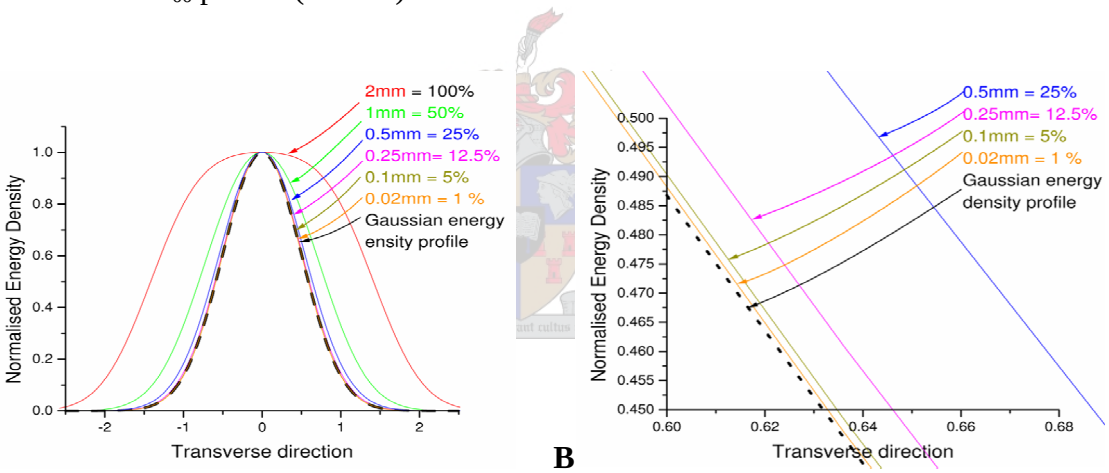

Figure 4-5: (A) shows slit profiles of a TEM_{00} beam calculated with varying degrees of slit widths. (B) shows an expansion of A indicating the difference in profiles using slit widths less than 5% of the beam diameter.

The error made by using a finite slit width is called a convolution error. Figure 4-5 (B) shows an expanded section of Figure 4-5 (A), indicating that that there is still a difference between the TEM_{00} profile and the transmitted energy profiles for slit widths smaller than 5% of the beam diameter. This difference is usually much smaller than the measurement error for these narrow slit widths. The signal to noise ratio increases dramatically as the slit width is decreased so that it is often necessary to compromise between the signal to noise ratio and the convolution error when choosing a slit width. When the signal is already low, the slit width

needs to be changed at several positions along a focused beam. Under these circumstances, slit scanning can become a very difficult technique to automate. It is often necessary to reduce the laser power or energy in order to avoid this. The signal to noise ratio can then become so low that the slit method becomes extremely inaccurate.

The slit method has the following advantages:

- Moving slits can be used to scan high-power lasers.
- Slits can vary the transmitted energy density without having to adjust the level of attenuation simply by varying their width.
- Slits can measure over a wider area than cameras.
- The method provides high accuracy over a wide range of wavelengths and test conditions.

The slit method also has a few disadvantages:

- The method can perform beam analysis in only one dimension at a time.
- Results from this method are susceptible to mechanical vibrations due to the slow speed. This forces the instrument to be large and bulky.
- The signal to noise ratio of this method is too low in many cases to be able to use a single slit width for all the profile measurements along the beam propagation direction.
- In many cases, the method cannot be used at all because the signal to noise ratio is too low.

4.2.4 Moving knife-edge method

This method employs a knife-edge, which cuts the laser beam laterally by means of a translation stage in front of a large area detector. The energy density is integrated over the uncovered area and the transmitted energy is measured as a function of the position of the knife-edge.

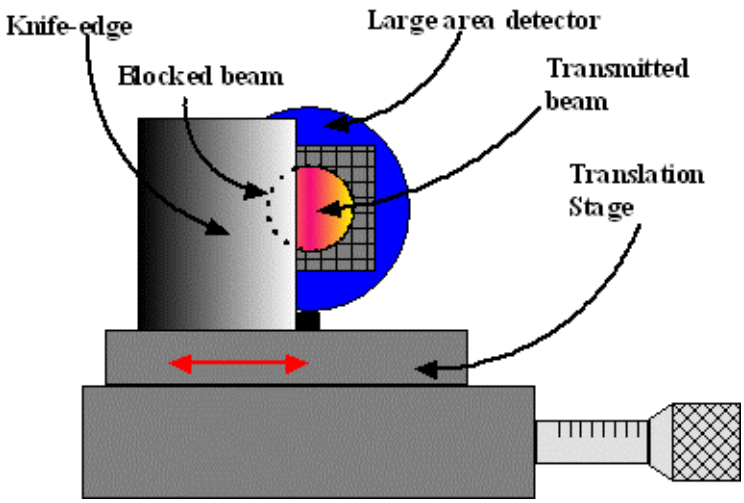

Figure 4-6: A knife-edge mounted on a translation stage allowing only part of the inflowing energy to fall on a large area detector.

The energy transmitted by the knife-edge can be mathematically modelled.

A knife-edge of length 2L scans a beam with energy density distribution $F(x,y)$ in the arbitrary transverse direction x. The beam is initially fully blocked off by the knife-edge, which then opens up the beam from a position that is approximated as infinite far away to a general position X.

The transmitted energy profile will then be

$$E_{\text{knife}}(x) = \int_{-L}^{L}\int_{-\infty}^{X} F(x,y)\,dx\,dy \tag{4.5}$$

The knife-edge length is usually approximated as infinite wide so that L can be replaced by ∞.

The transmitted knife-edge energy of a TEM_{00} mode is

$$E_{\text{knife}}(X) = \frac{ce_0}{2}\left|E_0\right|^2 \int_{-\infty}^{\infty} e^{\frac{-2y^2}{w_{00}^2(z)}}dy \int_{X}^{\infty} e^{\frac{-2x^2}{w_{00}^2(z)}}dx \tag{4.6}$$

After integrating, normalising and using of the error function (Equation (4.4)), it is found that the knife-edge energy function for the TEM_{00} mode is

$$E_{\text{knife gauss}}(x) = \frac{1}{2}\left[erf\left(\frac{-\sqrt{2}x}{w_{00}^2(z)}\right)+1\right] \tag{4.7}$$

Plotted, the TEM_{00} knife-edge profile appears sigmoidal. The formation of this sigmoidal distribution can be conceptualised from Figure 4-7.

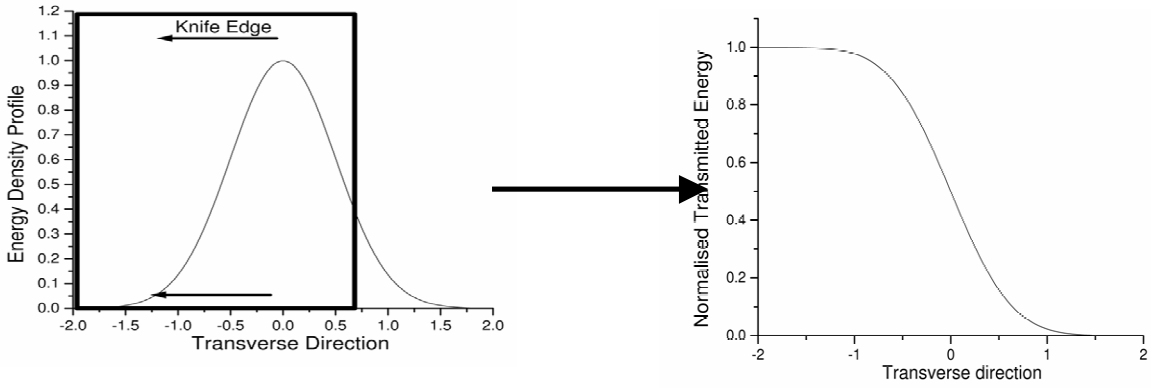

Figure 4-7: The energy density and energy profiles of a TEM_{00} beam with $w_{00,x} = 1$.

The transmitted knife-edge energy of the first Hermitian higher order mode (TEM_{xy} 01) is given by the following normalised energy function:

$$E_{\text{knife TEM01}}(x) = \frac{1}{2}\left(erf\left(\frac{-\sqrt{2}(x - x_0)}{w_{00,x}}\right) + 1 \right) + \sqrt{\frac{2}{p}}\left(\frac{x - x_0}{w_{00,x}} \right) e^{-2\left(\frac{x - x_0}{w}\right)^2} \qquad (4.8)$$

The formation of its knife-edge energy profile can be conceptualised from Figure 4-8.

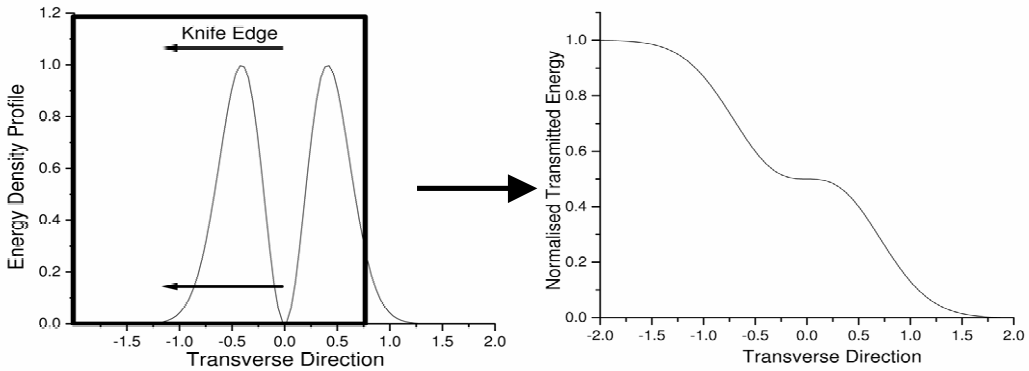

Figure 4-8: The energy density and energy profiles of a Gaussian TEM_{xy} 01 beam with $w_{00,x} = 1$.

The energy functions, energy density distributions and energy distributions of pure rectangular higher order modes up to TEM_{xy} 05 can be found in Appendix A. The energy profile of a beam can also be obtained by integrating its slit energy density profile.

The knife-edge method has the following advantages:

- Knife-edge scans provide the total energy at every scanning position in the propagation direction so that the energy stability of the laser can be monitored.
- It is the preferred method when the signal to noise ratio is low.
- Knife-edges can measure over a wider area than cameras.
- The method provides high accuracy and submicron resolution over a wide range of wavelengths and test conditions [55].

The knife-edge method also has a few disadvantages:

- Knife-edges cannot analyse very high-power lasers (the detector would be destroyed).
- The method can perform beam analysis in only one dimension per scan.
- The methods cause it to be susceptible to mechanical vibrations, forcing the measuring instrument to be large and bulky.
- The method is also limited because not all beam radius definitions (discussed in Section 4.3) can be applied to its profile due to feature loss in the integration process.

4.2.5 Variable-aperture method

High quality irises, or apertures of different sizes, are used to cut the beam circularly. The transmitted energy is then recorded as a function of the aperture radius. This method can be thought of as the knife-edge method for cylindrical symmetric beams. This is because the aperture cuts the beam between the cylindrical radial axis limits of 0 and ∞ while integrating between the azimuthal limits of 0 and $2p$. The knife-edge, on the other hand, makes use of rectangular symmetry to cut the beam between any two Cartesian coordinate axis limits of $-\infty$ to ∞ while integrating in the other direction. There is no practical equivalent to the slit method using physical cylindrical symmetric scanning devices.

The variable aperture method requires automatic centering, the development of a motorised calibrated iris and can only be used to measure stigmatic beams. In order to evaluate if the beam is sufficiently circular, the ratio between the radii on the two principle axes must be determined with a different scanning method. The variable-aperture method is therefore the least versatile [24] of all the methods discussed so far and will be omitted from future sections concerning beam characterisation. It does, however, have other practical applications as will be seen in Section 5.1.1.

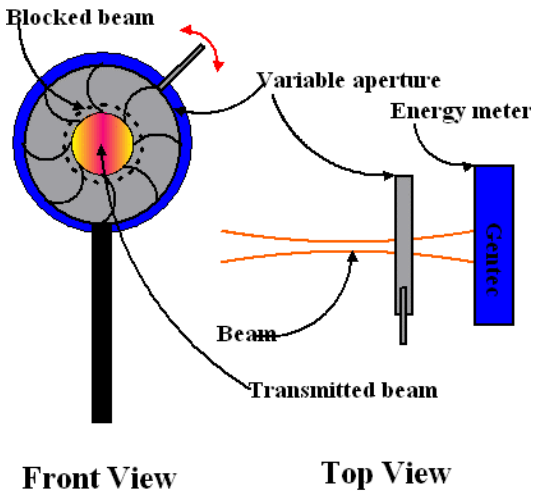

Figure 4-9: Variable-aperture method illustrated from the front and the top.

4.3 Beam radius definitions

Several definitions of the beam radius were made over the years based on these different profiles. Each definition is particularly suited for a specific application [4]. The moment definition of Chapter 2, which applies to energy density profiles, is theoretically the most complete definition. It also provides simple relations for calculating the radii and M^2 values for pure simple Gaussian modes (Section 3.3). It is for these reasons that the ISO recently made this definition the standard one. Other definitions are, however, better suited for practical applications.

4.3.1 Second moment radii

The second moment approach, as described in Chapter 2, was first formulated in 1979 by Carter for Hermitian beams [8]. The beam radii are obtained by using either two-dimensional (measured with a camera or pinhole) or one-dimensional (measured with a slit or pinhole) energy density profiles in Equations (2.4) or (2.5). Very precise scans of the beam profiles coupled with very good noise deducting algorithms are necessary to obtain the correct second moment radii.

This definition of the beam radius is well suited for beam quality measurements and for classifying non-conventional beams such as general astigmatic beams. It was made standard

by the ISO [24], as was already mentioned, and will be termed the standard beam radius definition. All other definitions are termed alternative beam radius definitions.

There are, however, a few complications with the second moment definition:

- The second moment method is a theoretically elegant way of defining the beam radius, but it is not very practical. There is for instance no straightforward relation between the second moment radius and the energy content radius, which is more suitable for energy flux calculations used in material processing.
- For some applications, it is necessary to trace a feature on the beam profile like a node or a local-maximum. There is also no common relation between these features and the second moment radius.
- Second moment radii are extremely sensitive to noise in the wings of the energy density profiles.
- It is sometimes not possible to measure the energy density profiles, which are used to calculate the second moment radii, due to low signal to noise ratios.

Another definition is usually employed when it is difficult to accurately measure entire energy density profiles. If any alternative definition is used for beam quality considerations it has to be shown that its beam radii are equivalent to those measured with the second moment definition [24].

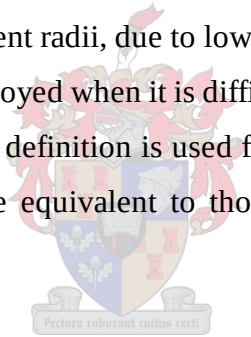

4.3.2 Energy density radii

An energy density radius is usually defined as half the distance between a specific feature on either side of the centre of a beam's energy density profile. Numerous attempts have been made in the past to standardise laser beam radii by using some version of this definition.

Bridges [7] proposed two features in 1975, the first of which was the largest radius between the centre of the beam and a point where the energy density is $1/e^2$ or 13,5% of the maximum. This percentage is referred to as the $1/e^2$ energy density clip-level and reduces to the Gaussian radius w_{00} for the fundamental mode. The second feature he proposed was the radius of the largest node of the highest higher order mode.

Zheng [56] et al proposed to fit a TEM_{00} profile to the data and then to use the Gaussian beam radius w_{00} (defined in Section 3.2.1.1) of the fitted profile. This technique is an option in many of the commercial camera software presently available on the market, but only works for beams which have almost an TEM_{00} profile.

4.3.3 Energy content radii

This definition of the beam radius originates from the moving knife-edge method. An energy content beam *radius* r_{EC} is defined as the distance between the transverse location of a lower energy point $e_K E$ and that of an upper energy point $(1\text{-}e_K)E$, where E is the total beam energy. These energy points (arrows in Figure 4-10) are referred to as clip-levels. Siegman [46] chose the clip-levels (e_K) of 10% and 90%, whereas the ISO chose clip-levels of 16% and 84%. Siegman's choice was based on correlating the knife-edge with the second moment method whereas the ISO's was chosen to match the fundamental mode radius.

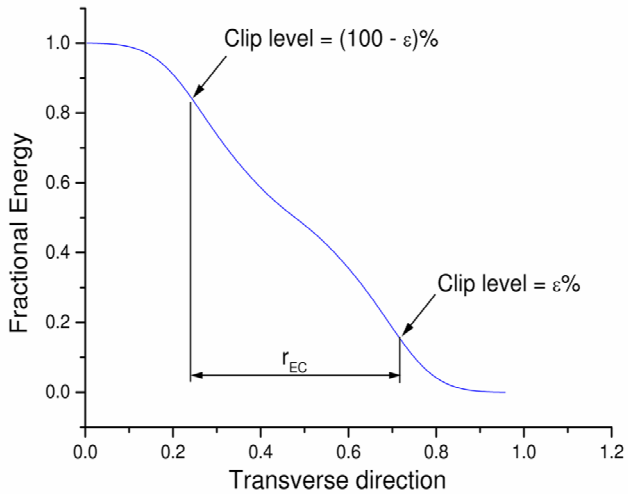

Figure 4-10: Illustration of how the energy content radii are defined.

A beam radius obtained by this method can be directly used to calculate the fluence, which is not possible with other methods unless the relationship between the beam radius and the energy content is known. Radii originating from the variable aperture method are also classified as energy content radii. The variable aperture radius of a beam is defined as the radius of the circular variable aperture (Section 4.2.5) which transmits a certain percentage e_V (the variable aperture clip-level) of the total beam energy. The radius of a variable aperture

that is reduced around a TEM_{00} beam will be identical to the Gaussian radius w_{00} if 86.5% of the total energy is transmitted [24].

4.4 Determining the beam radii from measured profiles

4.4.1 Manual acquisition

Siegman [46] proposed to manually scan the beam with a knife-edge and read off the distance between two knife-edge clip-levels. He did, however, suggest that more information could be obtained by measuring the entire knife-edge energy profile. The ISO [24] also proposed this method when alternative beam radius definitions are used (Section 4.5.3). A disadvantage of this method is that it is prone to human errors. The second moment radii can also not be directly obtained by this method.

4.4.2 Low frequency acquisition*

The beam is scanned in set intervals with a mechanical scanner. This method is usually employed to scan the beams from low frequency pulsed laser systems. The scanning edges are moved to set positions and the average over a certain number of shots of the transmitted energy is recorded. This method is best suited for knife-edge scanning. It can also be used for slit scanning using lots of very small intervals to obtain full energy density profiles from which the second moment radii can be calculated. Knife-edge radii can only be accurately determined from large interval scans by fitting appropriate functions to the data. (Such functions will be discussed in more detail in Section 4.4.4). Energy profile fitting is typically performed inside a mathematical program such as Matlab or Mathematica. The functions are then solved at predetermined clip-levels to obtain the alternative beam radii. Fitting of low frequency acquisition slit profiles with functions can be very unreliable as will be seen in Section 4.4.5.

4.4.3 High frequency acquisition

This type of scan is used predominantly for very high frequency pulsed or CW laser beams. A mechanical scanner is moved with a constant velocity across the beam and a fast large area detector records the average transmitted power [4]. The position of the scanner for a

* This technique was employed in this thesis to obtain the beam radii of a CO_2 TEA laser.

transmitted power level is accurately known if the speed and starting position of the mechanical device are also accurately known and the detector is fast enough. The resolution of the beam profile is therefore only dependent on the spatial and temporal resolution of the photo detector. This method can therefore be very accurate and affordable, making it highly attractive. The large number of data points can be directly inserted into integral (2.4) to obtain the second moment radius. Pixel counting techniques are used to obtain knife-edge or slit beam radii. These techniques are also used for camera profilers that have a large number of pixels in their CCD arrays [48].

4.4.4 Fitting of the energy profile

Diso et al [14] measured the entire knife-edge energy profile with the low frequency technique and fitted the TEM_{00} energy function (Equation (4.7)) to the data with the least squares method. They then used the Gaussian beam radius w_{00} (which they directly obtained from the fitted function) in subsequent quality calculations. This technique can lead to large errors for beams containing large percentages of higher order modes, because the TEM_{00} energy fitting function will not necessarily follow the measured data points. It is especially important to obtain good fits in the crucial 16% clip-level region. Figure 4-11 shows how a TEM_{00} function misfits data from a beam with large higher order mode content. This error can be minimized by adding the last term of the first higher order mode energy distribution (Equation (4.8)) to the fitting function.

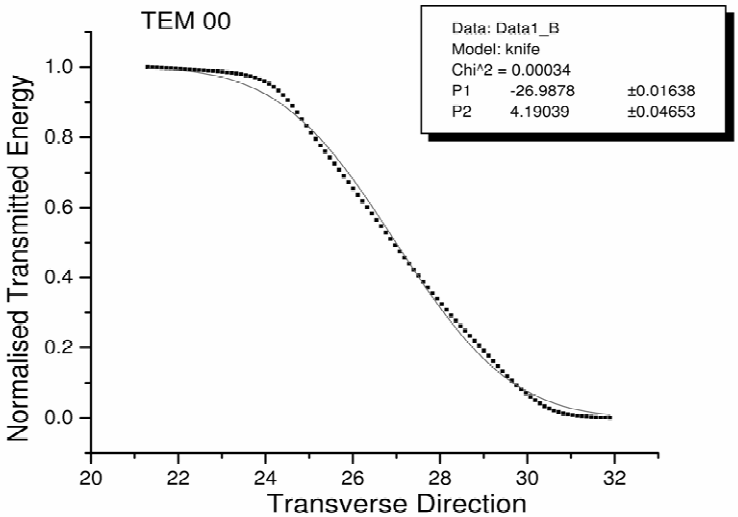

Figure 4-11:A TEM_{00} energy distribution mis-fitting the energy profile of a real higher order laser beam.

The TEM_{00} fitting function is directly found from Equation (4.7) by substituting P_1 and P_2 as the two fitting parameters for x_0 and $w(z)$ respectively.

$$y = \frac{1}{2}\left[erf\left(\frac{-\sqrt{2}(x-P_1)}{P_2} \right) + 1 \right] \tag{4.9}$$

It can be seen from a comparison between Equations (4.7) and (4.8) that there are many similarities between the knife-edge energy functions of the fundamental and first higher order mode. An extra higher order component is just added to the function of the fundamental mode to obtain the first higher order mode function. Accurate fittings can be obtained by adding a weight P_3 to control how much of this higher order component is added.

$$y = \frac{1}{2}\left(\frac{1}{2} erf\left(\frac{-\sqrt{2}(x-P_1)}{P_2}\right) + 1 \right) + P_3 e^{-2\left(\frac{x-P_1}{P_2}\right)^2} \frac{(x-P_1)}{P_2}\sqrt{\frac{2}{p}} \tag{4.10}$$

TEM_{00} component — Higher order component

The improvement is visually verified in Figure 4-12 by fitting the new function (4.10) using the same large higher order mode content beam of Figure 4-11. The chi-squared value (gives an indication of the fitting error from the least square method) decreased an order of magnitude from 0.00034 to 0.00009. Other higher order mode terms can also be added with ease since the first TEM_{00} parts for all the higher order mode distributions remain unchanged and only terms with uneven powers of x are found in the higher order functions (Appendix **A**). One does not deduce anything from the relative fitting parameters but only use the fitted function to obtain beam radii using clip levels. One could therefore also use other functions like polynomial fits.

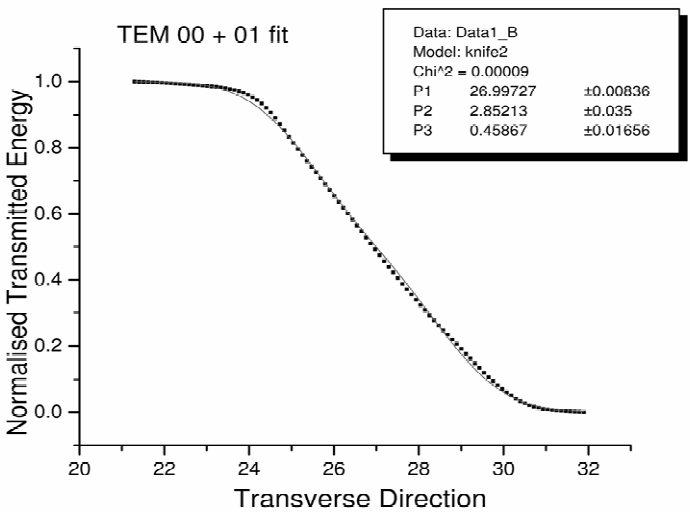

Figure 4-12:A $TEM_{x,y\ 00+01}$ energy function fitting the energy profile of a higher order beam.

4.4.5 Comparing energy and energy density profile fitting

The errors made when fitting a TEM_{00} energy density profile (Equation (3.20) with $m = n = 0$) to the slit profile of a beam that contains a percentage of a higher order mode is much larger than the errors made when fitting the TEM_{00} energy profile (Equation (4.7)) to the same beam's knife-edge profile. This can be observed by comparing the TEM_{00} energy density fit on the slit profile to the TEM_{00} energy fit on the knife-edge energy profile of the same beam with a higher order component in Figure 4-13. The errors made in the energy density fit are enormous compared to those of the energy fit. It is therefore not recommended to use fit techniques on energy density profiles.

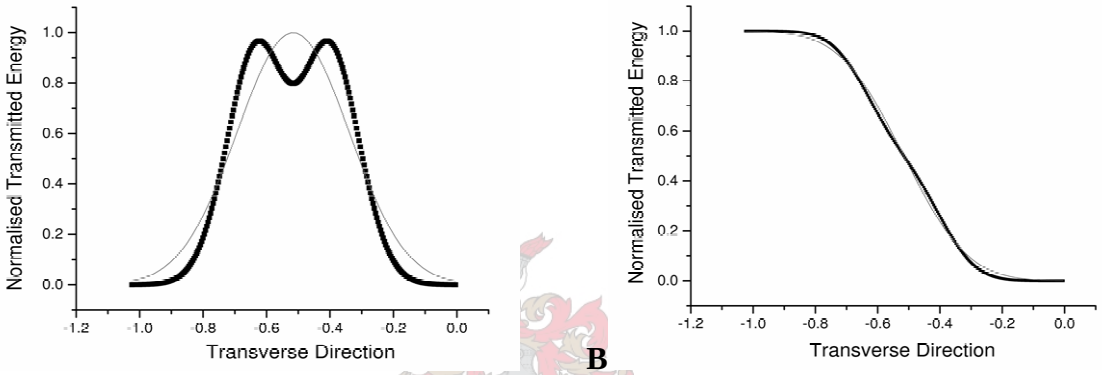

Figure 4-13: In A the fitting of the TEM_{00} energy density profile on the slit profile of a beam with a higher component can be seen. B shows the fitting of the TEM_{00} energy profile on the knife-edge energy profile of the same beam.

4.4.6 Determination of the principle axis for one-dimensional scans

The orthogonal Cartesian measuring edges (slit or knife-edges) are rotated until roughly equal beam widths are obtained in both directions. Beam measurements at each azimuthal angle can consist of only a few measuring points or be done manually. The edges are then rotated by 45° to yield the principle axis. Equation (2.17) can only be used if the entire two-dimensional beam energy density profile was measured with a camera or pinhole [24].

4.5 Correlations between the second moment and alternative radii

The second moment definition of the beam radius (Section 2.1.2) was standardised by the ISO and is best suited for quality considerations. The energy and energy density definitions are,

however, better suited for practical applications such as flux calculations and feature tracing. It is necessary to find correlations between the standard and different alternative definitions to fully characterise a laser beam spatially. Researchers have attempted to do this for years, but correlations proved elusive since it was found that there is not a general one-to-one relationship between the second moment and alternative methods [44]. The second moment radii can also only be determined directly from a large number of measuring points which are inserted into the noise sensitive second moment integral (Equation (2.4)). For some applications, this large amount of data points is impractical (especially for manual scans). For other set-ups, the entire beam cannot be accurately slit or pinhole scanned at all due to a low signal to noise ratio. Correlating the second moment definition with alternative ones is therefore still very relevant. In the next few sections, methods are described to correlate between the second moment and alternative methods.

4.5.1 Measurement of correlation factors: the SPSM method

Simple astigmatic beams do not rotate or change their energy density profile during propagation (Section 2.2.3) so that the relationship between the second moment radii and alternative radii remains invariant. It is therefore only necessary to determine this relationship at one position along the beam propagation direction. This can be done by carefully measuring the energy density profile at this position and then determining the second moment and alternative radii from it. The energy profile that is needed to determine the knife-edge radius is not physically measured, but rather obtained by mathematically integrating a slit profile (Section 4.2.4). The entire beam is then characterised by means of an alternative method and the correlation applied to each radius to determine the second moment propagation and M -value. This method is termed the single position slit measured (SPSM) correlation method.

This method is probably the most straightforward and simple to implement, but it does have some disadvantages. Plasma formation [1], [11] is sometimes encountered on scanning edges at the artificial waist. The beam needs to be attenuated to eliminate this, which in turn reduces the signal to noise ratio. If the signal has to be reduced by a large amount only the knife-edge method can be used to scan the beam. To measure the correlation factor the attenuator has to be removed to perform a single slit energy density scan some distance from the waist. The knife–edges also have to be removed and replaced with slits. These two extra operations have

to be done very carefully to ensure that the beam does not shift and that the two scanning devices have the same azimuthal angle. It is also very difficult to implement this in commercial systems. To avoid this, mathematical correlations have been developed and are discussed in the following sections.

4.5.2 Siegman's knife-edge correlation for rectangular Gaussian beams

Siegman investigated the effect that clip-levels value (e_K) have on the relationship between the energy content radius r_{EC}, and the second moment radius $\langle w \rangle$ [46]. He used a graphical approach by plotting the knife-edge transmitted (fractional) energy versus the clip width D_c (knife-edge radius) normalised to the standard deviation $\langle x^{2nd} \rangle$ as defined in Equation (2.4). He did this for several commonly found beams overlaying each other. The fractional energy was used as the clip-level e because it was normalised to one. Siegman mostly examined lower and higher order Hermite Gaussian beams. He also included a few peculiar beams such as diamond, picture frame, top hat, slit and doughnut shaped beams. His aim was to find a common relationship between a wide range of energy-content and the second moment beam diameters at an optimum knife-edge clip-level.

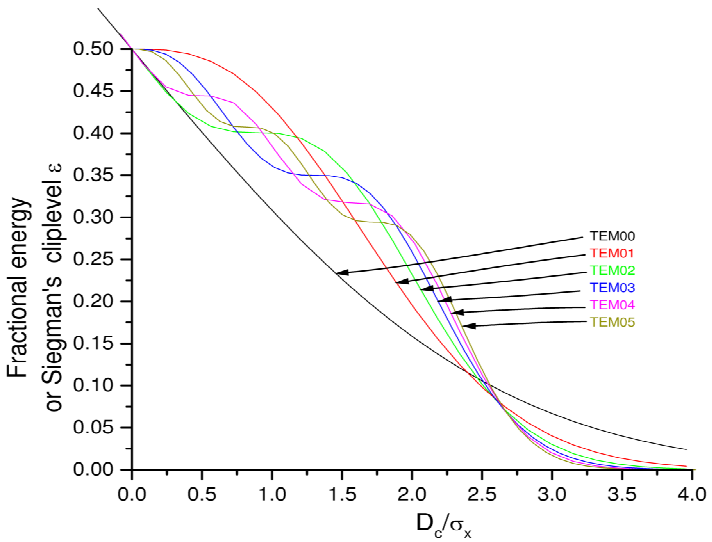

Figure 4-14:Siegman's clip-level plot for higher order rectangular Hermitian modes.

Siegman's approach was to find a clip-level where the correlation factor D_c / s_x is, within certain error limits, roughly the same for all the commonly investigated beams. This implies that he sought a converging point when plotting these moment-normalised graphs overlaying each other. In one of his graphs, he plots the fractional energy of the first seven higher order modes versus D_c / s_x (Figure 2 of [46]). A Similar composition up to mode TEM_{xy} 05 is shown in Figure 4-14. In an expanded view shown in Figure 4-15, it can be seen how he found that there was indeed almost a converging point at a clip-level of around 8%. For all practical purposes all the modes converge to a point at this clip-level, with the exception of the TEM_{00} mode. The TEM_{00} mode cuts the other modes at significantly higher clip-levels. His eventual finding was to use a clip-level of 10% and a resulting correlation factor of 2.563 as a compromise. The energy content radius is then related to the second moment radius with the following function at a clip-level of 10%:

$$\langle w \rangle = 0.7805 w_c \,. \tag{4.11}$$

One drawback of this approach is that most laser beams do not consist of pure modes, but rather of a superposition of them [45]. Siegman tried to address this problem by adding an error graph for mixtures of two adjacent higher order Laguerre modes (Fig 8 of [46]). Siegman also identified pedestal beams as being problematic. These beams consist of a good quality central beam with a surrounding bad quality pedestal. He listed these beams as extreme, implying that their parameters fall outside the ones he suggested. A new correlation between the energy and second moment radii should attempt to describe these beams as well.

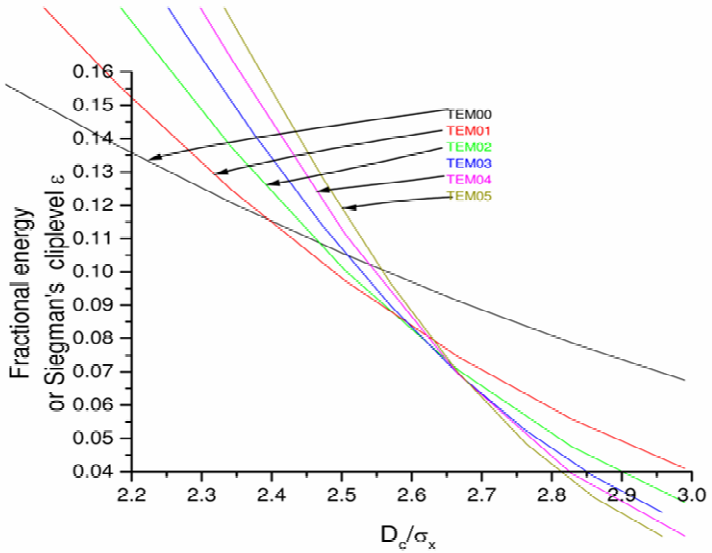

Figure 4-15:Expanded View of Siegman's clip-level plot for higher order modes.

4.5.3 Correlations from ISO standard 11146

The ISO in a normative Annex to the standard provided the following correlation functions between the beam quality factor determined with the second moment and three alternative definitions [24]:

$$M_s = c_i(M_i - 1) + 1 \tag{4.12}$$

where

- M_i is the square root of the "times diffraction limit" or beam quality factor M_i^2 according to an alternative method i and
- c_i is the correlation factor between the alternative method i and the second moment method.

The correlation constants c_i for the three methods are listed in Table 4-1 [24].

Alternative Method	c_i	Clip-level
Variable-aperture	1.14	86,5%
Moving Knife-edge	0.81	16%
Moving Slit	0.95	13,5%

Table 4-1:ISO correlation constants between the second moment and alternative definitions of the beam radius.

The ISO also provided a relation to determine the second moment beam diameters d_c from the alternative diameters d_i [24]:

$$d_s = \frac{d_i}{M_i}\left[c_i(M_i - 1) + 1\right]. \tag{4.13}$$

Johnston et al. [27] measured these correlations experimentally with the help of an ion gas laser. The results were confirmed for high power CO_2 lasers up to 1kW, with M^2 factors up to 4 and with radially symmetric beams [24]. Johnston measured the pin-hole profiles of six beams that were created by adjusting a variable-aperture within the ion gas laser resonator. These one-dimensional pinhole profiles were then fitted with linear combinations of the pure Laguerre modes to give six realistic, but theoretical mode profiles. The second moment, knife-edge, slit and variable-aperture diameters were then calculated from these fitted profiles. Graphs with $d_i / d_{00} - 1$ versus $d_{2\text{nd mom}} / d_{00} - 1$ were then fitted to obtain the correlation factors c_i.

The reason why the relationship between these two parameters was fitted was so that the M^2 determined with the alternative beam radius definitions, are real M^2 values. This implies that for a TEM_{00} beam, Equation (4.12) must reduce to one, which is a very basic prerequisite for a beam quality factor. The clip-levels for each of these methods had to be chosen correctly to guarantee this (See Table 4-1). These clip-levels are actually rounded off values with the result that the M^2 value does not reduce exactly to one for TEM_{00} beams.

These correlations were determined experimentally from only six profiles from an uncommon laser resonator with a specific symmetry making the applicability of this method very limited. In the next section, a theory to test old correlation methods and to develop new ones is presented.

4.5.4 Novel comprehensive correlation method

The second moment propagation equation (Equation (2.12)) can be rewritten in terms of the second moment M^2 factor using Equation (2.23)

$$\langle w(z)\rangle = \langle w_0\rangle \sqrt{1+\left(\frac{l M^2_{2nd} z}{p\langle w_0\rangle^2}\right)^2} \tag{4.14}$$

so that

$$M^2_{2nd} = \frac{p\langle w_0\rangle^2}{z\,l}\sqrt{\left(\frac{\langle w(z)\rangle}{\langle w_0\rangle}\right)^2 - 1} \tag{4.15}$$

This equation is used to determine the second moment beam quality by measuring second moment radii at several positions along the beam propagation direction. When an alternative definition is used to obtain the beam radii of simple astigmatic beams the measured radii deviate by a constant factor k from the second moment radii. This is because the shape of the beam profile of simple astigmatic beams does not change when the beam propagates. Only the second moment radius change. (Section 2.2.2).

There is a constant scale factor k between alternative beam radii are and the second moment radius of a specific beam.

$$w_{alt} = k\langle w(z)\rangle . \tag{4.16}$$

This k factor is a constant for both intensity-based radii (slit) and energy base radii (knife) of a specific beam. It is easily proven in Appendix H.

The new or alternative M^2-value determined by measuring the beam radii with an alternative method at several positions along the beam propagation would then be according to Equation (4.15)

$$M^2_{alt} = \frac{p\left(k\langle w_0\rangle\right)^2}{z\,l}\sqrt{\left(\frac{k\langle w(z)\rangle}{k\langle w_0\rangle}\right)^2 - 1} \tag{4.17}$$

$$M^2_{alt} = \frac{p\,k^2\langle w_0\rangle^2}{z\,l}\sqrt{\left(\frac{\langle w(z)\rangle}{\langle w_0\rangle}\right)^2 - 1} \tag{4.18}$$

$$M^2_{alt} = k^2 M^2_{2nd} \tag{4.19}$$

so that

$$M_{alt} = kM_{2nd}\,. \tag{4.20}$$

Please note that k's value can vary for different beams and is different from Equation (4.12) which are claimed to be valid for a large subset of beams.

From Equations (3.19) and (3.20) it can be deduced that all energy density functions of higher order modes are scaled with the fundamental mode with radius $w_{00}(z)$ (the Gaussian radius). At any position along the beam propagation direction according to Equation (3.39):

$$M_{2nd} = \frac{\langle w(z)\rangle}{w_{00}(z)} \tag{4.21}$$

To compare the different beam radii we choose for convenience the Gaussian radius w_{00} as one. The same technique was employed by Johnston [27]. Equation (4.21) then becomes

$$M_{2nd} = \langle w(z_s)\rangle\,. \tag{4.22}$$

From Equations (4.16), (4.20) and (4.22) it is now found

$$M_{alt} = \frac{w_{alt}(z_s)}{\langle w(z_s)\rangle}\langle w(z_s)\rangle \tag{4.23}$$

so that

$$M_{alt} = w_{alt}(z_s) \tag{4.24}$$

and finally

$$M_{2nd} = \left(\frac{1}{k}\right) M_{alt} = cM_{alt} \tag{4.25}$$

with

$$c = \frac{\langle w(z_s) \rangle}{w_{alt}(z_s)}. \tag{4.26}$$

Using these relations, the proportionality factors c can be plotted as a function of their alternative M -values using only single energy density profiles for a large number of different beams. If enough beams are evaluated, functions can be fitted through the proportionality factors to obtain correlation functions.

Note that no specific clip-level was used for the derivation. Any suitable clip-level can therefore be employed in the calculations. This is very similar to the technique Johnston [27] used to obtain a correlation. The main difference is that it is not assumed that there is a general linear relationship between the different methods. If a linear relationship exists between the second moment and alternative definitions, all the proportionality factors will remain constant for all the knife-edge M -values smaller than two [24]. A graph of the proportionality factors versus M-values is therefore a direct measure of the deviation from a linear relationship between the standard and alternative definitions.

Note also that because of Equations (4.22) and (4.24) either M or w can be used during discussions on correlation methods. It is for this reason that this thesis rather aims to correlate the different definitions of M rather than M^2. The ISO Annex also followed this approach.

4.6 Summary

Different methods and apparatus to measure beam profiles of laser beams have been reviewed. Different definitions of the beam radius closely related to these beam profiles have also been given. Attempts to find a relation between the standard and alternative beam radius definitions have been examined and a new proportionality factor was proposed. In the next chapter, programs are presented with which to calculate the newly proposed proportionality factors and to evaluate existing correlation functions.

Chapter 5

Computational techniques to calculate the proportionality factors

In this chapter, various programs to calculate the second moment, knife-edge and slit M -values of a very large group of beams will be presented. These values can be used to determine the accuracy of existing correlation functions and to develop new correlation methods.

5.1 Generation of representative beams

5.1.1 Linear mode combinations

Sufficiently large numbers of sample laser beams should be used to determine the accuracy of the existing correlation techniques (Section 4.5) and to develop new methods. Two good types of commonly found beams to use are the rectangular and cylindrical symmetric Gaussian modes and their respective linear combinations (discussed in Chapter 3). Siegman used mainly pure rectangular modes, while Johnston and the ISO used measurements and models of cylindrical symmetric beams.

It can be expected that real lasers divide the available energy from the gain medium between different modes in some sort of distribution. One can typically expect the TEM_{00} mode to receive the most and the highest order mode the least amount of total available energy. It has, however, been shown that for a CO_2 TEA laser the relative amount of energy that is allocated to the different modes can be changed by changing the gas mixture [31], [15], [16]. It is therefore not possible to use an energy allocating distribution for different modes. One way to include all possible mode combinations in a general theory is to multiply the pure mode-distributions with random weights in a linear combination. Such a theory would therefore

describe a laser resonator in which all the modes have equal probability to lase. Such a resonator is now defined as an equal probability resonator. If any energy allocating distribution is multiplied with such a random linear combination, the result would again be a random linear combination. The only deviation from real laser resonators, with energy allocating distributions, would be that statistically more beams with a set number of modes will be found at lower beam quality values. Any conclusions from statistical variations therefore have to take into account the fact that energy-allocating distributions do occur in practise. The equal probability resonator has the further advantage of being able to describe beams consisting of pure, or very close to pure, higher order modes as would be found when there are irregularities within a resonator.

To obtain an arbitrary energy density profile for a sample beam, two-dimensional energy density profiles of pure modes (each with a w_{00} equal to one (Section 3.2.1)) are multiplied with random weights and then added in a linear superposition:

$$y = c_{\text{rand }1} y_{\text{ rand }1} + c_{\text{rand }2} y_{\text{ rand }2} + \ldots\ldots c_{\text{rand n}} y_{\text{ rand n}} \tag{5.1}$$

Equation (5.1) does not have any cross terms because the electric field functions, from which the energy density distributions are calculated, are orthogonal to each other for simple laser systems [45], (Section 3.2.1). It must be noted that in reality non-orthogonal components can potentially be introduced by elements within resonators [39].

The second moment radii are usually calculated from this two-dimensional energy distribution. The slit profile is obtained by integrating this two-dimensional energy density profile either numerically or analytically according to Equation (4.1). The knife-edge profile is obtained by integrating the slit profile in turn either numerically or analytically according to Equation (4.5). The slit and knife-edge radii can then be calculated from the two profiles. All these radii values are equal to their respective M -values of the sample beam according to Equations (4.22) and (4.24) because w_{00} was chosen as one.

Practical laser resonators contain a finite number of modes due to design apertures and finite gain medium cross sections. It is therefore logical to limit the number of pure modes used to calculate the energy density profile of a sample beam. Attention should be given to how real resonators select the maximum number of modes it can contain when deciding which modes

should be used in a practical linear combination [23],[26], [37], [35]. Consider for example a simple cylindrical symmetric resonator with a single circular mode-restricting aperture [23] (Figure 3-1). As the mode restricting circular aperture is opened up, higher order modes start to lase in succession inversely proportional to the percentage of their energy that is cut off by the aperture. Modes with smaller radii therefore start to oscillate before larger ones. This selection for cylindrical symmetric beams is not at all trivial to determine from theory since there are various definitions of beam radii (Section 4.3). Both the second moment and variable aperture radii make use of a cylindrical integral. Table 5-1 lists the second moment and variable aperture radii (normalised to the fundamental) of the first few cylindrical symmetric modes according to Johnston [27]. It can be observed that there are modes that have the same second moment radii, but whose variable aperture radii vary significantly. For such beams it would be logical to rather evaluate their respective variable aperture radii to determine which will lase first due to the fact that the shape of the mode restricting aperture is circular. This illustrates once again that the second moment definition cannot stand on its own as the only available definition of beam radii. The variable aperture radius definition therefore has applications outside laser characterisation and is still relevant.

Cylindrical mode	Second moment radius Normalised to TEM_{00}	Variable aperture radius Normalised to TEM_{00}
TEM_{00}	1.00	1.00
$TEM_{pl}01$	1.41	1.32
$TEM_{pl}10$	1.73	1.64
$TEM_{pl}02$	1.73	1.56
$TEM_{pl}11$	2.00	1.88
$TEM_{pl}03$	2.00	1.76

Table 5-1: Second moment and variable aperture radii (normalised to the fundamental) of the first few cylindrical symmetric modes according to Johnston [25].

The phenomenon that different modes have identical second moment radii is not encountered in rectangular symmetry. The only possible similarity is where modes have the same radius in the two different Cartesian coordinates. These two modes will both start to lase at the same minimum circular aperture radius if the laser has perfect alignment, perfect optics and a

uniform gain profile. Under these conditions, it is also more likely that cylindrical symmetric modes will lase instead.

5.1.2 Cylindrical symmetric beams and rectangular scanning devices

The knife-edge and slit both are rectangular symmetric scanning devices and are best suited to scan rectangular symmetric beams consisting of superpositions of Hermitian modes. However, complications do arise when they are used to scan cylindrical symmetric beams consisting of superpositions of pure Laguerre modes. The general equation for two-dimensional cylindrical energy density distributions (Equation (3.15)) can be converted to Cartesian coordinates as follows:

$$I_{x,y}(x,y,z) = k\left(\frac{2(x^2+y^2)(z)}{w^2(z)}\right)^l\left[L_p^l\left(\frac{2(x^2+y^2)(z)}{w^2(z)}\right)\right]e^{-\frac{2(x^2+y^2)(z)}{w^2(z)}}\begin{Bmatrix}\cos^2\left(l\cos^{-1}\dfrac{x}{\sqrt{x^2+y^2}}\right)\\ \sin^2\left(l\sin^{-1}\dfrac{y}{\sqrt{x^2+y^2}}\right)\end{Bmatrix} \quad (5.2)$$

When Equation (5.2) is inserted into either the mathematical approximations of the slit (Equation (4.1)) or knife-edge (Equation (4.5)) the following integral is encountered which is not analytically solvable.

$$\iint_{\text{cartesian x,y}}\left(\frac{2(x^2+y^2)(z)}{w^2(z)}\right)^l\left[L_p^l\left(\frac{2(x^2+y^2)(z)}{w^2(z)}\right)\right]e^{-\frac{2(x^2+y^2)(z)}{w^2(z)}}\begin{Bmatrix}\cos^2\left(l\cos^{-1}\dfrac{x}{\sqrt{x^2+y^2}}\right)\\ \sin^2\left(l\sin^{-1}\dfrac{y}{\sqrt{x^2+y^2}}\right)\end{Bmatrix}. \quad (5.3)$$

This integral leads to several complications when the different radii are calculated for cylindrical symmetric beams as will be seen in the next few sections.

5.1.2.1 Separability and the $TEM_{pl}P0$ modes

One of the effects of the non-separability can be seen by comparing the slit profile of the pure $TEM_{pl}20$ mode (Figure 3-6 A, B) with its one-dimensional pinhole profile in Figure 5-1.

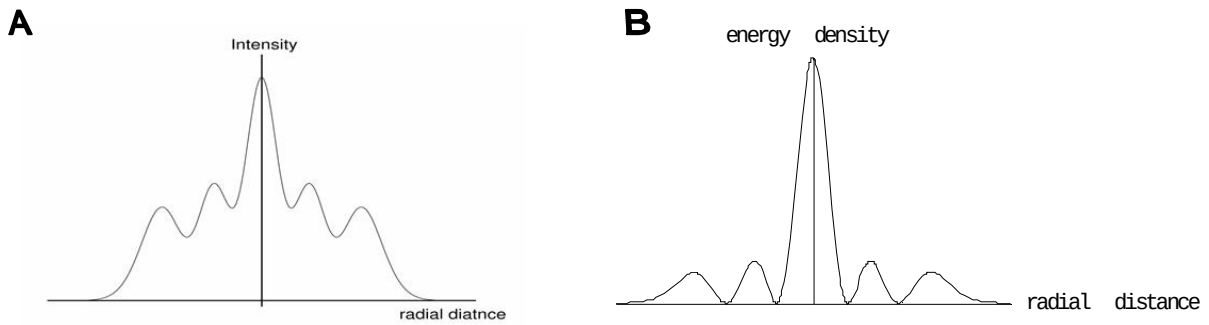

Figure 5-1: The difference between a slit profile (A) and a radial pinhole profile (B) of the cylindrical $TEM_{pl}20$ mode.

The two profiles are clearly very different which implies that their second moment, slit and knife-edge radii will also be different. The slit profile is the logical choice from which to calculate the slit and knife-edge radii. The second moment radius is usually calculated by inserting the full two-dimensional energy density distribution into the cylindrical second moment integral (Equation (2.5)). It would be simpler to rather use either the one-dimensional slit or pinhole profiles in the calculation of the second moment radius since it requires vast computer memory resources or very long calculation times to use the full two-dimensional energy density distributions. The second moment radii of the slit and one-dimensional pinhole profiles of the $TEM_{pl}20$ mode were calculated with the rectangular symmetric second moment formula (Equation (2.4)) as 1.732 and 2.237 respectively. Only the slit profile's second moment M -value corresponds to the theoretically correct two-dimensionally calculated value given by Equation (3.38). The value calculated from the one-dimensional pinhole profile differed significantly from the theoretical value. It can be seen in Table 5-2 that the slit profiles also provided the correct second moment radii for other pure $TEM_{pl}P0$ cylindrical symmetric modes. It is also verified using the cylindrical $TEM_{pl}10$ mode that the slit profiles provide the correct values for the knife-edge and slit radii of the $TEM_{pl}P0$ cylindrical symmetric modes (according to Johnston [27]). Note that the one-dimensional pinhole profiles provided incorrect radii for these values. The correct slit, knife-edge and second moment radii can therefore be calculated by using the slit profiles in one-dimensional integrals.

	Theory			Slit profile			Pin-hole profile		
Circ mode	2^{nd} mom radii	Knife-edge radii	Slit radius	2^{nd} mom radii	Knife-edge radii	Slit radii	2^{nd} mom radii	Knife-edge radii	Slit radii
TEM_{00}	1.00	1.00	1.00	1.00	1.00	1.01	1.00	1.03	0.99
$TEM_{pl}10$	1.73	1.99	1.66	1.73	1.99	1.67	1.53	1.37	1.48
$TEM_{pl}11$	2.24			2.24	2.51	2.15	1.88	1.59	1.77
$TEM_{pl}30$	2.65			2.64	2.95	2.55	2.16	1.59	0.786

Table 5-2: The left column contains theoretical published radii of a few cylindrical symmetric modes [27]. The middle column contains the corresponding radii calculated from slit profiles. The right column contains the corresponding radii calculated from one-dimensional pinhole profiles.

5.1.2.2 The $TEM_{pl}0l$ modes

The focus so far has only been on the $TEM_{pl}P0$ modes. Additional complications arise when the $TEM_{pl}0L$ modes are investigated. For example, it was seen that that the two-dimensional energy density profile of the cylindrical symmetric $TEM_{pl}01$ mode is identical to that of the rectangular symmetric $TEM_{mn}01$ mode but that their properties are not (Section 3.3.1). The rectangular second moment radius of $TEM_{mn}01$ calculated with Equation (2.4) equals $\sqrt{3}$ and the cylindrical second moment radius of $TEM_{pl}01$ calculated with Equation (2.5) equals $\sqrt{2}$. This is due to the fact that in the second moment radii calculations, cylindrical integration (Equation (2.5)) was performed on $TEM_{pl}01$ and rectangular integration with Equation (2.4) on $TEM_{mn}01$. The two integrals differ and therefore the second moment radii differ as well. Rectangular integration requires that the azimuthal angle between a mode and the beam reference frame be defined and remain static in time. Cylindrical symmetric beams are not allowed to have one preferential Cartesian direction. All azimuthal directions should therefore have equal probability to contain a zero intensity node, or any other specific feature. This is automatically imposed by using cylindrical symmetric integration.

The cylindrical symmetry has to be maintained when cylindrical symmetric modes are used in numerical calculations involving rectangular scanning devices. The $TEM_{pl}P0$ modes are automatically cylindrical symmetric, but the $TEM_{pl}0L$ modes are not. It should be just as likely to find a minimum at the azimuthal position of a maximum and vice versa. When two

identical, two-dimensional mode structures which are each shifted so that the maxima of the one coincides with the minima of the other are combined, perfect cylindrical symmetric or doughnut modes are formed. Further additions are unnecessary because the resulting structure already has perfect cylindrical symmetry. The formation of the first three cylindrical symmetric two-dimensional $TEM_{pl}0L$ profiles can be seen in Figure 5-1 and is identical to time integrating these pure cylindrical mode profiles.

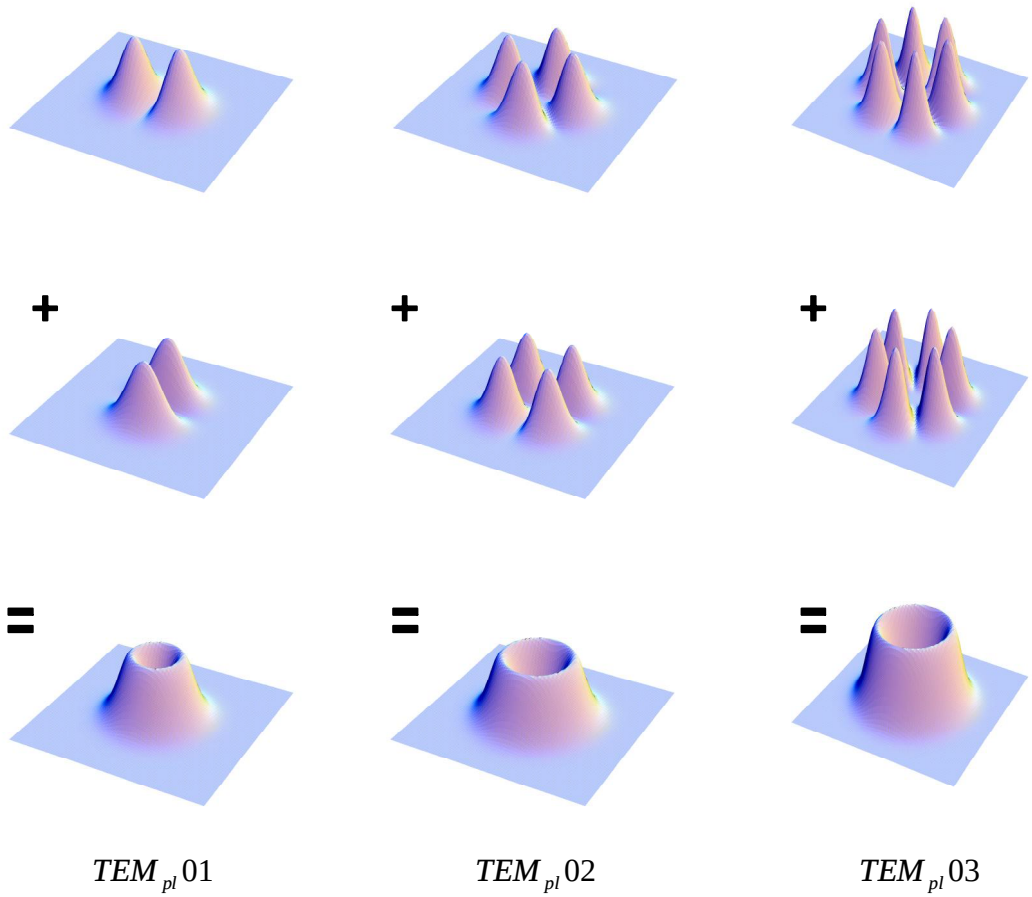

Figure 5-2: Formation of the correct two-dimensional cylindrical symmetric $TEM_{pl}0L$ profiles to be used in numerical calculations.

It can be seen from Table 5-3 that the second moment radii determined from the slit profiles of the cylindrical symmetric doughnut mode profiles are found to correspond exactly with theory [23], (Equation (3.32)). The second moment values determined with the slit profiles of the non-rotated mode profiles correspond only occasionally when one preferential axis is chosen. It can furthermore be seen from Table 5-3 that the knife-edge and slit radii of only the doughnut modes also correspond with the theoretical values provided by Johnston [27]. Very few of the knife-edge and slit values calculated from the non-rotated profiles correspond to

these values. The cylindrical symmetric doughnut profiles of the $TEM_{pl}0L$ modes are therefore the correct ones to use in cylindrical symmetric calculations.

	Theory			Choose preferential direction			Doughnut profile		
Circ mode	2nd mom radii	Knife-edge radii	Slit radii	2nd mom radii	Knife-edge radii	Slit radii	2nd mom radii	Knife-edge radii	Slit radii
$TEM\,00$	1.00	1.00	1.00	1.00	1.00	1.01	1.00	1.00	1.01
$TEM_{pl}\,01$	1.41	1.53	1.42	1.73	1.87	1.50	1.41	1.53	1.41
$TEM_{pl}\,02$	1.73	1.92	1.68	1.73	1.99	1.67	1.73	1.91	1.68
$TEM_{pl}\,03$	2.00	2.26	1.88	2.00	2.32	1.80	2.00	2.25	1.89

Table 5-3: The left light shaded area contains published radii of a few cylindrical symmetric modes [27]. The middle slightly darker shaded area contains the corresponding radii calculated from slit profiles of the non-rotated profiles. The right darkest shaded area contains the corresponding radii calculated from slit profiles of the cylindrical symmetric doughnut modes.

5.1.2.3 Generation of cylindrical sample beam profiles

Equation (5.1) is the two-dimensional energy density distribution of a sample beam consisting of n number of modes. Adding the two-dimensional distributions together for each sample beam would either require enormous amounts of computer memory or very long calculation times. A simpler solution is therefore needed. It was already established that the slit profiles could be used to determine the second moment radii of beams by means of one-dimensional integration. According to Equation (4.1) the slit profile of a sample beam (Equation (5.1)) is

$$\int_{-L}^{+L}\int_{x_p-W}^{x_p+W} y\,dxdy = \int_{-L}^{+L}\int_{x_p-W}^{x_p+W} c_{\text{rand }1}y_{\text{ rand }1} + c_{\text{rand }2}y_{\text{ rand }2} + ...c_{\text{rand n}}y_{\text{ rand n}}\,dxdy \qquad (5.4)$$

So that

$$\int_{-L}^{+L}\int_{x_p-W}^{x_p+W} y\,dxdy = c_{\text{rand }1}\int_{-L}^{+L}\int_{x_p-W}^{x_p+W} y_{\text{ rand }1}dxdy + c_{\text{rand }2}\int_{-L}^{+L}\int_{x_p-W}^{x_p+W} y_{\text{ rand }2} + ...c_{\text{rand n}}\int_{-L}^{+L}\int_{x_p-W}^{x_p+W} y_{\text{ rand n}}\,dxdy \qquad (5.5)$$

The slit profile of a sample beam can therefore be obtained from the randomised sum of the correct slit profiles of the pure modes. These one-dimensional profiles reduce the memory

requirements of a program to manageable levels so that large amounts of computations can be done in a relatively short time. Both the second moment and slit radii are calculated from this slit profile. The knife-edge energy profile can be obtained by numerically integrating Equation (5.5). The knife-edge energy radius is then obtained from this knife-edge profile.

5.2 Calculation of the different beam radii

Programs can be written to obtain the differently defined beam radii (Section 4.3) of the random sample beams. Proportionality factors between the different radii from a large number of sample beams can then be used to find general correlations between different definitions of M (Section 4.5.4). Such programs should have the structure seen in Figure 5-3.

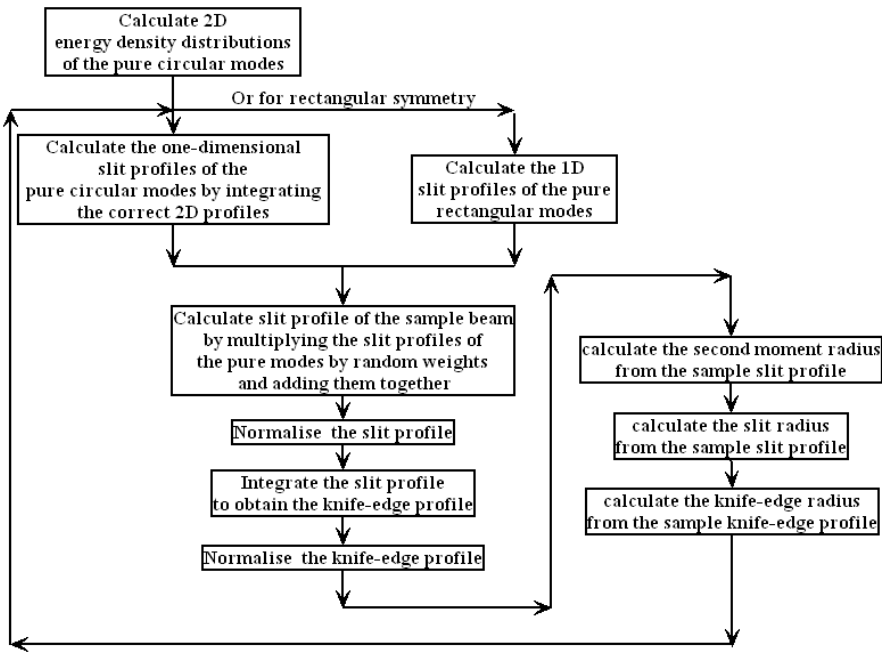

Figure 5-3: General structure of a program that calculates the different radii of randomised sample beams.

5.2.1 Numerical Programming

The widely available Microsoft program *Excel* was used to numerically calculate the second moment, slit energy density and knife-edge energy radii. The cellular nature of the numerical program made it similar to the separate pixels of a CCD camera. Results obtained from this program should therefore reflect real mathematical challenges faced in camera profilers. The

program could, however, not be included in this thesis because it was written over several sheets making it physically too large.

5.2.1.1 Two-dimensional cylindrical energy density distributions

A 255 by 255-cell matrix with variable grid size was used to generate two-dimensional energy density distributions of the normal pure cylindrical symmetric modes. Each cell was assigned a unique x and y position. The energy density value of each cell was obtained by substituting these x and y values into Equation (5.2). Both the pure $TEM_{pl}P0$ and $TEM_{pl}0L$ modes had to be used in the linear combinations since they have different slit profiles. This was not necessary for rectangular symmetric beams since they are separable in Cartesian coordinates. The matrices for the doughnut profiles were obtained as described in Section 5.1.2.2. In Appendix B the two-dimensional value matrices can be seen for the normal and doughnut $TEM_{pl}01$ modes. The energy density contour profile is visible due the fact that equi-energy density lines have identical values and therefore identical recognisable shapes.

5.2.1.2 The slit energy density profile

A slit integrates the two-dimensional energy density distribution only in one Cartesian direction. Slit integration was simulated for cylindrical symmetric beams by adding up each column of the two-dimensional energy density cell grid. The resulting row of values then represents the slit energy density profile. This process is illustrated in Figure 5-4. The numerical integration is much like the actual slit scanning process where the beam is scanned in discrete steps. This is also done in post-processing programs of CCD cameras which have a finite number of pixels. For rectangular symmetric beams, only the one-dimensional energy density profiles were needed because the one-dimensional pinhole profiles are identical to the slit profiles due to the separability of the rectangular modes in the Cartesian coordinates (Appendix C). An arbitrary linear combination for a particular sample beam was generated by multiplying slit integrated rows of all the participating modes by random numbers between zero and one and adding them all together to obtain a linear superposition according to Equation(5.5).

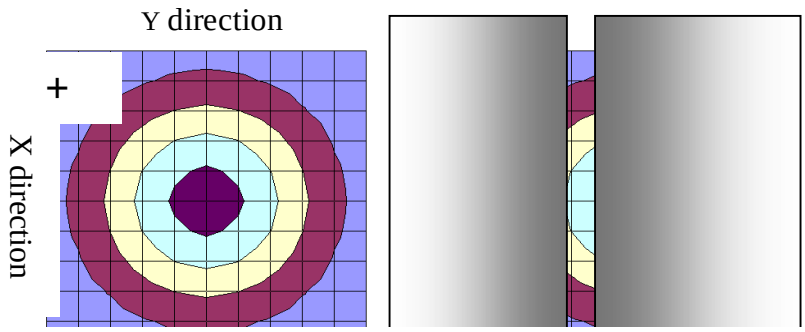

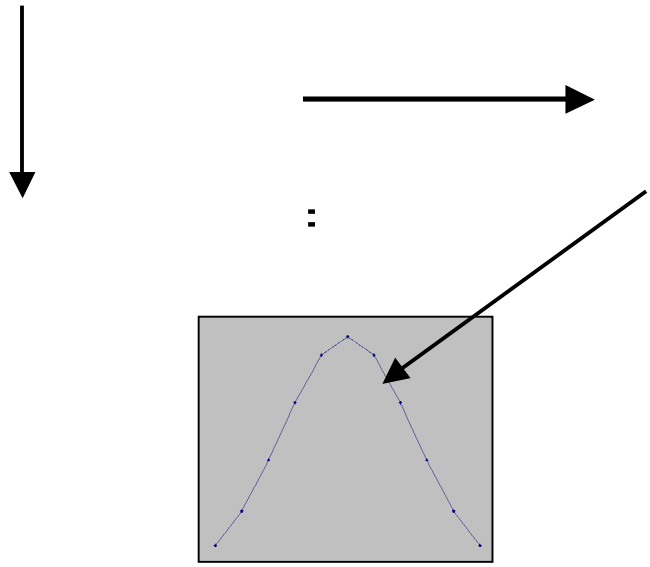

Figure 5-4: Generation of the slit energy density profiles by means adding rows in the two-dimensional energy density grid.

The randomised slit energy density profiles were normalised to the highest value. These slit energy density profiles were the sample beams that were used to calculate the second moment and slit radii. The energy density profiles of one hundred sample beams were generated in this way. A sheet was also created where weights for all the modes could be entered manually to get a visual perception of how the modes added up. A normalised two-dimensional energy density graph and a one-dimensional slit profile of this manually created beam were then automatically generated.

5.2.1.3 The knife-edge energy profile

The knife-edge profiles were obtained by adding the average of adjacent cell values of the slit profile in a cumulative summation. The resulting energy profiles from which the knife-edge energy radii can be calculated are similar to real scans in which steps or pixels are used to obtain the knife-edge radii. If integration was performed by adding up the full values of the slit profile cells, an extra energy density of half the difference between two adjacent values would be added per summation. The accumulative effect shifts the energy profile to noticeably higher incorrect values. The error is made because the index values of the cell positions are discrete and are in fact only precisely correct for the centre of the cell. This is illustrated in Figure 5-5.

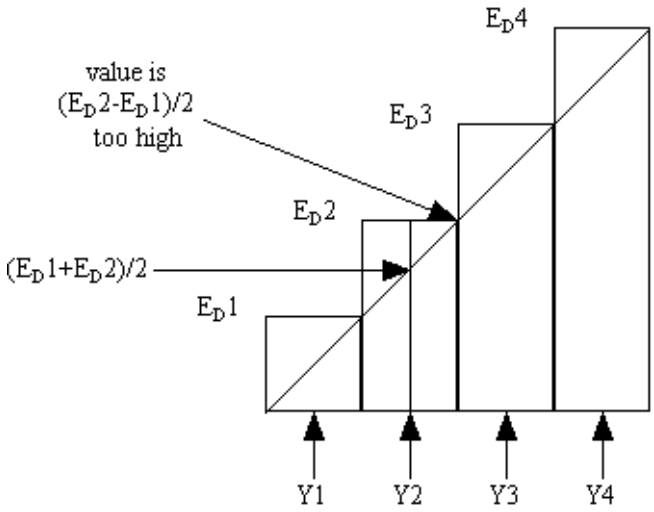

Figure 5-5: The origin of erroneous knife-edge profiles by erroneous addition of slit energy density cell values.

5.2.1.4 The calculation of the second moment radii

The second moment radii were calculated by means of Equation (2.4) with $\left\langle x^{1st} \right\rangle = 0$ because all the modes were centred on zero

$$2\left\langle x^{2nd} \right\rangle(z) = 2\sqrt{\int_{-\infty}^{+\infty} y^2 \cdot I(y)dy \Big/ \int_{-\infty}^{+\infty} I(y)dy} \,. \tag{5.6}$$

The cell values of the sample beams slit profiles were used for $I(y)$. The cell positions were used as the y value and the positional step size was employed as dy. The integration was performed by cumulative addition. It was not necessary to add the average values as was done for knife-edge integration since the extra values cancel out in the division of the two integrals (this was confirmed with calculations). The resulting numerical formula in each cell of a calculation sheet appeared as follows.

$$2\left\langle x^{2nd} \right\rangle(z) = 2\sqrt{\frac{[\text{cell y position}]^2 \cdot [\text{cell value}] \cdot [\text{stepsize}] + [\text{previous cell value}]}{[\text{cell value}] \cdot [\text{stepsize}] + [\text{previous cell value}]}} \tag{5.7}$$

5.2.1.5 The calculation of the knife-edge radii

The knife-edge radii were more difficult to calculate than the second moment radii because exact clip-levels had to be used instead of an overall integration. A simple search in the normalised knife-edge profile for a cell with the exact value of the clip-level percentage could not be made since it was highly improbable that a cell would have had this exact value. A

positional range within which to search had to be specified. *Double* the average of the qualifying cells position values was then taken as the knife-edge radius (Section 4.3.3) because the beam was centred at zero. If no cells were found that matched the criteria, an error showed up. The search range could then be adjusted until all the knife-edge radii of the 100 sample beams had no errors.

5.2.1.6 The calculation of the slit radii

The slit radii were even more difficult to determine than the knife-edge radii. This is because a normalised slit profile could possess multiple positions on the same side of the beam centre with the specified energy density clip-level value. This is illustrated in Figure 5-6, where the arrows indicate the multiple positions.

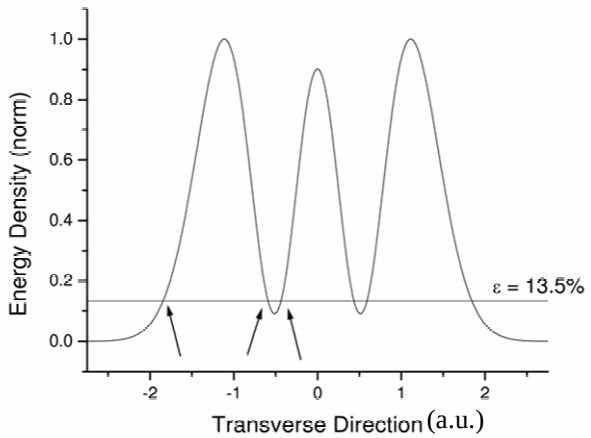

Figure 5-6: Multiple points on the same side of the centre fulfilling the energy density clip-level value condition.

Only the distance between the beam centre and the outermost value should be taken as the correct slit radius. This was achieved by firstly determining the minimum position value of all the cells whose energy density values met the clip-level range criteria. The mean of the position values of the adjacent cells that also met the criteria (including the original value) was then taken as the slit radius because the beam was centred at zero.

5.2.1.7 Generation of a large enough sample

Every time an action was performed in *Excel*, new random M -values were generated. A macro was written that copied and pasted all three radii of one hundred sample beams two hundred times to a separate sheet. This generated beam radii values for twenty thousand

sample beams. If the sample size was still too small, the macro was repeated to generate forty thousand values and so forth.

5.2.1.8 The numerical error

The calculation techniques of both the knife-edge and slit radii selected the mean of a certain number of discrete qualifying cells. These two alternative radii were therefore discrete. The second moment calculation utilised all the cell values of the one-dimensional energy density profiles and was much more accurate. The discrete alternative radii will therefore have a spread in second moment radii values. This spread is referred to as the numerical error, which is in fact a very real error in modern camera systems employing pixel-counting techniques [48].

5.2.1.9 Numerical program for rectangular symmetric beams

The Hermitian functions that characterise rectangular symmetric beams are separable in the two Cartesian directions (Section 3.2.1.2). Since the slit and knife-edge scanners are also rectangular symmetric, the practical implication is that the normalised slit intensity in one direction is equivalent to the profile obtained by setting the other directions values equal to zero which is the same as the one-dimensional pinhole profile. This was already used in the derivation of Equation (4.2) and is graphically illustrated in Appendix C. The generation of two-dimensional energy density distributions is therefore unnecessary due to the Cartesian separability of the Hermitian functions. Unlike cylindrical symmetric modes the same functions describe the energy density distributions in both principle Cartesian directions. More pure mode energy density combinations (up to mode $TEM_{xy}0\ 10$ or $TEM_{xy}10\ 0$) could therefore be included in the calculations. Beams with relatively high M^2-values could therefore be modelled. Apart from these changes, the rest of the rectangular numerical program was similar to that of the cylindrical symmetric case (Section 5.2.1).

5.2.2 Analytical Programming

The rectangular separability in the Cartesian directions of the Hermitian modes also provided the possibility of analytically solving the second moment, slit and knife-edge radii integrals. These integrals are solvable in mathematical programs such as Matlab and Mathematica. The latter was chosen due to previous experience with it.

The analytical program had the same structure as described in Figure 5-3 and can be found in Appendix G. There were only a few perceptible differences between it and the numerical programs.

- Only energy density functions up to mode $TEM_{xy}\,0\,5$ were used (Appendix A).
- Each of the functions was energy normalised, meaning the profiles they generated were normalised with the total area underneath them, which also had to be analytically calculated.
- The second moment radius was calculated analytically using Equation (5.6).
- The energy function of the sample beam was calculated by analytically integrating the energy density function according to Equation (4.5) and was then normalised to the maximum energy value.
- The knife-edge radius was found by applying a root finding function (FindRoot) to the normalised beam energy function added to the required energy clip-level.
- The slit radius was then obtained by applying the root finding function to the sum of the normalised energy density distribution and the required energy density clip-level.

Even though the root finding functions are numerical, their accuracy far exceeded that of the *Excel* program. The analytical program performed all these calculations for one sample beam at a time, which took some time to solve (especially for linear combinations containing a high number of pure mode functions). The program therefore took a very long time to run: it could typically run overnight or even over a weekend to produce enough sample results.

5.3 Application of the computed radii

The second moment, slit and knife-edge radii of the resulting beam profile or beam profile function (depending on the calculation approach) were calculated with any one of the three programs. Values obtained with one of these programs will henceforth be referred to as the computed values. The computed values were used directly as the different beam quality values according to Equations (4.22) and (4.24), because the Gaussian radii of the pure modes were chosen as one (This was also done by Johnston [27]). The relationship between the second moment and the alternative M -values could therefore be plotted and compared to existing functions of correlation theories to obtain their accuracy. The newly proposed theory plotted the proportionality factors of Equation (4.26) as a function of their respective

alternative M -values. Correlations between the different methods could be directly obtained from these graphs. These accuracies and new methods are presented in the next chapter.

5.4 Summary

Three programs, two numerical and one analytical were described which were used to test the ISO's correlations as well as to develop a new theory. The numerical programs perform numerical calculations to determine the three different beam radii for both cylindrical and rectangular symmetric beams. The analytical integration program can only be used for rectangular symmetric beams. In the next chapter, the results of these programs are presented.

Chapter 6

Computational results

In the previous chapter, three programs were presented with which to calculate beam radii from different definitions of a large number of sample beams. Two of these programs were numerical and could calculate beam radii for cylindrical and rectangular symmetric beams. The third program was analytical and could only calculate beam radii for rectangular symmetric beams. In this chapter, the numerical results of the programs will be used to evaluate the accuracy of the ISO knife-edge and slit correlation functions and to develop new correlation methods.

6.1 Relationships between second moment and knife-edge M-values

Rectangular and cylindrical beams consisting of a set number of modes were investigated respectively. Beams with the same number of modes of a particular symmetry are classified as belonging to a certain beam subclass. For instance, all beams consisting of the first three rectangular modes fall into the rectangular three-mode subclass. In Figure 6-1 (see page 76) the second moment M-values were plotted versus their respective knife-edge M-values (calculated with a 16% clip-level) for different subclasses. Graphs for rectangular beams ranging from the rectangular two-mode (top) to the five-mode (bottom) subclasses are given in the left column of Figure 6-1. Their cylindrical symmetric cousins are given in the right column.

All the graphs were drawn on the same scale so that direct comparisons between them could easily be made. Unfortunately, it meant sacrificing some detail for the lower mode subclass graphs. Their structure will, however, be investigated in more detail in later sections.

6.1.1 General observations

The relationship between the second moment and knife-edge M definitions of the rectangular subclasses shows a linear trend, which gradually deteriorates as the number of modes is increased. The ISO knife-edge correlation function (Section 4.5.3) was superimposed as a linear reference function to highlight this deviation. Any deviations from the ISO functions will be thoroughly investigated in Section 6.3.1. The pure cylindrical symmetric modes generally have lower second moment and knife-edge M-values than their rectangular cousins. Cylindrical symmetric resonators therefore produce higher quality beams. However, it is very difficult to obtain perfect cylindrical symmetry within a resonator and is usually only found in high quality sealed off CW systems.

The proportionality graphs of all the lower beam subclasses are part of those of all the higher subclasses. This is because the lower subclasses represent the linear combinations in which the higher modes have an almost zero weight. A theory that accurately describes a beam subclass containing N modes therefore also describes all the other lower N subclasses.

6.1.2 Separate evaluation of subclasses

The top two graphs (Figure 6-1 A and E, page 76) show that, for all practical purposes, there is a one-to-one relationship between the two M-value definitions for both two-mode subclasses. This implies that if it is established that a laser beam contains only the first two modes (as most high quality commercial systems do), its second moment M-value can be determined exactly by means of knife-edge characterisation. It can be observed from the inserts that the overall relationship between the second moment M-values and the knife-edge M-values is linear with a slight curling deviation. The discrete structure of the numerical results will be discussed in future sections (Section 6.3.1 and Section 6.4.2.1).

It was observed that both three-mode subclasses can have more than one second moment M-value for a measured knife-edge M-value or vice versa. This is especially pronounced for the rectangular symmetric case (Figure 6-1 B), which consists of two lobes. There will therefore always be a theoretical error when converting a knife-edge M-value to a second moment M-value by means of any correlation function for subclasses consisting of more than two modes.

The second moment radius can be thought of as a wave function specific property since it is strongly dependent on the beam energy density profile. A general Hermitian energy density profile is equivalent to mixtures of the probability curves of the quantum harmonic oscillator. The knife-edge radius, on the other hand, is associated with the energy flux of beams. The multiple second moment radii are therefore reminiscent of quantum degeneracy, where different states (having different wave functions) have the same eigen energy values under certain conditions. This theoretical error when using correlation functions will therefore be referred to as the degenerate error. A knife-edge M -value does in fact exist for both three-mode subclasses where the degenerate error is zero. This point can clearly be seen near the centre of the rectangular computed values (the connection point between the two lobes in Figure 6-1 B) at a knife-edge M -value of 1.732. This implies that the second moment M -value is known to be exactly 1.591 if a knife-edge M -value of 1.732 was measured with 16% clip-level for this subclass. The zero error point is not as visible for the cylindrical symmetrical case due the numerical error described in Section 5.2.1.8, and because its degenerate errors are smaller. It will be shown in a later section how this interesting feature is central to a new correlation method.

The rectangular four-mode subclass (Figure 6-1 C) has no zero degenerate error points like the rectangular three-mode subclass. The degenerate error is also substantially larger so that large correlation errors can be expected when any correlation function is used. The cylindrical four-mode subclass (Figure 6-1 G) does not show the same behaviour. The degenerate error of this subclass increased only marginally at lower knife-edge M -values from the previous subclass and the range of the knife-edge M -values increased only slightly to terminate at the value of the pure TEM_{pl} 10 mode. The 1.732 zero error point is still present in the graph of the cylindrical four-mode subclass and is in fact more perceptible due to increased degenerate errors elsewhere in the graph.

The rectangular five-mode subclass (Figure 6-1 D) can be seen to have very large degenerate errors. The general relation between the M -values from the two definitions no longer follows the linear trend of the previous subclasses. It does therefore not appear wise to expect too accurate correlations for rectangular beam subclasses containing such a large number of higher order modes.

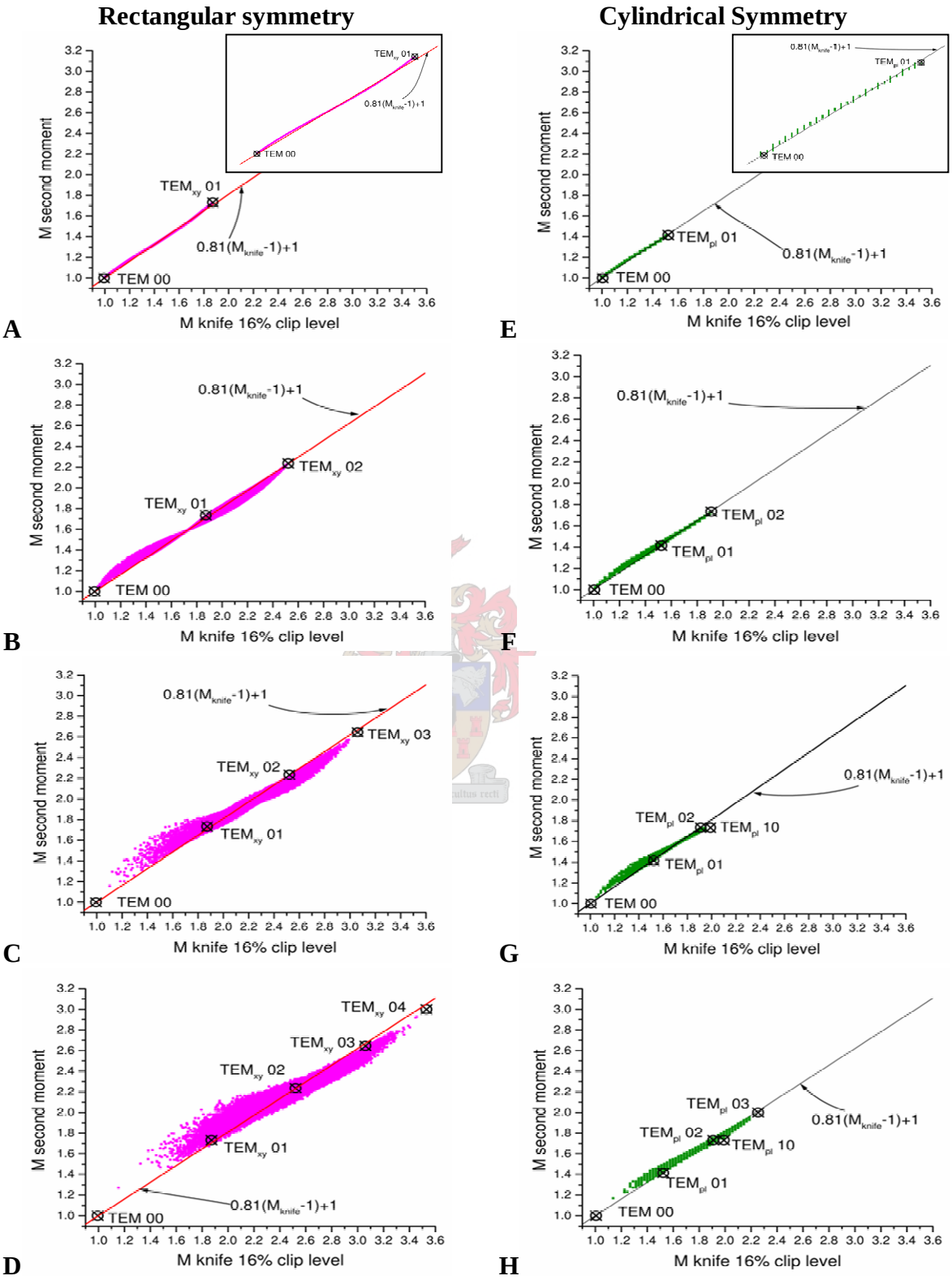

Figure 6-1: Second moment M -values as a function of their respective knife-edge M -values for the first four rectangular (left) and cylindrical (right) subclasses.

It is still acceptable to use a correlation function for the cylindrical five-mode subclass (Figure 6-1 H) even though its proportionality graph does deviate slightly from the linear trend set by the previous beam subclasses and contains no zero error knife-edge proportionality points. The degenerate error also increased only slightly when the fifth mode was added.

For high mode content beams it was found that the computed second moment and knife-edge M -values do not reach those of the pure modes, especially the modes having lowest and highest mode numbers. This is because there is a very small chance of finding a beam consisting of only a single pure mode in a resonator where many other pure modes have an equal probability to lase.

It was apparent that the knife-edge and second moment M -values differ greatly for the two symmetries. In practise, it is not always clear whether a laser has rectangular or cylindrical symmetry, especially when it only contains a few modes. It would therefore be very useful to find a single theory that can describe subclasses from both theories with low mode content.

6.2 Relationships between second moment and slit M-values

6.2.1 General observations

In Figure 6-2 (see page 78) the second moment M -values are plotted versus their respective slit M -values (calculated with a 13.5% clip-level) for different subclasses. It is immediately apparent that there is no general linear relationship between the second moment and slit M -values for the rectangular subclasses. The second moment values deviate sharply from the linear ISO slit correlation function, which was used as a reference. Only at low slit M -values does there seem to be linear behaviour. The second moment values of the cylindrical subclasses behave much more linearly and correspond very well to the ISO reference function.

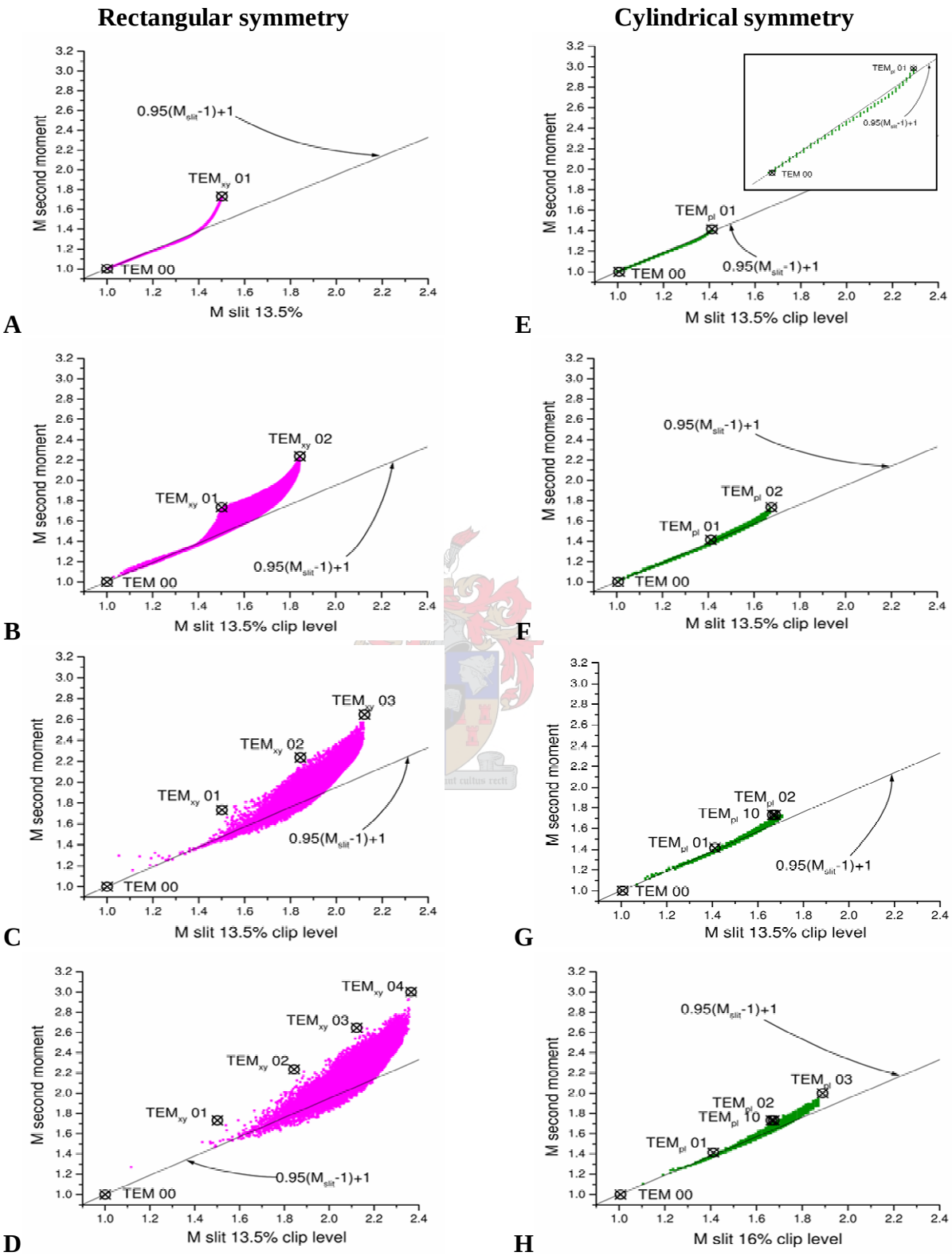

Figure 6-2: Second moment M -values as a function of their respective slit M-values for the first four rectangular (left) and cylindrical (right) subclasses.

6.2.2 Separate evaluation of subclasses

The layout of Figure 6-2 (page 78) is identical to that of Figure 6-1 (page 76), described in Section 6.1.2. A one-to-one relationship is found between the second moment and slit M -values of the two, two-mode subclasses (Figure 6-2 A). This one-to-one relationship is similar to the knife-edge case. After an initial linear relationship, the second moment M -values of the rectangular two-mode subclass curve sharply away to higher values ending at the value of the pure $TEM_{xy}02$ mode. A linear correlation function would therefore be expected to give large errors for the rectangular two-mode subclass. The proportionality graph of the cylindrical two-mode subclass does not exhibit such a trend. It remains almost linear and corresponds well with the ISO reference function.

Both three-mode subclasses do not have a one-to-one relationship between the second moment and slit M -values (similarly to the knife-edge case). This is, however, much more apparent for the rectangular subclass (Figure 6-2 B) which resembles a slipper. There is a nonlinear relationship between the second moment and slit M -values for the rectangular three-mode subclass for slit M -values higher than approximately 1.4 where any correlation function will have large degenerate errors. No slit zero error point was found for the rectangular three-mode subclass as was the case for the knife-edge method. The cylindrical three-mode subclass remains largely linear and corresponds well with the ISO reference function, exhibiting only minimal degenerate errors (Figure 6-2 F). As the number of modes is increased, the general shape of the rectangular subclasses resembles upturned umbrellas with the pure mode values at the spoke ends (Figure 6-2 C, D). The degenerate errors become so severe that it was doubtful whether any general correlation could be found for rectangular beams. The cylindrical symmetric graphs remained almost linear with only minimal degenerate errors (Figure 6-2 G, H).

6.3 Determining the accuracy of the ISO correlation functions

The correlation functions for the knife-edge and slit alternative methods were already evaluated by superimposing them on the second moment graphs of Figure 6-1 and Figure 6-2. Error graphs are, however, more useful to get a quantitative measure of how well the ISO's functions correlate with the alternative (knife-edge or slit) and second moment M -values.

Such error graphs were obtained by subtracting the calculated second moment values from those obtained from the ISO function and dividing again by the computed values to obtain an error percentage. The layout of the error graphs for the knife-edge (Figure 6-3 page 81) and slit (Figure 6-4 page 83) is identical to that of Figure 6-1 (page 76) and Figure 6-2 (page 78).

6.3.1 The ISO knife-edge correlation function

From Figure 6-3 A it can easily be observed how the second moment M-values of the rectangular two-mode subclass curl around the ISO correlation function. The error varies almost sinusoidally between the maximum approximate values of -1.5 and +0.5%, which is close to a typical measuring error. The average of the computed values of the proportionality graph for the cylindrical two-mode subclass is identical to the rectangular case up to a knife-edge M-value of 1.53 (see the insert in Figure 6-3 E). The slight offset was probably due to a numerical calculation error. The numerical error described in Section 5.2.1.8 could be assessed because there is a one-to-one proportionality for this beam subclass as seen from analytical calculations. The analytical calculations also give exact values for all practical purposes. The maximum numerical error was subsequently found to be approximately $\pm 0.94\%$ from the average values. Notice that the correlated second moment M-value for the pure TEM_{00} beam does not have a zero error because the ISO used a rounded off clip-level of 16%. A clip-level of 15.866% leads to a knife-edge radius, which corresponds much better to the $1/e^2$ Gaussian radius.

Errors arising from using the ISO correlation function on beams belonging to the rectangular three-mode subclass are substantial. From Figure 6-3 B it could be observed that negative errors of up to 9% and positive errors up to 4.6% can unknowingly be made when one blindly uses the ISO Annex. This is unacceptable when considering that these errors are roughly double for M^2 values. The total error might be even larger if measuring errors are also taken into account. It must, however, be mentioned that it is unlikely that such beams would occur in practise. This is due to the low density of points close to the maximum negative error indicating a general low probability to find such beams in practice.

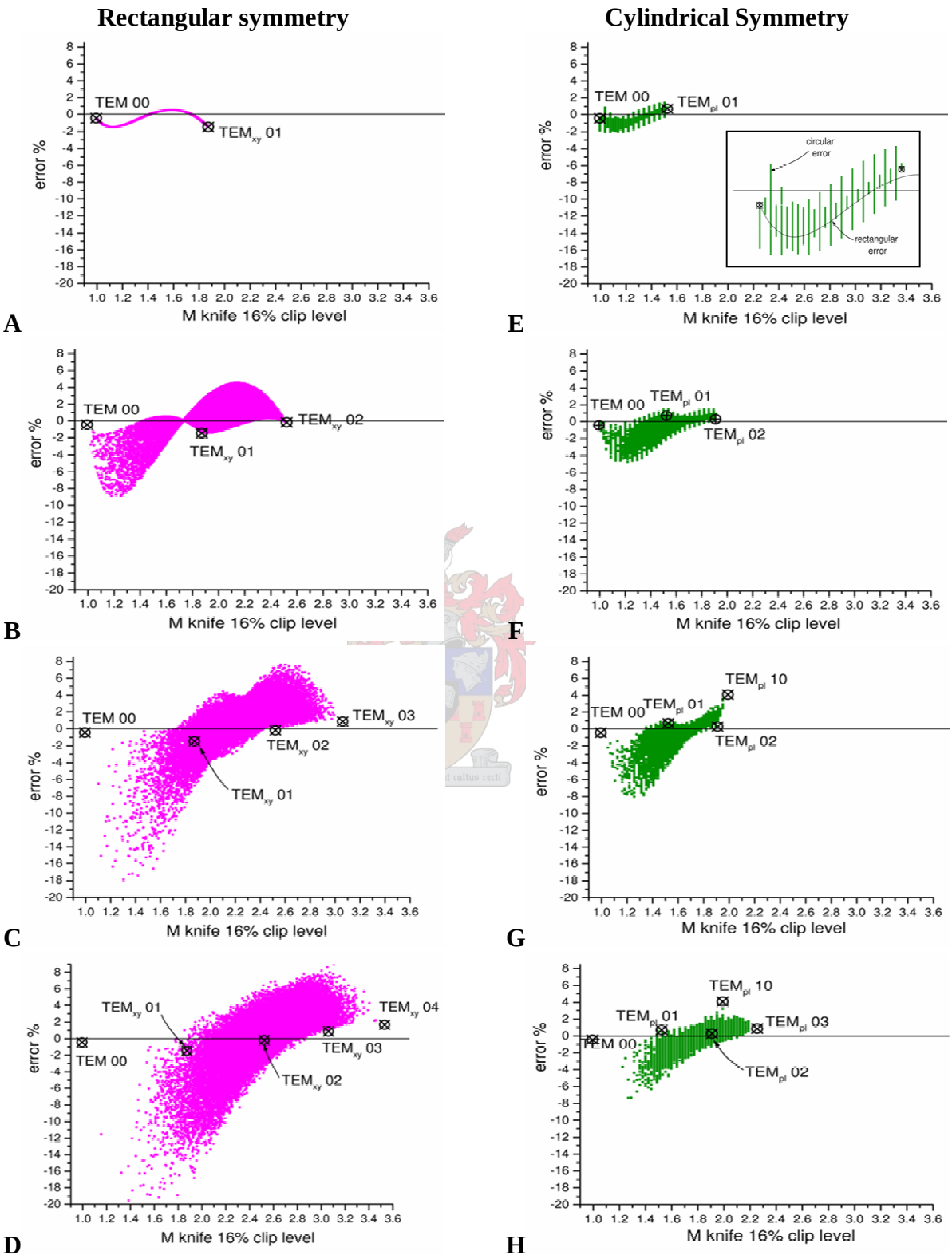

Figure 6-3: Potential errors that can be made when using the ISO knife-edge correlation function (Equation (4.12)) for the first four rectangular (left) and cylindrical (right) subclasses.

For the cylindrical three-mode subclass the maximum error of 4.6% is roughly half that of their rectangular cousins. It is therefore clear why the ISO chose to only correlate cylindrical symmetric beams. Figure 6-3 C shows that up to -18% and +8% maximum errors are possible for the rectangular four-mode subclass. It is, however, very unlikely that such high negative errors will ever be made since it is statistically unlikely to find beams with low knife-edge M -values close to one for the rectangular four-mode subclass. More realistic errors of $\pm 8\%$ can therefore be expected. It became clear from the error graphs of beam subclasses consisting of more than three modes that the ISO correlation is only suited for cylindrical symmetric beams. The error for rectangular symmetric beams is unacceptably high, while it remains constant or even decreases for cylindrical symmetric beams as the number of modes is increased.

6.3.2 The ISO slit correlation function

The second moment values for the rectangular two-mode subclass (Figure 6-4 A page 83) do not correspond to those from the ISO function. This can lead to large errors of up to almost 15% for higher slit M -values. It can be seen from the insert in Figure 6-4 E that the average of the numerical values for the cylindrical two-mode subclass are identical to those of their rectangular cousins up to slit M -values of 1.42. The large errors are only made at higher slit M -values and are therefore avoided for cylindrical symmetric beams.

From Figure 6-4 B it can be observed that the ISO slit correlation errors are very large for the rectangular three-mode subclass. The rectangular slit M -values also have no zero error point like their knife-edge counterparts. A minimum error point can, however, be observed at a slit M -value of approximately 1.4. A band of higher density points is also observable. This implies that beams in this subclass are more probable to have second moment values in this band. The ISO correlation function does not follow this high-density band. It is found that the degenerate error becomes even more severe for subclasses consisting of more modes. As the number of rectangular modes is increased, the high-density band vanishes and the maximum errors remain consistently high at values of around 22%.

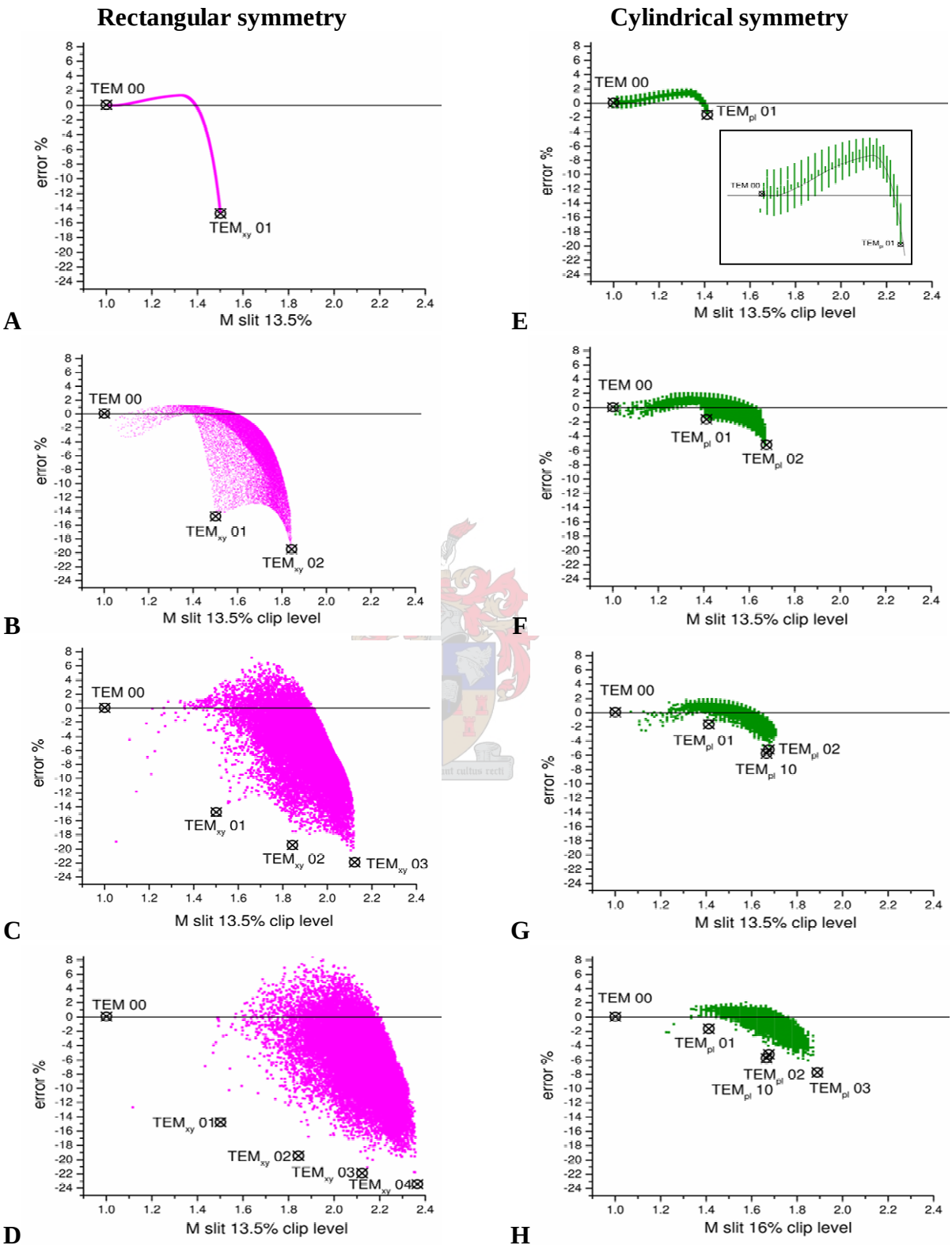

Figure 6-4: Potential errors that can be made when using the ISO slit correlation function (Equation (4.12)) for the first four rectangular (left) and cylindrical (right) subclasses.

It can be observed from Figure 6-4 F that the ISO errors for the cylindrical three-mode subclass are far less severe and actually seem to intersect the average of the computed values. This trend is also observed for the cylindrical four-mode subclass (Figure 6-4 G). Significant negative errors at higher M -values become apparent in the cylindrical four-mode subclass, which seem to be even worse for the five-mode subclass (Figure 6-4 H). A further unusual finding is that the ISO correlation function does not follow the general trend of the pure cylindrical second moment values.

6.4 Novel comprehensive correlations

It was shown in the previous sections that the ISO functions have large unacceptable errors. The aim of this section is to minimise these errors by developing novel correlation functions and methods. The newly proposed graphs that are used to correlate between the second moment and alternative definitions consist of the computed proportionality factors (defined in Section 4.5.4 Equation (4.26)) plotted as a function of their respective alternative M -values. This means that the proportionality factors are the second moment values divided by their respective alternative M -values of Figure 6-1 (page 76) and Figure 6-2 (page 78). The resulting proportionality graphs are fitted with appropriate functions by means of a least squares method. Proportionality factors are used since it was found that the small variations in the relation between the second moment and alternative values could better be incorporated into the fitting functions. The graphs also illustrate that proportionality factors do not remain constant as Johnston [27] proposed. The measured alternative M -values should be inserted into the fitted functions to obtain the correlation factor. The resulting correlation factor needs to be multiplied again by this measured alternative M -value to obtain the second moment M -value. This is already done for all the fitted functions for the convenience of a potential user. The second moment values can therefore be directly obtained by inserting the alternative M -values into these multiplied functions. If the original fitting functions are required, they can be obtained by simply dividing by the alternative M -value.

6.4.1 Knife-edge correlation for rectangular Gaussian beams

The knife-edge proportionality graphs of the first four rectangular subclasses can be seen in Figure 6-5 A-D (the left column on page 86). They were obtained by simply dividing the second moment M -values of Figure 6-1 A-D (page 76) by their respective knife-edge M -

values. The solid curves are the best least squares fits of a fifth order polynomial that was forced through the knife-edge M -value and proportionality factor of the TEM_{00} mode. The forcing ensured that the functions always produce a second moment M -value of 1 for the fundamental mode. The high order of the polynomial produces sufficient local extrema in the function so that it is able to accurately follow the computed proportionality values. Even though this produced long correlation functions, the extra accuracy justifies the extra calculation time, which is anyway short compared to the time it takes to measure the entire beam propagation. The polynomial functions are given in Table 6-1 (see page 87) for the first four rectangular beam subclasses. The error made using one of the correlation functions can be determined by subtracting the computed values from the function and dividing again by the computed values to obtain an error percentage as was done for the ISO correlation functions in Sections 6.1 and 6.2. The graphs of these error values can be seen in Figure 6-5 E-H (the left column) for their corresponding proportionality graphs (in the right column).

The rectangular two-mode subclass correlation function followed the computed values almost exactly. The error, seen in the insert in Figure 6-5 E, varied between -0.025% and +0.025% which is far below any possible measuring error. The proportionality graph for the rectangular three-mode subclass can be seen in Figure 6-5 B. The two lobes and zero error point are much more apparent than they were in the direct second moment graphs of Figure 6-1 B (page 76). This was one of the reasons why the proportionality factors graphs were used instead of the direct second moment graphs. The fitted polynomial passes through the lobe connecting zero error point and then almost through the value of the pure $TEM_{xy}02$ mode. The left lobe was found to have the largest errors varying between -5.5% and +3.2%. The right lobe's maximum errors only vary between +2.7% and -2.9%. From the low density of points at low knife-edge M -values it can be deduced that it is improbable for beams in the rectangular three-mode subclass to have knife-edge M -values close to one. Realistically the error for the left lobe can therefore be much lower. The error made by using this function is roughly half that of the ISO's linear function. The rectangular two-mode subclass delineates the lower proportionality values of the first lobe of the proportionality graph of the rectangular three-mode subclass. The maximum error that is made using the three-mode function for beams belonging to the rectangular two-mode subclass was found to 3.2%.

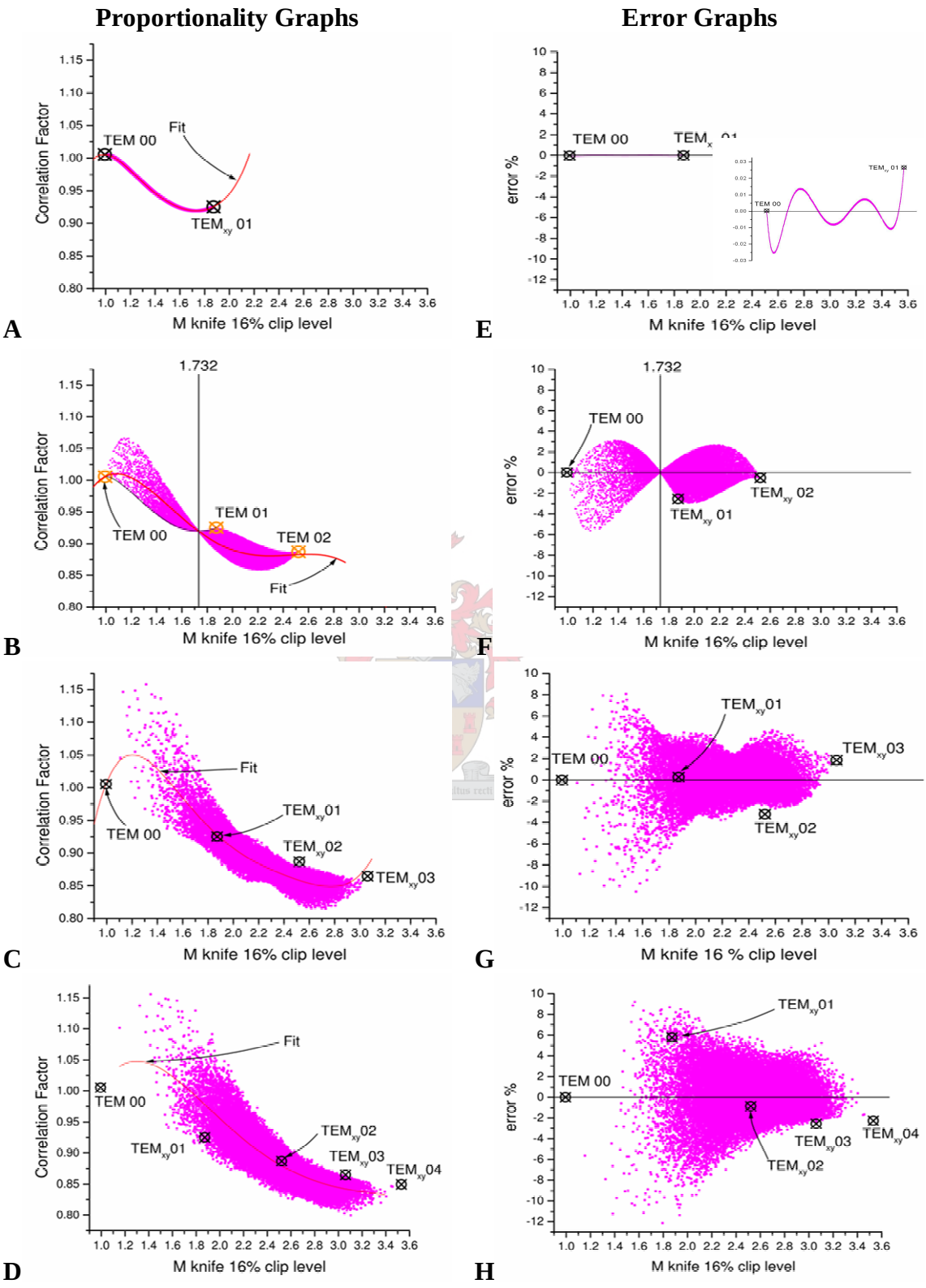

Figure 6-5:Novel comprehensive knife-edge proportionality graphs for the first four rectangular subclasses (left) and the errors that can be made when the fitted polynomials are used (right).

The error of the newly proposed correlation function of the rectangular four-mode subclass is initially very high for low knife-edge M -values (Figure 6-5 G). For higher knife-edge M -values the positive and negative errors are shifted so that no zero or minimum error points are formed. The positive errors vary between 4.7% and 2.7% and the negative errors between -5% and -2.3%. These values are quite high but are still much lower than those of the ISO function (Figure 6-3 C). The maximum correlation error of the rectangular five-mode subclass is initially very high at approximately $\pm 9\%$ but then gradually reduces to approximately $\pm 3\%$.

$$M_{knife} \times (+1.00557 - \mathrm{a}(M_{knife} - 0.994458) + \mathrm{b}(M_{knife} - 0.994458)^2 + \mathrm{c}(M_{knife} - 0.994458)^3 + \mathrm{d}(M_{knife} - 0.994458)^4 + \mathrm{e}(M_{knife} - 0.994458)^5) \quad (6.1)$$

Beam subclass	**a**	**b**	**c**	**d**	**e**	**Range** Knife-edge M	**equation**
TEM_{xy} 00+01	-0.01312	-0.7997	+1.6389	-1.357	+0.4695	M>0.9946 M<1.8724	(6.2)
TEM_{xy} 00+01+ 02	+0.1004	-0.6456	+0.6230	0.2143	+0.0212	M>0.9946 M<2.5211	(6.3)
TEM_{xy} 00+01+ 02+03	+0.4849	-1.6091	1.6448	0.7467	+0.1286	M>0.9946 M<3.0600	(6.4)
TEM_{xy} 00+01+ 02+03+04	+0.3074	-0.6721	+0.4129	0.1074	+0.0102	M>0.9946 M<3.5310	(6.5)

Table 6-1:Newly proposed correlation functions for the first four rectangular mode subclasses (the correlation factors in the table is to be inserted into Equation (6.1)).

The major drawback of using different functions for different subclasses is that knowledge of the mode content is required to use the best correlation function. The degenerate error also becomes unacceptably high for beam subclasses containing more than three modes. Most laser resonators are designed to emit beams consisting only of a low number of modes. A correlation method that has low errors and is mode independent for low mode content beams would therefore be more than sufficient for most applications.

6.4.2 Knife-edge correlation for cylindrical Gaussian beams

6.4.2.1 Separate fitting of subclasses

The same method that was used for the rectangular subclasses can now be applied to establish correlation functions for the first four cylindrical subclasses. The proportionality graphs can be seen in Figure 6-6 A-D (the left column). The solid curve overlaying the computed values is the fifth order polynomial that is forced through the fundamental mode values. These fitted polynomial functions multiplied by the knife-edge M -value can be found in Appendix D. The error graphs were calculated in a fashion that is identical to that used for the rectangular correlation functions. They can be seen in Figure 6-6 E-H (the right column).

It was established in Section 6.1.2 that the rectangular two-mode subclass had zero degenerate errors. This was done by using analytical calculations. The maximum numerical error was confirmed to be $\pm 0.94\%$ from the comparison between the two, two-mode subclasses. The numerical error can also be directly observed in Figure 6-6 E.

It can be observed that both the three and four cylindrical mode subclasses have ranges in which the error is equal to or less than the numerical error. The cylindrical three-mode subclass has errors below $\pm 0.88\%$ (which are below the numerical error) for knife-edge M -values above 1.65. The cylindrical four-mode subclass has an error of 0.87% at the knife-edge M -value of 1.732 (which is also below the numerical error). No error ranges or points could be found for the cylindrical five-mode subclass where the error was below the numerical error. It is therefore a reasonable assumption that only the two, three and four cylindrical mode subclasses have zero degenerate error points or regions.

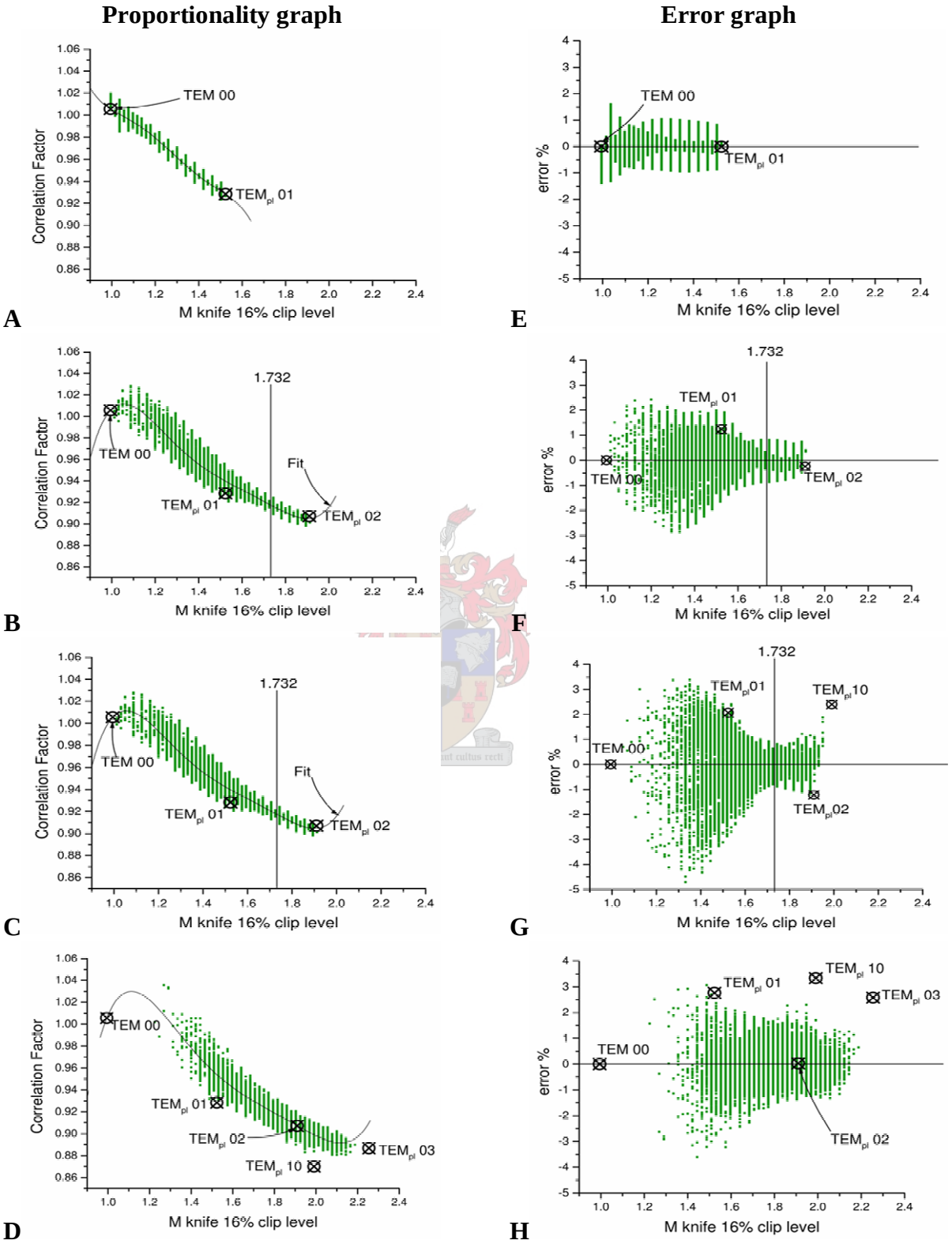

Figure 6-6: Newly proposed knife-edge proportionality graphs for the first four rectangular subclasses (left) and the errors that can be made when the fitted polynomials are used (right).

6.4.2.2 Single cylindrical correlation function

It was seen in Figure 6-1 (page 76) that the relationship between the second moment and knife-edge M -values is more linear for cylindrical symmetric beams than it is for their rectangular cousins. The degenerate error was also found to be far less severe when correlating cylindrical symmetric beams. It was therefore investigated whether a single simple function could be found for cylindrical symmetric beams. All the proportionality graphs for the first six cylindrical mode subclasses were therefore combined and fitted with a simple linear function forced through the values of the fundamental TEM_{00} mode (Figure 6-7). The linear correlation function was used for simplicity. This linear function multiplied by the knife-edge M -value was found to be

$$M_{\text{second}} = \text{M}_{\text{knife}} \times (\text{-0.1153}(\text{M}_{\text{knife}} \text{-0.994458}) \text{+1.00557}) . \qquad (6.6)$$

The error was calculated in an identical manner as was done for the correlation functions in the previous sections. This can be seen in Figure 6-7 B. Even though the error was found to be quite high (up to almost –7%) for low knife-edge M -values it can be deduced from the low density of points that most practical beams will probably have much lower errors in this range. A more realistic total error assessment would be approximately +1.5 and -2.5%, which is much lower than the ISO correlation function, which has realistic errors as high as -5% (Figure 6-3 G page 81). This single linear function is more practical than the previous functions in Section 6.4.2.1 since for a minimal increase in error the function is more simple and is also independent of number of modes in a beam (up to the $TEM_{pl}11$. This could not be attempted for rectangular subclasses due to the increased degenerate error and non-linear behaviour that accompanies an increase in mode content.

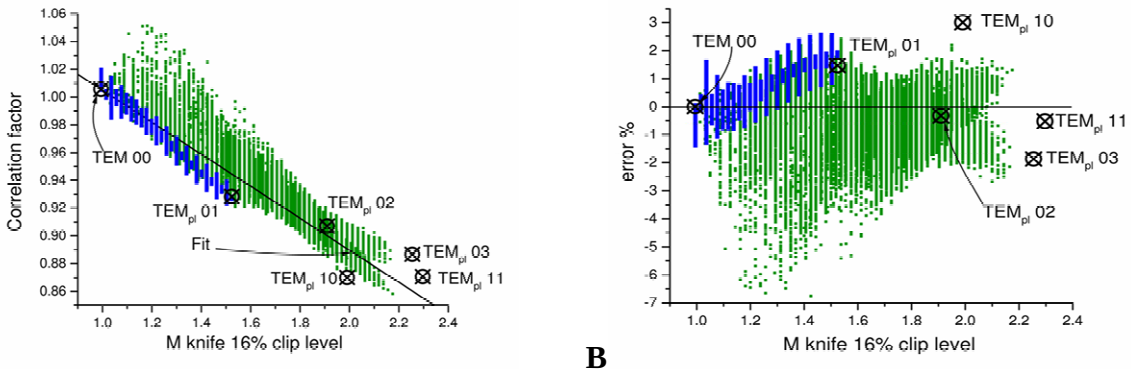

A **B**

Figure 6-7: Newly proposed single knife-edge correlation for the first five cylindrical subclasses (left) and the errors that can be made when the function is used (right).

6.4.3 Comparison between the rectangular and cylindrical proportionality graphs

6.4.3.1 The 1.732 zero error value

The rectangular three-mode and cylindrical four-mode proportionality graphs are superimposed in Figure 6-8. The combined proportionality graphs for the two symmetries correspond exactly for knife-edge M -values lower than 1.732, taking into account the numerical error. The cylindrical proportionality factors deviate from that of their rectangular cousins for higher knife-edge M -values. After the value for the TEM_{pl} 02 mode is reached, the cylindrical proportionality factors drop off sharply to the value of the pure TEM_{pl} 10 mode. The rectangular proportionality factors continue to form a right lobe, which terminates at the value of the pure TEM_{xy} 02 mode. The knife-edge M -value of 1.732 is therefore very important for both symmetries in that the cylindrical four-mode subclass (which contains the values of previous subclasses) can be described by the rectangular three-mode subclass at knife-edge M -values lower than 1.732 (with a 16% clip-level). One-to-one proportionalities for the rectangular three-mode and cylindrical three and four-mode subclasses were also previously found at this knife-edge M -value (Section 6.4.2.1).

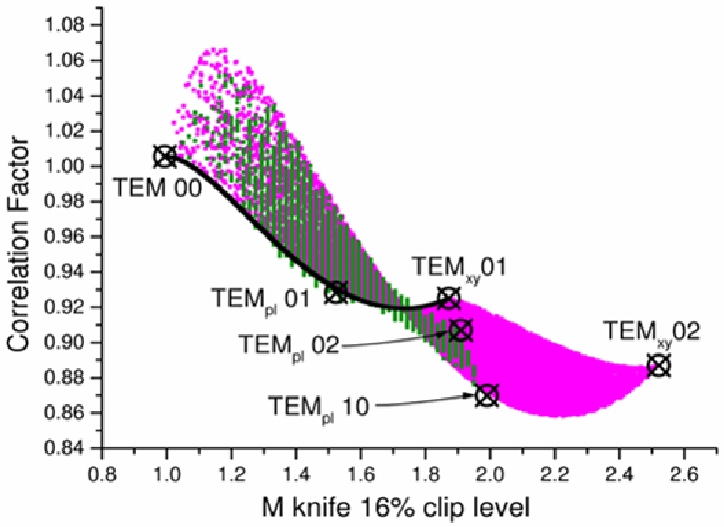

Figure 6-8: Comparison of the knife-edge proportionality graphs of the rectangular three-mode (magenta) and cylindrical four-mode (green) subclasses.

6.4.3.2 Additional applications of the proportionality graphs

The rectangular three-mode proportionality graph can be used not only for correlation purposes, but also to evaluate laser beams when both the second moment and knife-edge radii are easily accessible. Note from the previous section that three-mode proportionality graph also describes the cylindrical two, three and four-mode subclasses. It can be assessed how close to the fundamental a beam is by plotting the proportionality factor of a measured beam (Equation (4.26)) versus its knife-edge M -value (Equation (4.24)) on the proportionality graph of the rectangular three mode subclass.

The proportionality factors and graphs can also potentially be utilised in camera software to accurately align and to select only the TEM_{00} mode in laser resonators. This can also be done by monitoring the transverse mode beating [45], [21], but this method is not suited to pick up diffractive effects from an aperture that is too small. The new camera technique would monitor whether the knife-edge proportionality factors determined by only one two-dimensional energy density profile correspond to the computed proportionality factors of the rectangular two-mode subclass at knife-edge M -values close to one. The resonator could then be adjusted until the proportionality factors in both transverse directions are equally shifted to their maximum M -values (see Figure 6-5 A). If these values correspond to the values of the knife-edge two-mode proportionality graph the best possible near TEM_{00} beam profile for the particular resonator is obtained. The knife-edge and second moment M -values of such beams should also be accessible from this proportionality factor without the measurement of the entire beam propagation due to the one-to-one nature of the proportionality graph of the rectangular two-mode subclass.

The proportionality graph can be used to determine whether the resonator contains two or three modes. Any deviation from the rectangular two-mode subclass line would indicate a third mode. The proportionality graph can also be employed to determine whether a beam from a simple resonator shows general Gaussian behaviour and measuring errors. If a measured proportionality factor does not correspond to expected values on a proportionality graph, the beam is either non-Gaussian or serious measuring errors are made. The user must determine which one is applicable. Small deviations from Gaussian behaviour can be more

easily picked up in the proportionality graphs than in the second moment graphs. The proportionality graphs therefore serve as a new tool for the evaluation of laser beams.

6.4.3.3 A symmetry unified correlation method

In the earlier sections, a large number of functions were presented with which to correlate the knife-edge and second moment M -values. These functions depend on the symmetry of a resonator and the number of modes it contains. Figure 6-8 does suggest that there are some similarities between the rectangular and cylindrical symmetric correlations factor graphs for beam subclasses containing up to certain number of modes.

A point was also found where there is a one-to-one proportionality for the first two and three rectangular and cylindrical subclasses respectively. Beams consisting only of the first few modes are the most desired and therefore commonly found in practical systems. A unified method that accurately describes such beams of both symmetries should be highly relevant and sought after. In the following section the effect of changing the clip-level will be investigated as well as the implications it has for such a unified method that correlates the first few mode subclasses in both symmetries.

6.4.4 The effect of the knife-edge clip-level on the proportionality graphs

6.4.4.1 Rectangular symmetry

Figure 6-9 shows a few knife-edge proportionality graphs for the rectangular three-mode subclass calculated with various energy clip-levels. The 16% clip-level graph of Figure 6-5 B (page 86) is indicated as a reference graph. It was observed that all the different clip-levels retain the zero error point that was seen in the 16% clip-level proportionality graphs in Section 6.4.1. The two lobes play an important part now. The number of proportionality factor points in the left lobes increases with clip-level and vice versa for the right lobe. The zero error point, however, remains stationary at the 16% value of 1.732, which is likely to be the square root of three ($\sqrt{3}$).

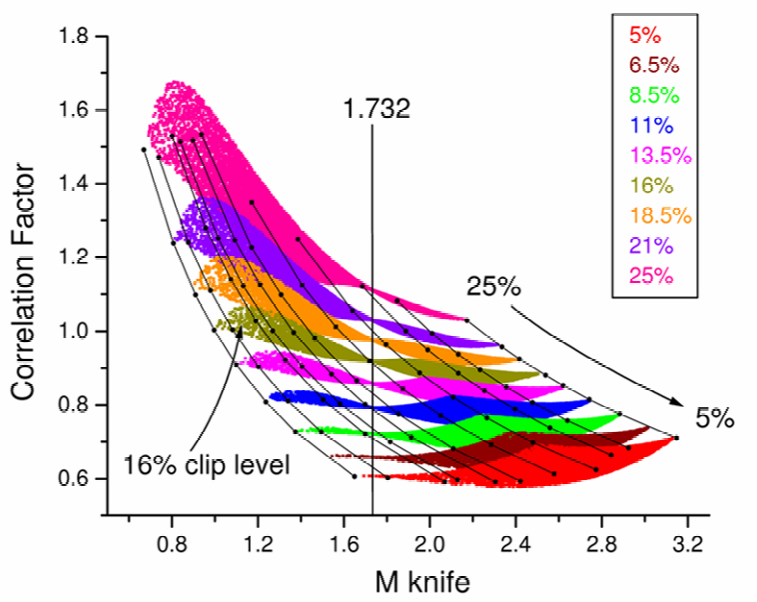

Figure 6-9: Knife-edge proportionality factor graphs for the rectangular three-mode subclass calculated using different clip-levels.

The black lines trace specific mode combinations as the clip-levels are changed. It can be seen that the proportionality factors of individual sample beams shift in arcs from lower to higher knife-edge M -values as the clip-level is lowered. All the proportionality factor values shift from the left lobe at higher clip-levels to the right lobe at lower clip-levels crossing the 1.732 zero error line. The two extreme mode traces are for the TEM_{00} mode at the bottom which crosses only at a clip-level of $4.16\,\%$ and the TEM_{xy} 02 mode at the top which only crosses at a clip-level of $35.00\,\%$. All of the mode combinations therefore cross the zero error line at some clip-level between these two extremes. This can be seen more clearly in the more complete 34.6% to 4.5% rectangular combination proportionality graph shown in Appendix E Figure 10-6. It is therefore possible to obtain a zero error proportionality factor for any linear combination of the first three rectangular modes by simply changing the clip-level.

It has not been determined why the zero error point has the apparent knife-edge M -value of the $\sqrt{3}$. This may become the subject of a future more mathematical study of this particular problem. It is only necessary at this stage to validate the value graphically since the analytical accuracy is far above any measuring error. This graphical proof is shown in Figure 6-10, which focuses in on the 1.732 line and consists of more proportionality graphs than Figure **6-9**.

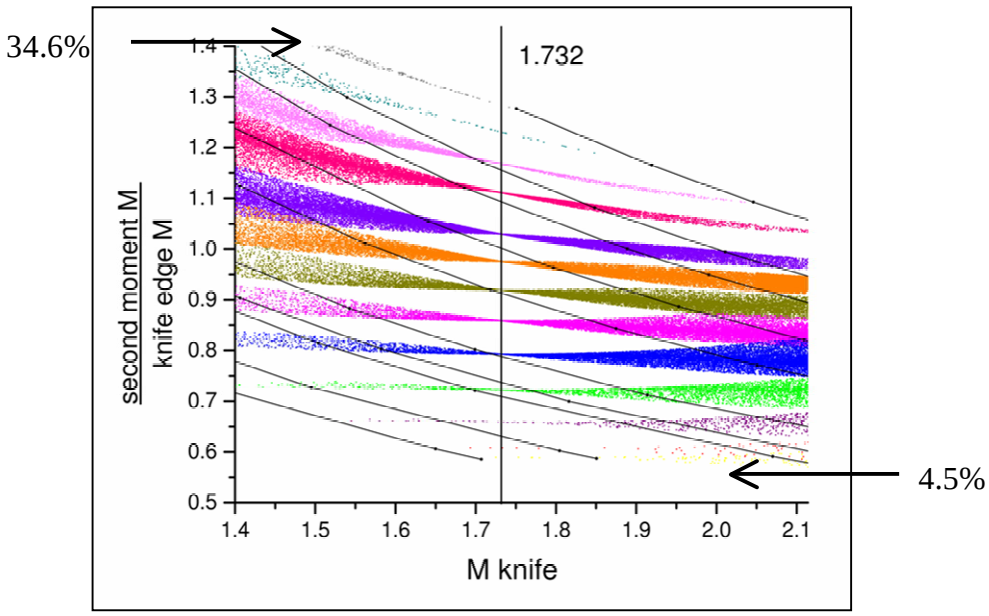

Figure 6-10:Expanded view of Figure 6-9 around the knife-edge M -value of 1.732.

6.4.4.2 Cylindrical Symmetry

Figure 6-11 and Figure 6-12 (see page 96) show the effect of clip-level changes on the knife-edge proportionality graphs for the three and four cylindrical mode subclasses respectively. The enlarged version of these graphs are given in Appendix E. It was observed that the cylindrical symmetric graphs show the same behaviour as the rectangular ones. The zero error point, which is hidden by the numerical error, remains stationary for both subclasses. The number of proportionality factor points in the left lobes increases with clip-level and vice versa for the right lobes. The total error, however, remains consistently below the numerical error at knife-edge M -values of 1.732. The proportionality graph of the cylindrical three-mode subclass does not have large degenerate errors for most of the clip-levels. The degenerate errors for the whole range of knife-edge M -values are seen to be lowest for an 11% clip-level.

The proportionality graphs of the cylindrical four-mode subclass are less defined because a very large number of calculations have to be done to obtain all possible linear superpositions. Due to the larger degenerate error in the left lobe, the stationary nature of the zero error point at 1.732 was much more apparent than for the cylindrical three-mode subclass.

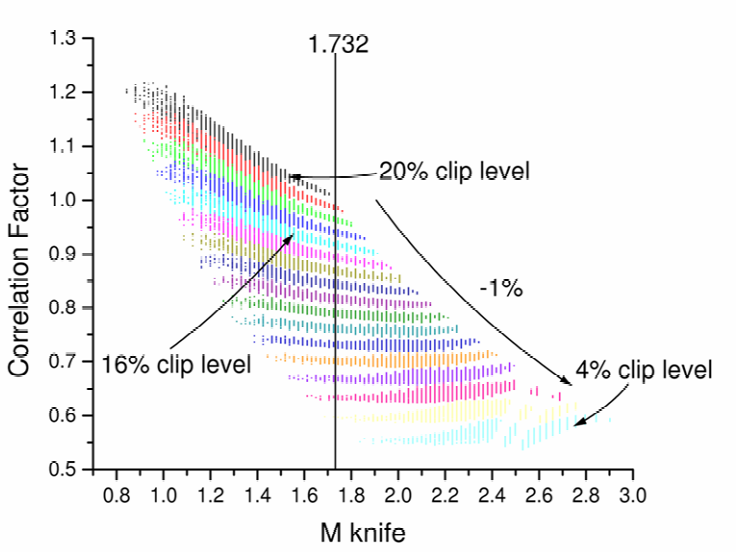

Figure 6-11:Knife-edge proportionality factor graphs for the cylindrical four-mode subclass using different clip-levels.

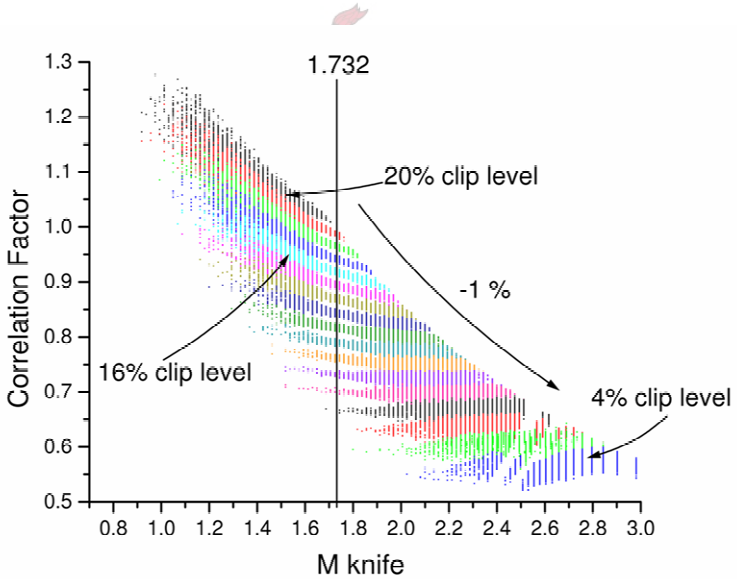

Figure 6-12:Knife-edge proportionality factor graphs for the cylindrical four-mode subclass using different clip-levels.

The major difference between the clip-level dependence of the cylindrical and rectangular graphs is that the cylindrical TEM_{pl} 02 and TEM_{pl} 10 modes cross 1.732 knife-edge M -value at the much lower clip-level of roughly 20%. This is because cylindrical symmetric resonators have a smaller range of possible knife-edge M -values for subclasses with the same number of modes as their rectangular cousins.

6.4.4.3 Zero error correlation $\rightarrow$ the clip-level optimisation method

The single proportionality factors at knife-edge M -values of 1.732 for the above mentioned subclasses are now defined as the zero error proportionality factors for specific clip-levels. The zero error proportionality values are plotted versus clip-level in Figure 6-13 for the examined cylindrical and rectangular symmetric subclasses overlaying each other. It is remarkable that they seem to correspond exactly when one takes into account the large numerical error and large difference in the slit intensity profiles of the numerical method. The rectangular analytical proportionality factors were calculated much more accurately and they were therefore fitted with a second order polynomial function

$$C_{0\,\text{error}} = 0.45106 + 0.03378\ C_l - 2.86149\times10^{-4}\ \ C_l^{\,2}. \tag{6.7}$$

C_l is the zero error clip-level where the knife-edge M -values are 1.732. The function that would give the zero error second moment M -values is therefore 1.732 times this function

$$M_{\text{sec,zero error}} = 0.7813 + 0.05851\ C_l - 4.95624\times10^{-4}\ \ C_l^{\,2}. \tag{6.8}$$

This remarkable result provides techniques to measure the exact second moment M -value for a large number of relatively good quality beams of both symmetries without measuring the energy density profile of the beams. This is especially useful for high energy pulsed lasers, whose characterisation is difficult to automate due to commonly found low signal to noise ratios.

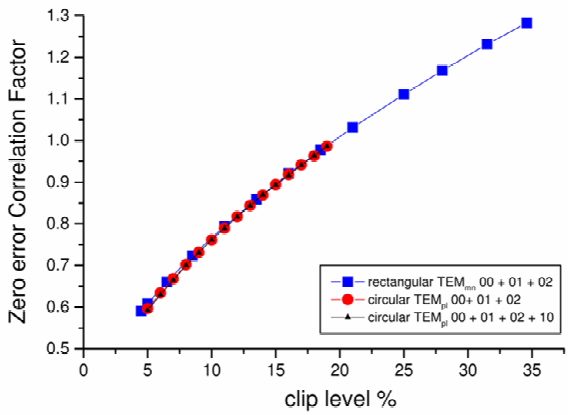

Figure 6-13:Zero error proportionality factors versus clip-level for Gaussian rectangular (red) and cylindrical symmetric (blue) modes.

One such technique is to measure the entire beam energy profile with a knife-edge at several positions along the beam propagation direction as described in Section 4.4.3. If relatively few measuring points are used per radius measurement, the normalised profiles have to be fitted with suitable functions (Section 4.4.4). The beam radii are then obtained by solving the functions using a 16% clip-level (Section 4.4.4). If enough measuring points are used as in constant velocity scans (Section 4.4.3) no fitting functions need to be used and the beam radii can be determined by pixel counting techniques. These beam radii are then to be used in energy and energy flux calculations. The knife-edge M -value is obtained through fitting the beam propagation equation as was explained in Section 4.4.4. The exact second moment M -value is then obtained as follows. If the knife-edge M -value is less than 1.732, the clip-level is lowered in steps to 4.16% and the knife-edge M -value is calculated at each of these clip-levels, the same way as the for the 16% clip-level. If M is higher than 1.732 the clip-level is similarly increased in steps to 35%. The relationship between knife-edge M -values and clip-levels is then fitted with a third order polynomial. The clip-level, which produces the knife-edge M -value of 1.732, is calculated and inserted into Equation (6.8) to determine the exact second moment M -value.

This method can also be used when the knife-edge radius is measured by hand. Larger clip-level intervals must, however, be used because of the large amount of time each knife-edge hand scan takes. A quicker method for hand scanning rectangular symmetric beams is also given in Appendix F.

6.4.5 Numerical calculations for rectangular Gaussian beams

6.4.5.1 Theoretical verification of the analytical proportionality graphs

The numerical program that calculated the rectangular second moment, knife-edge and slit M -values was primarily written to verify the results from the analytical programs. The programming method of this rectangular numerical program was similar to that of the cylindrical numerical program (Section 5.2.1), but completely different to that of the rectangular analytical program. Good correspondence between the outputs of the two rectangular programs implied that only the basic assumptions, which were identical to the two rectangular programs, need to be verified.

Figure 6-14 A and B show the numerically calculated knife-edge and slit second moment graphs overlaying the analytically calculated second moment graphs for the rectangular three-mode subclass respectively. Except for the small numerical error the correspondence between the two different outputs was so good that it was difficult to distinguish between the analytical (magenta) and numerical (blue) outputs. Another good indication of the correctness of the calculations is that the computed second moment, knife-edge and slit M -values of all the pure rectangular and cylindrical modes correspond to that given in theory (Section 3.3.3) as well as to published values [25].

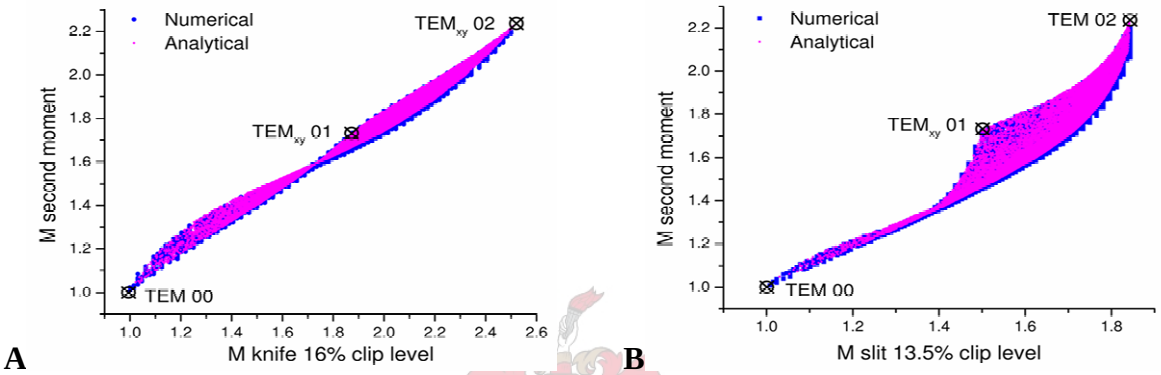

Figure 6-14:Analytical (magenta) and numerical (blue) second moment graphs as a function of the knife-edge (A) and slit (B) M -values of the rectangular three-mode subclass.

6.4.5.2 Evaluation of the numerical sample size

Beam subclasses consisting of a large number of modes need a very large sample number (number of individual calculations or points) to obtain proportionality graphs that describe them completely. For higher mode content subclasses the edges of the proportionality graphs become blurred and the computed values do not extend to the pure modes. This is because some linear superpositions are more likely to occur than others. Not all possible combinations were therefore covered by the amount of computations. This is usually not a problem for subclasses containing a low number of modes.

A mayor drawback of the analytical program is that it takes a very long time (up to a few days on a 1.6 GHz pc) to do even a modest number of calculations. The calculation speed is even further decreased by the addition of more pure modes. In contrast, the numerical *Excel* program can produce an immense number of calculations in a relatively short time. It can

therefore be tested whether the analytical sample size was large enough for subclasses consisting of a relatively high number of modes. This has been done graphically in Figure **6-15** for the rectangular six-mode subclass (up to $TEM_{xy}05$). This subclass was the most prone to under sampling since it consisted of the largest number of modes used in analytical calculations.

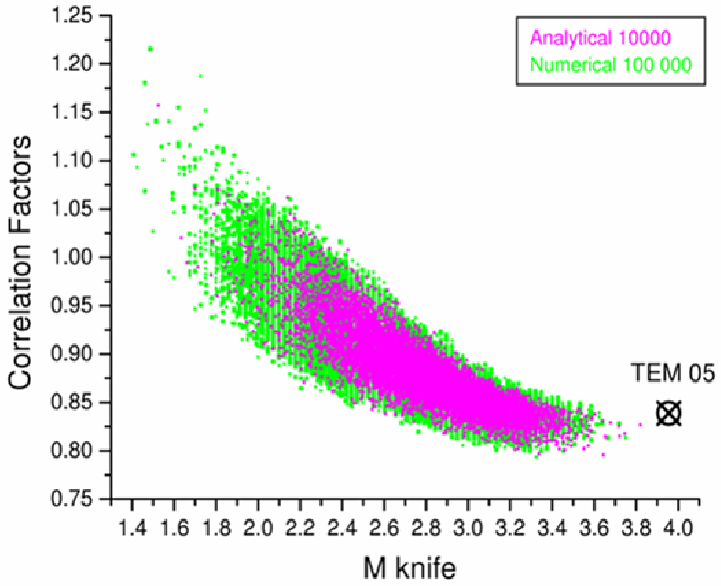

Figure 6-15:Testing of the sample size. The magenta points are the analytical values and number 1 x 10^4 in total. The green points are the numerical values and number 1 x 10^5 in total.

The magenta points were calculated by means of the analytical *Mathematica* program and numbered 10 000 in total. The green points were calculated with the numerical *Excel* program and totalled an order of magnitude more than the analytical points. The only large difference between the two is the higher concentration of sample points at lower knife-edge M -values. The rest of the knife-edge M -values and edges correspond remarkably well. The sample size was therefore deemed adequate for all the lower subclasses.

6.4.5.3 Investigation of beams containing a high number of modes

Another aspect of the numerical program was that its speed was relatively independent of the number of pure modes it used in its calculations. Beams containing a large number of modes (up to $TEM_{xy}0$ 10) could therefore be investigated without straining the memory capabilities of the personal computer. The second moment M -values were plotted versus knife-edge M -values (calculated with a 16% clip-level) for the rectangular two, three, six and eleven-mode

subclasses overlaying each other in Figure 6-16. The linear ISO knife-edge correlation function was superimposed on the computed values to give an estimation of the relative linear behaviour of the rectangular proportionality graphs.

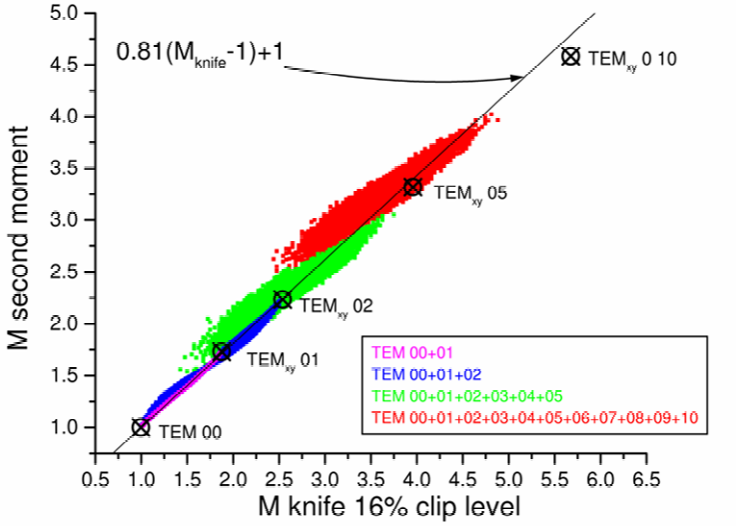

Figure 6-16:The second moment M -values versus their respective knife-edge M-values (16% clip-level) for the rectangular two, three, six and eleven-mode subclasses overlaying each other.

It can be observed that the computed second moment M-values clearly deviate from the linear ISO reference correlation function for subclasses containing a large number of modes. The detachment of the computed second moment values from the pure mode values (seen in Figure 6-1) becomes progressively worse as the mode number of a subclass is increased.

The newly proposed proportionality factor graphs for the four subclasses are shown in Figure 6-17. The proportionality graphs for the six and eleven-mode subclasses appear remarkably similar in that they have approximately the same degenerate error and relative range. The knife-edge values of the rectangular eleven-mode subclass are just shifted to higher knife-edge M -values. It was therefore impossible to fit one function that describes all rectangular subclasses due to this shift. This could already be observed in the deviation of the second moment graphs from the linear reference function. Closer inspection also reveals if linear functions are fitted through the second moment graphs their slope would gradually become smaller (flatter). Even though the degenerate error seemed to remain constant as the number of modes increased, it was still too high for any meaningful accurate correlation. It is

therefore recommended that only rectangular symmetric beams that contain less than three be correlated. The very large degenerate error seen in Figure 6-17 for high mode content beams, demonstrates the extreme importance of measuring the energy content radius rather than the second moment radius to obtain repeatable energy flux values when beams with visibly bad beam quality are used.

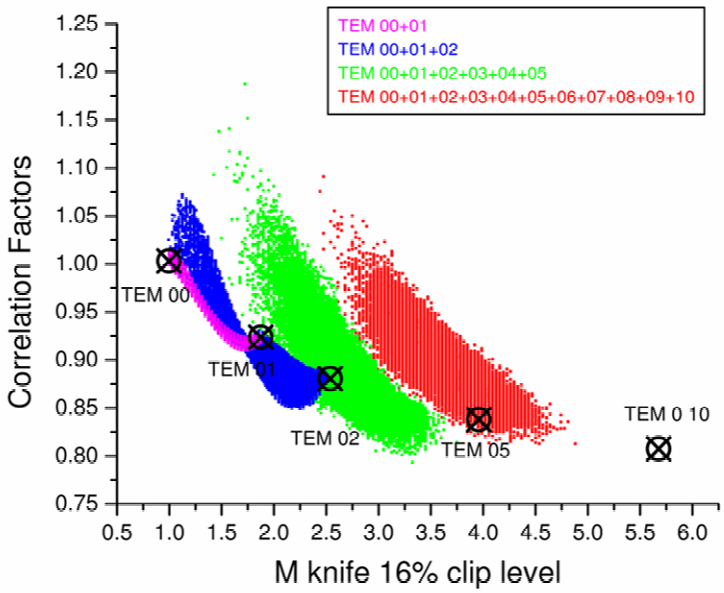

Figure 6-17: The knife-edge proportionality graphs (16% clip-level) for the rectangular two, three, six and eleven-mode subclasses overlaying each other.

6.4.6 Slit correlation for rectangular Gaussian beams

The same procedure that was used to find correlation functions for the knife-edge method is also applied to the slit method. The second moment graphs of Figure 6-2 are divided by the slit M -values to produce the proportionality factor graphs defined in Equation (4.26). These graphs are then also fitted by fifth order polynomials, which are forced through the two TEM_{00} M -values. These fitted functions can be found in Appendix D for rectangular and cylindrical symmetric beams.

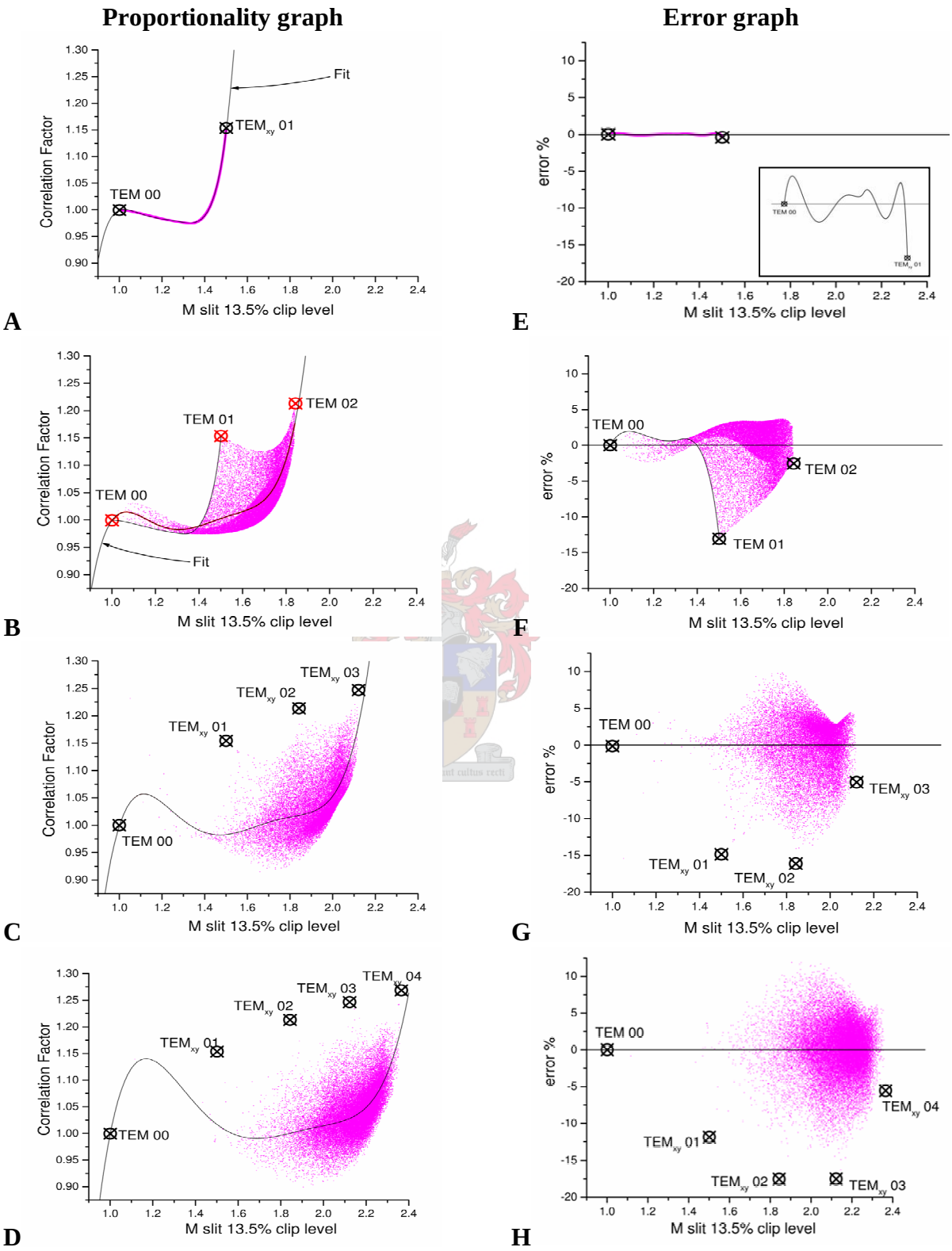

Figure 6-18:Novel slit proportionality graphs for the first four rectangular subclasses (left) and the errors that can be made when the fitted polynomials are used (right).

Figure 6-18 (see page 103) has the same layout as the knife-edge proportionality graphs of Figure 6-5. It can be seen in Figure 6-2 (page 78) that the second moment values do not display the same linearity for the slit M -values and have a larger degenerate error than their knife-edge M counterparts (Figure 6-1). It could therefore be expected that the slit method would be less suited for correlation purposes than the knife-edge method.

The slit proportionality graphs of the rectangular two-mode subclass can be seen in Figure **6-18** A. The fitted polynomial follows the computed values almost exactly for this subclass, just as it did for the knife-edge method. The correlation error is therefore also negligible, as can be seen in the insert of Figure 6-18 E.

The slit proportionality graph of the rectangular three-mode subclass has a very interesting structure. A high density band, which was already mentioned in Section 6.3.2, can be observed at lower proportionality values. Most real beams belonging to the rectangular three-mode subclass will therefore have values in this band, but it cannot be assumed from these calculations that proportionality values of a beam are always part of this band. The fifth order polynomial fitting function follows this high-density band, something the ISO correlation function did not do (Figure 6-4 B page 83). Errors as high as -14% are possible, but unlikely, for the fifth order polynomial fitted through the slit proportionality graph of the rectangular three mode subclass. When the number of rectangular modes is increased beyond three, large positive and negative errors are made. It could be observed that correlation errors as high as 17% are possible, but again unlikely. More realistic errors for these subclasses would be in the region of +7% and -10%.

6.4.7 Slit correlation for cylindrical symmetric beams

6.4.7.1 Separate fitting of subclasses

Figure 6-19 (see page 105) has the same layout as the cylindrical knife-edge graphs in Figure 6-6. It is seen from Figure 6-2 that the second moment M -values of beams containing only cylindrical symmetric modes exhibit much more linear behaviour with respect to the slit M -values than their rectangular cousins. They also have much lower degenerate errors. Fifth order polynomials were also fitted through the proportionality graphs and forced through the values of the fundamental mode as was done for the rectangular subclasses. These can be found in Appendix D.

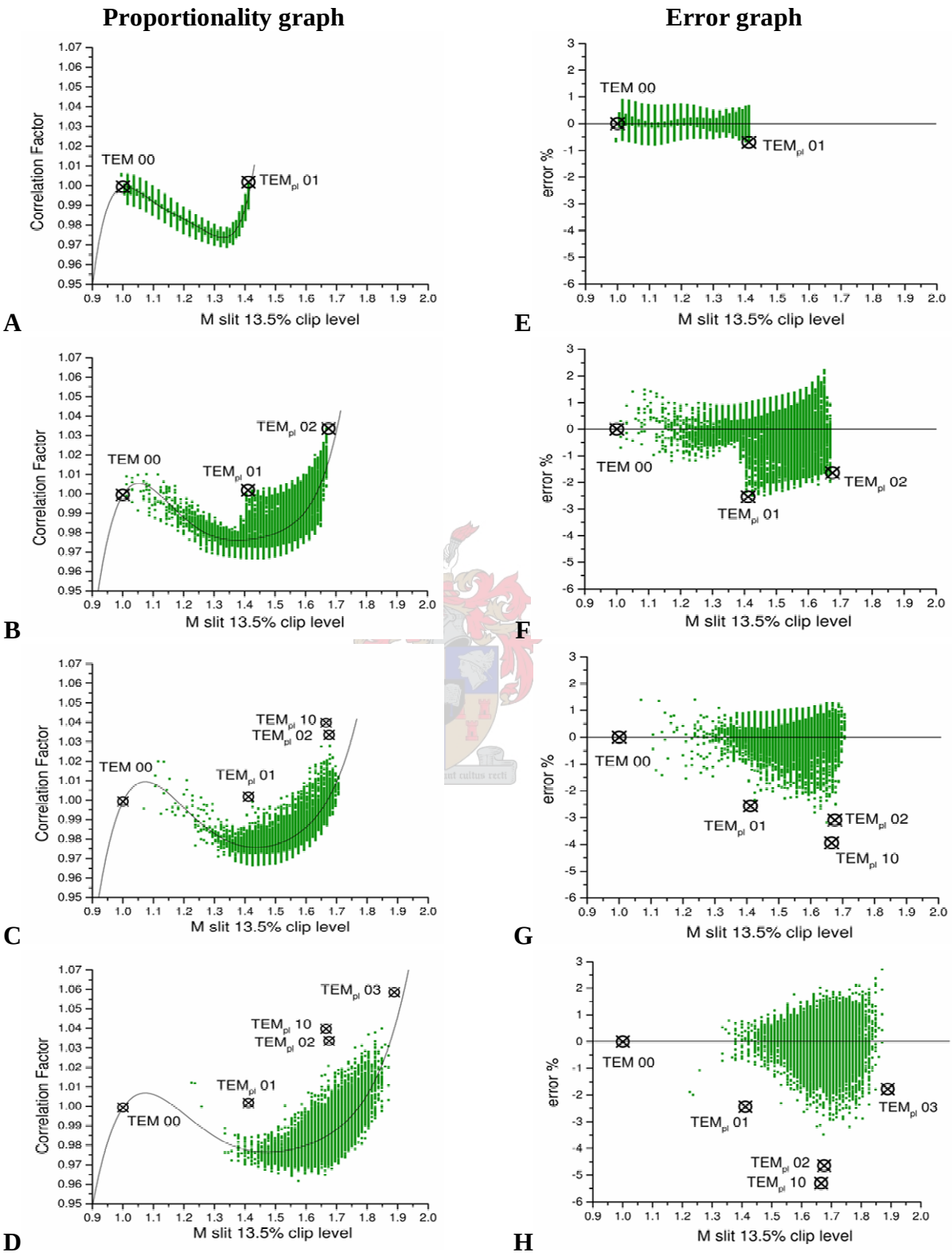

Figure 6-19:Newly proposed slit proportionality graphs for the first four rectangular subclasses (left) and the errors that can be made when the fitted polynomials are used (right).

For the cylindrical two-mode subclass the fifth order polynomial follows the average of its proportionality graph almost exactly (Figure 6-19 A). The maximum numerical error was determined to be ±0.9 % in a similar fashion as was done for the knife-edge proportionality graphs in Section 6.3.1. When the number of cylindrical symmetric modes is increased beyond two, the maximum errors can become as high as -5.5% (Figure 6-19 H). The most probable errors do, however, stay fairly constant at +2% and -3%, which includes the numerical error. The individual correlation functions for the slit M -values therefore have minimal errors for cylindrical symmetric beams.

6.4.7.2 Single cylindrical correlation function

A single function that is able to correlate the slit M -values of the first five cylindrical subclasses fairly accurately should be possible due to the linearity and low degenerate error of the cylindrical proportionality graphs. A linear function was used to do this for the knife-edge method (Section 6.4.2.2), but from Figure 6-19 it is clear that a higher order polynomial is needed for the slit method. The existing fifth order polynomial was therefore fitted through the combination proportionality graph of the first five cylindrical subclasses (Figure 6-20 A). This polynomial can be found by dividing Equation (6.9) by the slit M -value. The error made when using this function can be seen in Figure 6-20 B. The error is small for low slit M -values and gradually increases for higher values. Maximum error values of +3% and -4% are made when this correlation function is used:

$$M_{second} = M_{slit} \times (+0.999381+0.02585(M_{slit}-1.000619)-1.35911(M_{slit}-1.000619)^2 +5.4392(M_{slit}-1.000619)^3-7.97633(M_{slit}-1.000619)^4+4.06871(M_{slit}-1.000619)^5) . \quad (6.9)$$

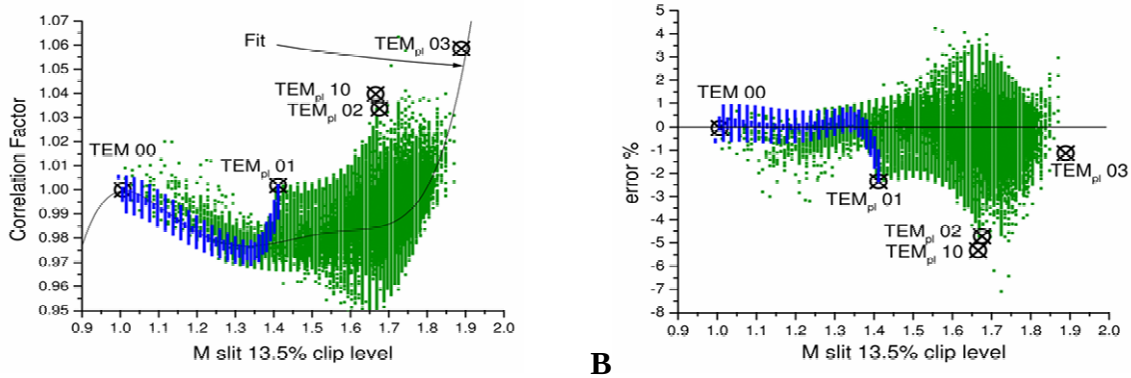

A **B**

Figure 6-20:Novel slit single correlation function for the first five cylindrical subclasses (left) and its possible errors (right).

6.4.8 The effect of the slit clip-level on the proportionality graphs

The 13.5% clip-level proportionality graph for the rectangular three-mode subclass contains a minimum error point close to a slit M -value of 1.4, which resembled the knife-edge zero error point discussed in Section 6.4.3.1. The clip-level was therefore changed in large steps to investigate whether this minimum error point could also potentially be used as was done for the knife-edge method. Figure 6-21 shows that as the clip-level is changed, only the left lobe (at lower slit M -values) is dramatically affected. Its degenerate error increased with clip-level and vice versa. The minimum error points degenerate error also increases until it becomes almost invisible at higher clip-levels. The degenerate error of the right lobe (at higher slit M -values) remains almost constant. The minimum error point could therefore not be exploited.

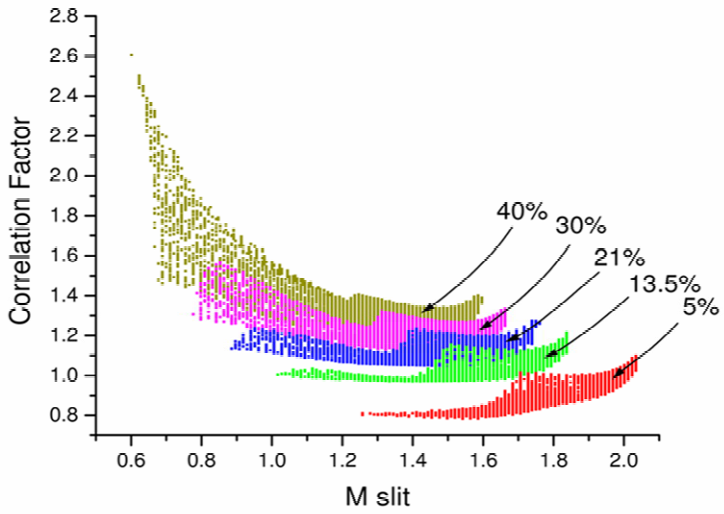

Figure 6-21:Effect of a clip-level change on the slit proportionality graphs of beams containing the first three rectangular modes.

The slit clip-level was also changed in large intervals for the cylindrical three and four-mode subclasses. The results can be seen in Figure 6-20 A and B respectively. The same behaviour as was seen for the rectangular three-mode subclass (Figure 6-21) was also observed for both subclasses. There is therefore no slit correlation technique that encompasses both cylindrical and rectangular symmetric modes.

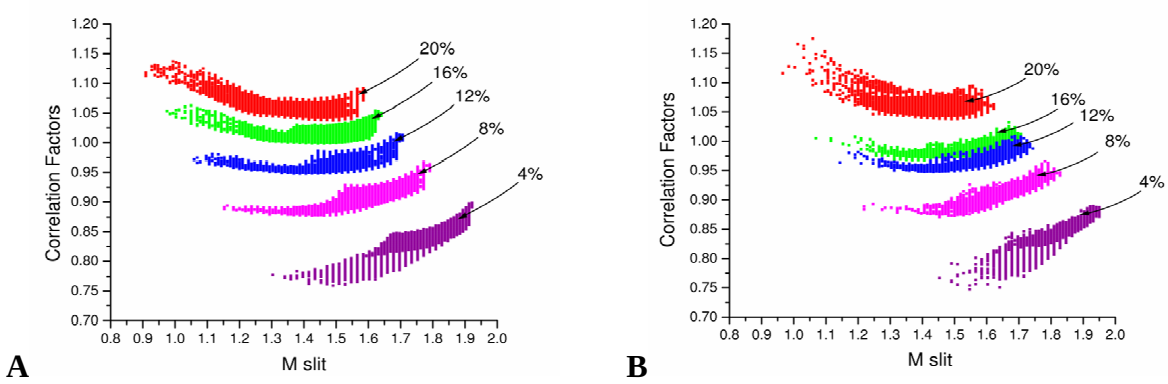

Figure 6-22:Effect of a clip-level change on the slit proportionality graphs of beams containing the first three (left) and four (right) cylindrical modes.

6.5 Comparison between the knife-edge and slit methods

The knife-edge rectangular graphs exhibit more linear behaviour and have much lower degenerate errors than the slit method in general. The knife-edge method also has a zero error point that can be exploited by a symmetry unified zero correlation error method. The slit method is also subject to the same signal to noise limitations as the second moment method. This makes it impossible to use in some set-ups. Because of these qualities, the knife-edge method is judged superior to the slit method for correlation purposes.

6.6 Verification of proportionality graphs by means of published experimental results

In order to experimentally verify the proportionality graphs, complete second moment, knife-edge and slit measurements of a large number of different beams need to be performed. This can either be done separately by means of different beam scanners, or combined by means of accurate slit scans or camera measurements. The slit energy density profiles can be determined by mathematically integrating two-dimensional energy density profiles as was done in Section 5.2.1.2. Knife-edge energy profiles can in turn be obtained by mathematically integrating these slit energy density profiles as was done in Section 5.2.1.3.

It was not possible to do a complete camera or slit characterization to verify the computational results because such a system was not available. An assessment of whether the computational results describe real laser beams could, however, be made by using published results. Johnston et al. [27] proposed the correlation functions that the ISO adopted in their 1999

standard ISO 11146 [24]. Johnston provided the modelled second moment, knife-edge (16% clip-level) and slit (13.5% clip-level) M -values of the beams they used to determine the ISO correlation functions (Section 4.5.3). They also provided the measured second moment and knife-edge (16% clip-level) M -values of seven beams from different laser systems to test their knife-edge correlation function. They used a Coherent Mode Master mechanical scanner to measure the knife-edge M -values and to obtain one-dimensional pinhole profiles from which the second moment radii were calculated. The average noise was subtracted from the pinhole profile and it was truncated in the calculation of the second moment radii. No additional noise deduction techniques were therefore used.

6.6.1 Knife-edge verification

The clip-level optimisation method could not be verified with Johnston's data since complete data sets were not given. Only the knife-edge and slit M -values calculated with 16% and 13.5% clip-levels respectively were given. The knife-edge results from the test beams, as well as those from the modelled beams that were used to obtain the correlation functions, are superimposed on some of the knife-edge proportionality graphs of Sections 6.4.1 and 6.4.2.1 (Figure 6-23 and Figure 6-24). Only the rectangular graphs need to be used since they incorporate the cylindrical symmetric graphs (Section 6.4.3.1). Figure 6-23 shows the superposition of these values on the proportionality graphs of the rectangular three (A) and four-mode (B) subclasses.

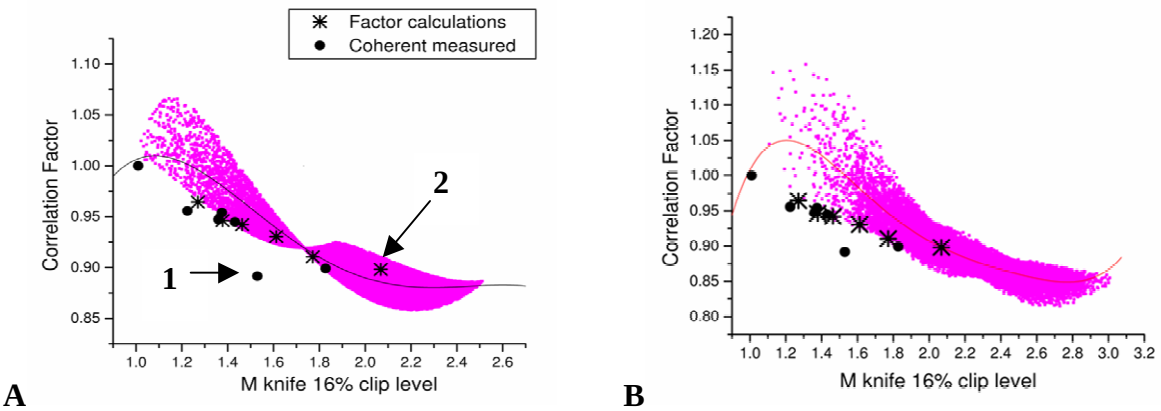

Figure 6-23:Superposition of published values on the knife-edge proportionality graphs of the rectangular three (left) and four (right) mode subclasses.

The values of the modelled beams all correspond to those of the proportionality graphs. This is not surprising since they, like the computed results, were also mathematical constructs of laser beams. The experimental measurement technique Johnston used is almost identical to the theoretical one used in the programs of Chapter 5. There are differences however. Johnston employed one-dimensional pinhole profiles and not slit profiles. Section 5.1.2.1 shows that the latter method is incorrect when evaluating cylindrical symmetric beams. Johnston also manually selected a few profiles, whereas the programs of Chapter 5 considered large subsets of Gaussian profiles.

Only one of the measured beam M -values differs substantially from the computed values. All the other values correspond within error limits ($\pm 2\%$), but most are lower than the average of the computed values for the rectangular three-mode subclass. The most probable explanation of this is that Johnston used truncation limits that were too small in the calculation of the second moment radii. This demonstrates how difficult it is to accurately determine the second moment M -values. This truncation is most likely also the explanation for the very low second moment value of the beam indicated by the number 1.

Johnston's modelled beam with the highest knife-edge M -value (indicated by the number 2) had a higher proportionality value than the average of the computed values of the rectangular three-mode subclass. It is suspected that the beam belongs to the rectangular four-mode subclass due to the trend of the others to have lower values than the average of the computed values. This was confirmed by the observation of three minima in the one-dimensional pinhole profile of this beam [27].

The cylindrical proportionality graphs would be expected to correspond better to the beams that were used to obtain Johnston's correlation functions since cylindrical symmetric functions were used in their modelling. This could indeed be observed in Figure 6-24 A. The M -values of beam 2 did not correspond to the computed values even for the cylindrical six-mode subclass (up to $TEM_{pl}03$) as can be seen in Figure 6-24 B. It therefore fell outside the cylindrical symmetric range investigated in this thesis.

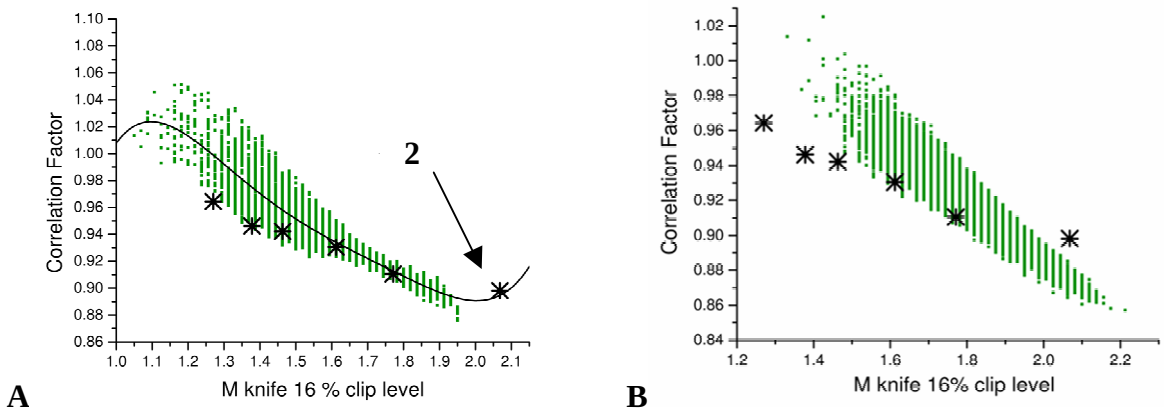

Figure 6-24:Superposition of published values for modelled beams on the knife-edge proportionality graphs of the cylindrical four (left) and six (right) mode subclasses.

6.6.2 Slit verification

The report by Johnston provided only the slit M -values of the modelled beams that were used to determine the correlation functions. The slit M and proportionality values of these beams were superimposed on the rectangular three and four-mode proportionality graphs of Sections 6.4.6 and 6.4.7.1 in Figure 6-25. Once again, the values of the modelled beams (except 2) correspond with the rectangular three-mode proportionality graphs.

In Figure 6-23 A the knife-edge proportionality values of beam 2 with the highest slit M -value coincides with the computed values for the rectangular three-mode subclass, but from its pin-hole profile it was found that it rather belongs to the rectangular four-mode subclass. In Figure 6-25 A it can be seen that the slit proportionality factor for this beam does not correspond to the computed proportionality values for the rectangular three-mode subclass. It is therefore an elegant confirmation that this beam does not fall within the rectangular three-mode subclass as it appears in the knife-edge proportionality graph.

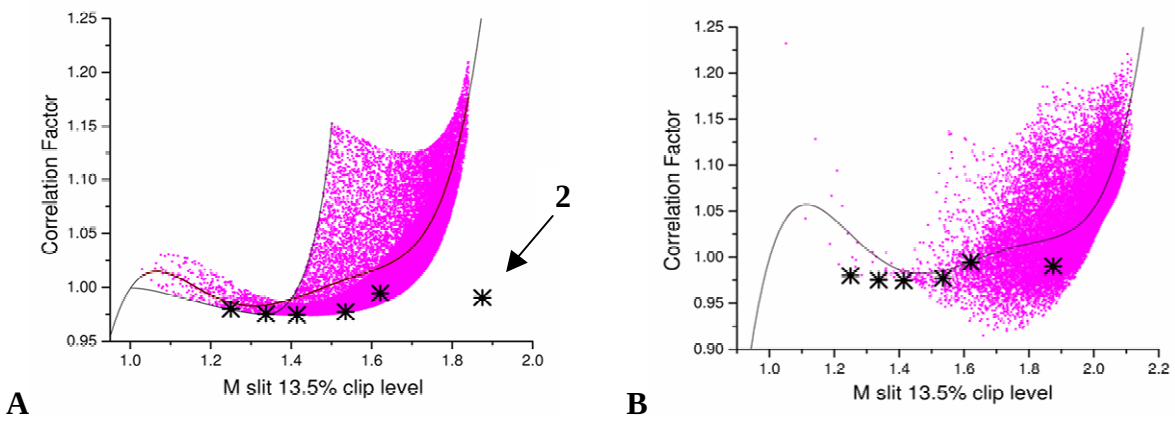

Figure 6-25 Superpositions of published modelled beam M -values on the slit proportionality graphs of the rectangular three (left) and four (right) mode subclasses.

It can be seen in Figure 6-26 A that the proportionality values of the modelled beams correspond better to the cylindrical computed values for the same reason mentioned in the previous section. The slit proportionality values of the beam 2 also do not correspond to any of the computed values even for the cylindrical six-mode subclass shown in Figure 6-26 B.

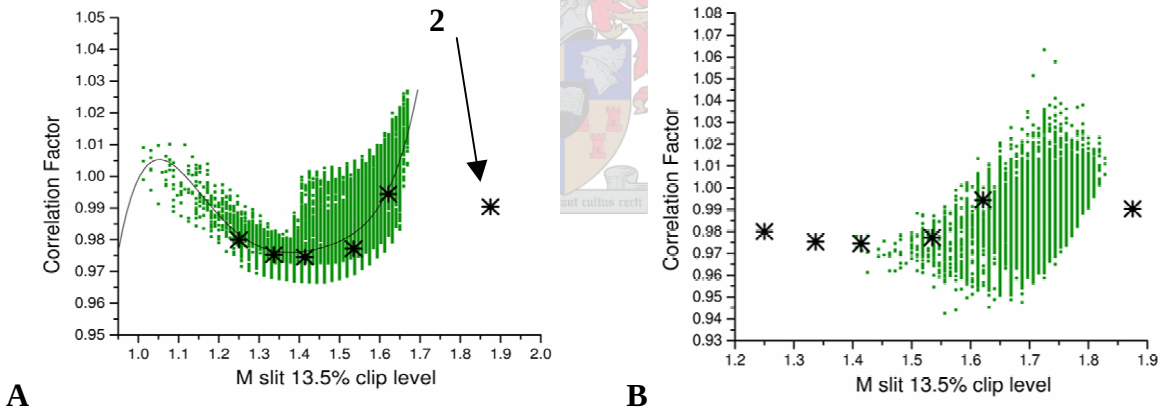

Figure 6-26:Superposition of published modelled beams values on the slit proportionality graphs of the cylindrical four (left) and six (right) mode subclasses.

This sample is too small to evaluate the proportionality graphs and functions. It also contains possible calculation errors due to noise deduction errors and wrong profiles. It is proposed that new verification experiments be performed with accurate camera profilers, new noise elimination algorithms and stable laser systems.

6.7 Summary

The ISO correlation functions were evaluated using computed values, calculated with three programs, using both rectangular cylindrical symmetric base functions. Various new correlation functions and techniques have been proposed for both the knife-edge and slit methods. An attempt was also made to verify the proportionality graphs that were used to obtain the new correlation functions by using published results. In the next two chapters, the proportionality graphs will serve as a tool to evaluate two experimentally characterised beams.

Chapter 7

Experimental set-up and techniques

The initial aim of this project was to modify and characterise a CO_2 TEA laser for material processing purposes. The theory developed in the previous chapters will be applied to evaluate and correlate beams emanating from this laser. The data from this characterisation will be used to illustrate the newly proposed clip-level optimisation method. This chapter will examine the laser, measurement equipment (hardware), set-up, methods, software and post processing techniques to achieve these objectives.

7.1 The laser source

The type of laser that was characterised was a mini CO_2 TEA laser provided by the company Scientific Development and Integration (SDI) located in Pretoria, South Africa [42]. The laser resonator consisted of a flat molybdenum back reflector, internal mode restricting aperture and curved ZnSe output coupler (15m radius, 70% reflecting). The distance between the back reflector and output coupler was 0.5m. Figure 7-1 illustrates this in an outline sketch of the laser.

The discharge is generated between two profiled discharge electrodes (see Figure 7-1). Beam directions will be defined as parallel (vertical) and perpendicular (horizontal) to the discharge.

A rich gas mixture consisting of 20% CO_2 and 20% N_2 in 60% He (mixed by means of percentages of the total pressure) was used. This provided high energy, long tailed laser pulses that favoured the formation of beams that consisted of a large percentage of higher order modes [30].

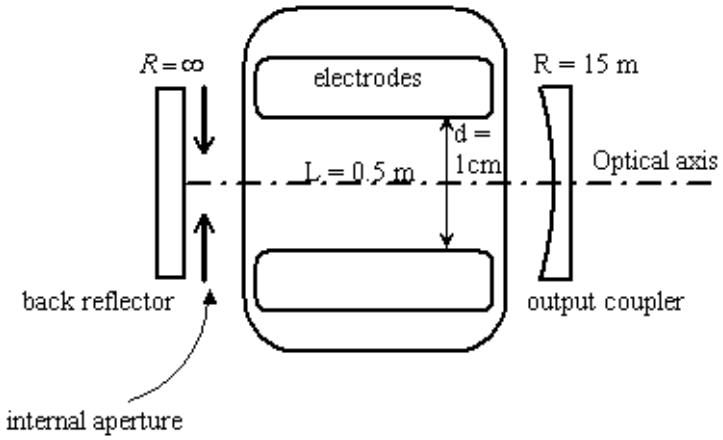

Figure 7-1: Outline sketch of the mini CO_2 TEA laser.

Repeated optics failures were encountered during the initial experiments using the laser. This was due to layer formation on the inside of the resonator optics, which was in contact with the laser gas. Because of this, it was impossible to obtain repeatable beam quality measurements. Further investigation revealed that the stainless steel pre-ionisation pins were responsible for a red iron oxide layer residue on all the internal parts of the resonator causing optical degeneration. To prevent this, the pins were replaced by machined titanium welding rods. The pin holders also had to be redesigned, which led to the extra improvement of the pins being spring loaded to make them easily adjustable. An internal aperture had to be developed at this stage since no good quality undamaged windows were available. The internal aperture eliminated the need for a window, externally mounted aperture and external mirror holder. The aperture was designed so that it fitted exactly into the optical mount of the laser. Figure **7-2** shows a drawing of the position and shape of the internal aperture and Figure 7-3 shows two photos of the internal aperture. The optimal size of the internal aperture was experimentally determined by observing the output profiles of beams formed when the resonator contained different apertures which differed by 0.5mm in width. The optimum diameter of 6.5mm was very near to that of the theoretically calculated fundamental TEM_{00} mode so that all other modes were suppressed. A drawback of this design was the extreme alignment sensitivity of the resonator because the optical axis needed to coincide precisely with the centres of all the optical mounts. Accurate alignment was achieved by means of precision-machined alignment aids, long alignment distances and lots of patience.

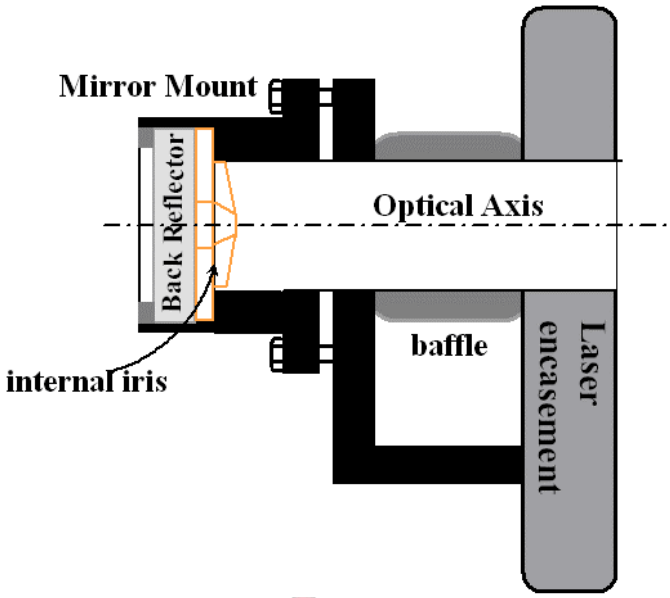

Figure 7-2: Design drawing of the position and shape of the internal aperture.

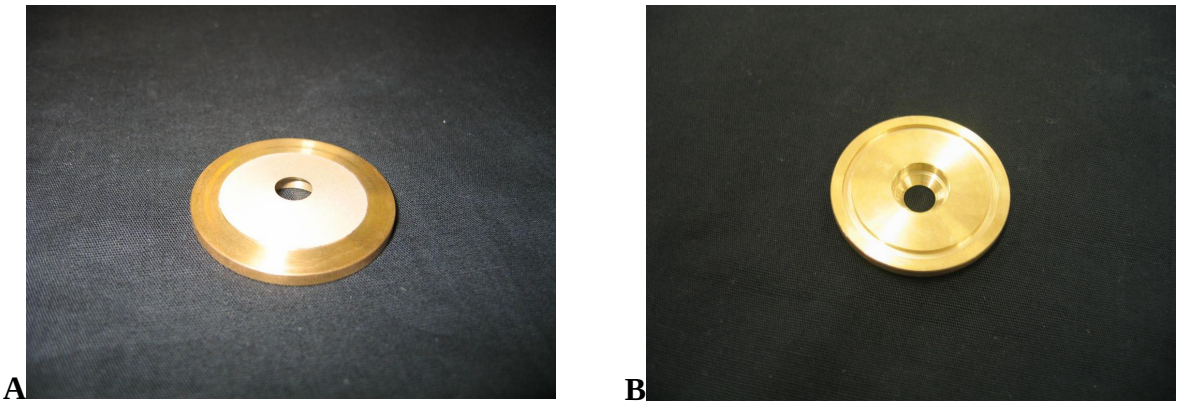

Figure 7-3: Photos of the internal aperture. The side shown in A faces towards the discharge and the side shown in B fits onto the back reflector by means of an O-ring.

This internal aperture had several benefits:

- The sealed resonator eradicated dust on the internal optics. Since the energy density was extremely high inside the resonator impurities were burned onto the optics. This possibly led to higher mode selection or, in the worst case, to beam distortion (if the beam is distorted the Hermitian and Laguerre functions can no longer be used to describe the laser energy density function, invalidating the theory developed earlier).
- The molybdenum mirror was more burn damage resistant than a ZnSe window, even with impurities in the resonator. It could also easily be cleaned.
- For externally mounted optics, the danger existed that the laser could be misaligned by accidental impact to the protruding mirror mount. This danger was therefore reduced because the extra mounting plates for the external mirror and aperture holders were eliminated.
- The internal aperture was also cost effective since the high quality expensive window was eliminated. This window also needed replacement from time to time, as all optics of frequently used lasers do. The mirrors can be cleaned so that the overall cost of the laser was reduced and the lifetime was increased.

7.2 Beam propagation

Two beams from the CO_2 laser were analysed. The first beam emanated from the laser resonator when it contained no deliberate internal aperture. This beam will be referred to as the multimode beam. The second beam emanated from the laser resonator when it contained the 6.5mm aperture discussed in Section 7.1. This beam will be referred to as the near TEM_{00} beam. A third beam emanating from the resonator when it contained an 11mm aperture was also used to find the optimal measuring parameters. It will be clearly stated when results from this beam are used.

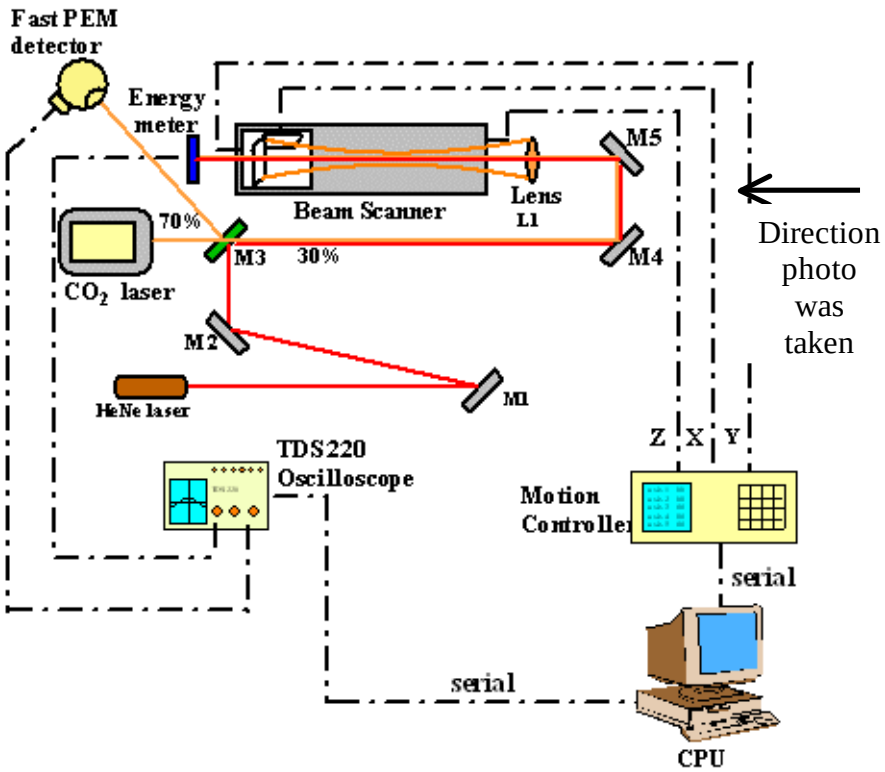

Figure 7-4: Schematic of the beam propagation, measurement and control set-up.

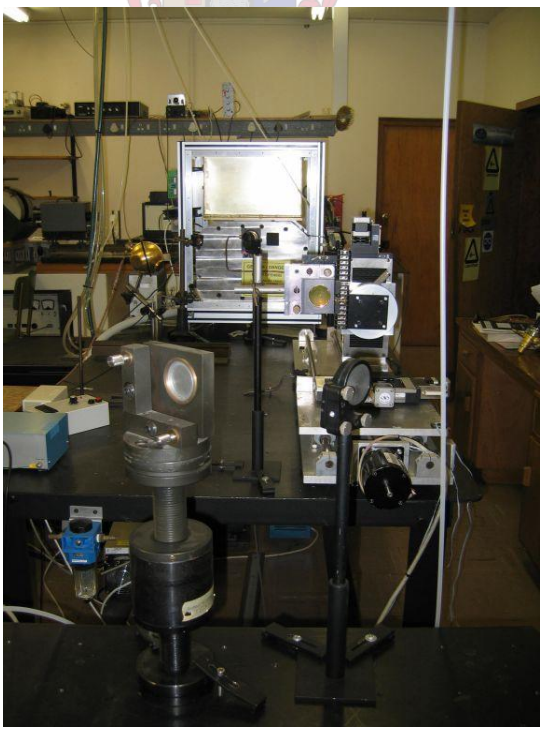

Figure 7-5: Photo of the laser, measurement equipment as well as of the beam attenuating, steering and focussing optics.

The experimental set-up for characterising the CO_2 laser is shown in Figure 7-4. The beam exited the laser at the output coupler and was then split with a 70% Germanium partial reflector M3. Thirty percent of the beam was transmitted while the remainder was reflected into an integrating sphere. Two molybdenum mirrors M4 and M5 was used to steer the beam through a ZnSe lens with a 0.5m focal length, positioning the beam parallel to the movement of the long axis of a beam scanner. The beam was scanned with either a knife-edge or a slit and the transmitted energy fell onto an energy meter (Gentec joule meter Model ED-500). The transmitted beam energy was reduced to 30% by M3 to prevent plasma formation on the scanning surfaces at the focus of lens L1. M3 was also used to superimpose a red HeNe guide beam (635.8nm) onto the invisible infrared beam ($10.6\,mm$). A photo of the set-up can be seen in Figure 7-5.

7.3 Measurement and control equipment

7.3.1 Overall set-up

Most of the beam scanning procedure was computer automated. A Pentium 3 personal computer (PC) interfaced by means of a serial port with a motion controller (Newport Universal Motion Controller ESP 7000). The motion controller in turn powered three translation stages in the x, y and z Cartesian directions of the laboratory system.

The laser energy that was transmitted by either the slit or knife-edge was measured with a large area energy meter. (Gentec Model ED-500). The signal from this meter was fed into a digital oscilloscope. The Tektronix TDS 220 oscilloscope was also interfaced by means of its serial port to the PC, from which its settings could be adjusted and its output waveforms analysed.

The part of the beam that terminated in the integrating sphere was measured with a fast Pyro Electric, or PEM detector (Vigo systems PEM.L.2). This detector could detect rise times of down to 1ns and could therefore resolve the shape of the laser pulse as well as the transverse and longitudinal mode beat frequencies. The signal from the detector was also fed into the TDS 220 digital oscilloscope. Measurements made with this detector are, however, not included in this thesis due to conciseness.

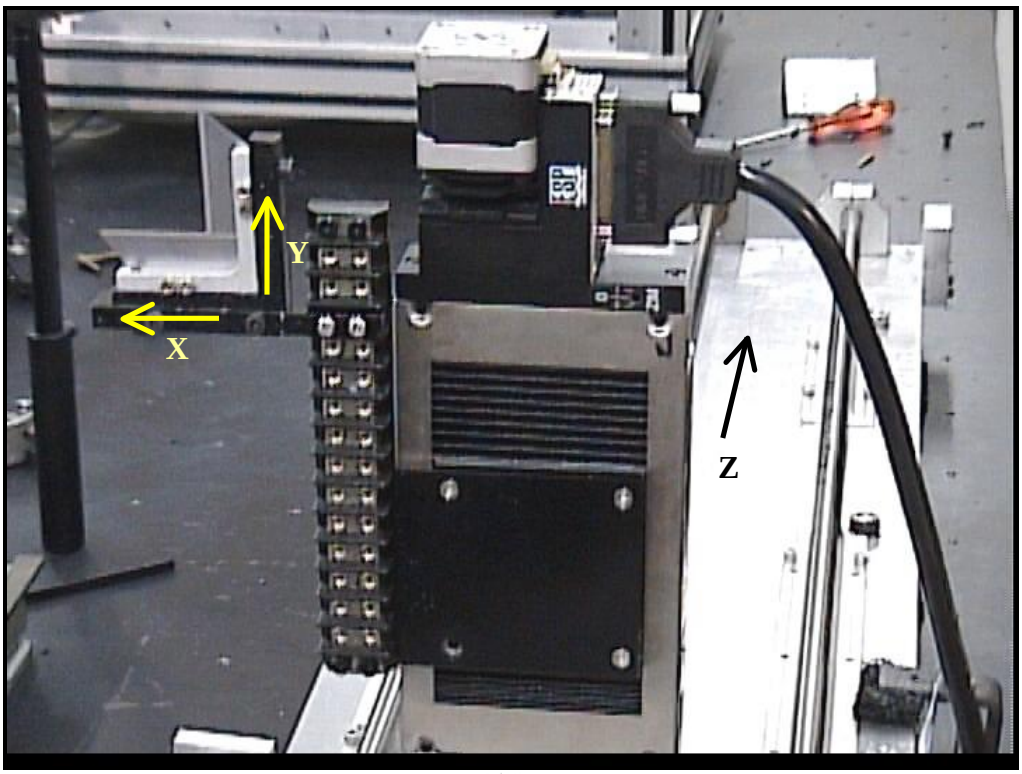

Figure 7-6: Photo of the beam scanner with knife-edges mounted illustrating the three Cartesian directions.

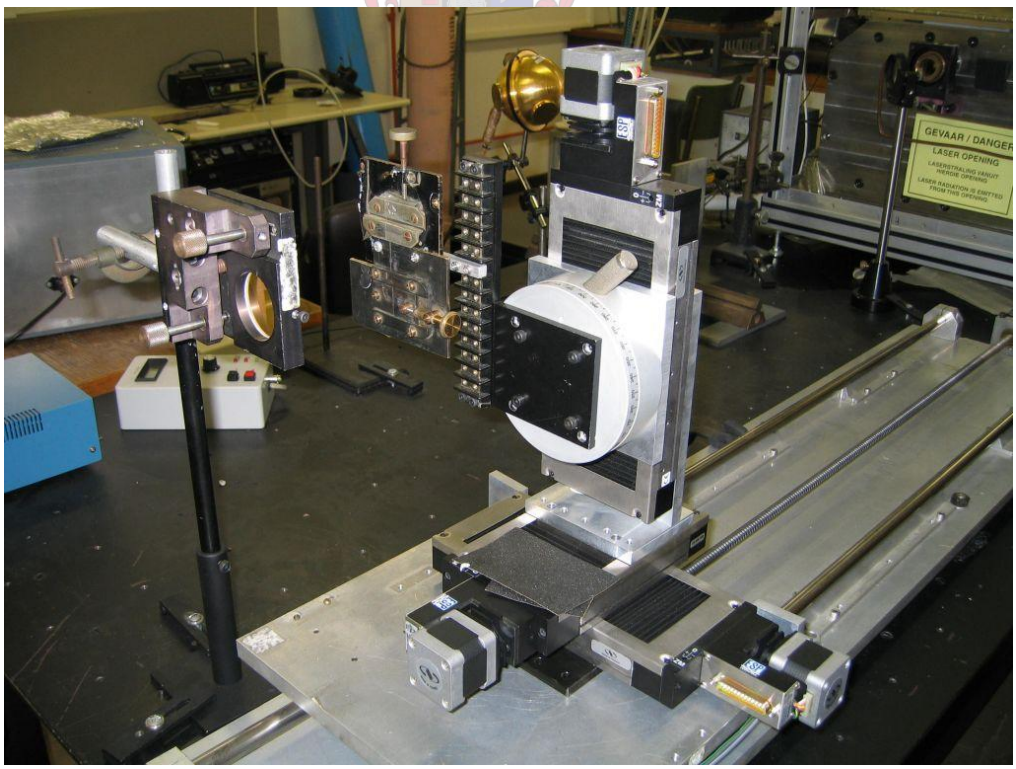

Figure 7-7: Photo of the beam scanner with the slits mounted.

7.3.2 Scanning hardware

The beam scanner consisted of the following components:

- An 850mm long z stage and carriage whose direction coincided with the beam propagation direction.
- State of the art 100mm range Newport translation stages, accurate to $5\,m$ m, were used to move the scanning edges in the two transverse directions.
- Two knife-edges were positioned perpendicular to each other in order to perform knife-edge scans in the horizontal (x) and vertical (y) directions.
- Two slits were also mounted perpendicular to each other. Due to the large size of the slits and knife-edges, only one set-up (knife-edge or slit) could be mounted at a time.
- A height adjustable rack mount was used to attach the two different scanning devices onto the vertical Y stage.
- The entire beam scanner was fastened to an optical table using foam rubber to minimize vibrations.

Two photos of the automatic beam scanner that was used to characterise the beam are provided in Figure 7-6 and Figure 7-7 and shows the knife-edges two slits mounted on the beam scanner, respectively.

7.4 Automation software

The entire automation process was run by a program written using the software package *LabView*, from National Instruments. The structure of this program can be summarised as follows:

- Communication was first established between the computer and the motion controller via a serial port (a GPIB communication option was also available).
- The two transverse stages were compatible with the motion controller and merely had to be allocated a drive number because they were automatically recognised by the motion controller. The motion controller had to be specially configured to initialize the existing long stage every time the program was run.
- After communication was established with the TDS 220 oscilloscope, the oscilloscope's functions could be set with a special visual interface (VI) provided by *LabView*. The scanning devices were then manually positioned and the optimised settings were chosen by the user.

- A prewritten text program was read in. This instructed *LabView* (and in turn the motion controller) to move the translation stages to specifically required three-dimensional positions. This program was first written in *Excel* after which it was copied into a text editor (*Notepad*).
- The computer then instructed the motion controller to move the stages to their initial starting positions.
- The oscilloscope was set so that the waveform was already averaged over sixteen shots when it was read in by the PC. This waveform was then fitted with a standard forth order polynomial by *LabView* (provided in the VI for the oscilloscope), after which the peak to peak value was calculated and recorded with the specific three-dimensional x, y and z positions of the scanner.
- The computer, after recording the energy and position values, instructed the motion controller to move the stages to the next scanning position that was provided by the prewritten text program.

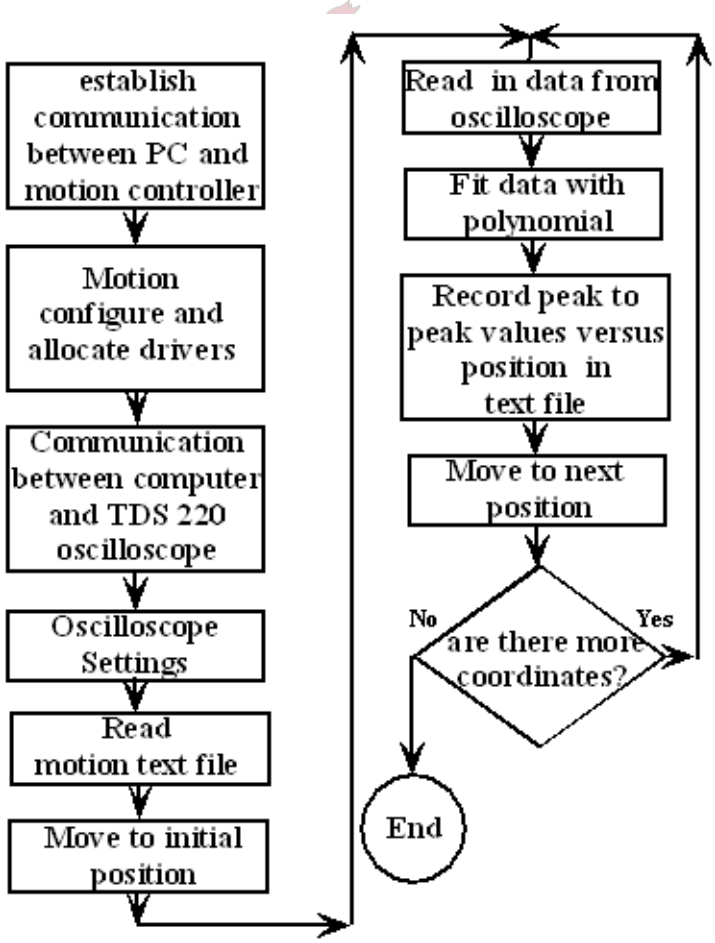

Figure 7-8: Structure of the automated beam-scanning program.

7.5 Slit scanning

Two slit scans were performed in each of the two principle directions. The first scan was a pre-scan to obtain a first assessment of the beam and consisted of only 20 measuring points. The second scan, which consisted of 200 measuring points, was done to measure accurate beam profiles from which the second moment radius and SPSM proportionality factors (Section 4.5.1) could be calculated. It was found that, with the beam energy reduced to 30% by the partial reflector (Section 7.2), the signal to noise ratio was very small, making slit profiles unreliable. The Germanium partial reflector therefore had to be removed before any slit scans could be performed, making complete slit scans through the focus of the lens impossible due to plasma formation on the slit edges [1], [11].

7.5.1 Noise subtraction

Noise subtraction is extremely important when calculating the second moment radius. Even minute noise levels in the wings of the beam can lead to large errors. This is due to the fact that values in the wings are further away from the centre so that they have a large moment. Noise errors are a major drawback of the second moment method and various companies have developed and patented methods to reduce noise. Spiricon holds a patent in which algorithms essentially calculate the noise and then deduct it. A theoretical TEM_{00} beam is created to which noise is added with a Gaussian distribution similar to that found in cameras. The beam width accuracy can be precisely calculated in this way [48].

A different noise deduction technique was employed in this thesis because the precise method Spiricon used is patented. The average of the noise was deducted from all the slit measured energy values. The positive and negative parts of the noise then cancel each other out in the second moment calculations. A large amount of noise measuring points is needed for this method to give accurate results. The average of the fifteen noise devoted points was found not to be statistically representative and more had to be located in the wings of the measurement. It is therefore recommended that the number of noise measurement points be increased to at least 30. A typical average noise deduction can be seen in Figure 7-9. Figure 7-9 A shows part of the wings of the beam in which no noise has been subtracted. In Figure 7-9 B in which the average noise has been subtracted it can be seen that almost half the points are positive and the other half negative, resulting in an almost zero noise moment.

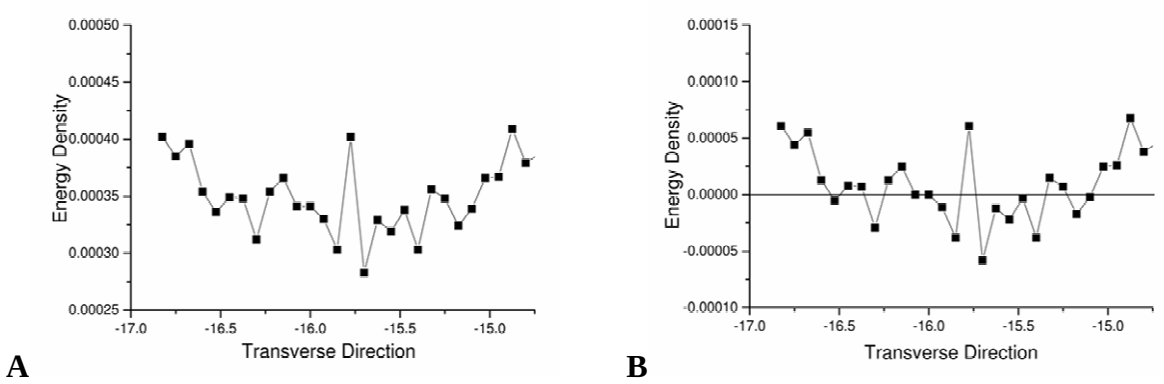

Figure 7-9: Effect of the noise subtraction in the wings of a typical energy density measurement. In A no noise was subtracted. In B the average of the noise was subtracted.

7.5.2 Determination of the optimal slit width

A beam originating from the resonator containing an intermediate aperture diameter (**:** $11mm$) was used to obtain the optimal slit width for both full slit scans. The slit profile was measured using the set-up described in Section 7.3. The slit width was first increased until an adequate maximum signal was obtained. After comparing this slit width to a very rough approximation of the measured beam diameter, it was found that the slit diameter did not fulfil the ISO specification of being $1/20^{th}$ of the beam diameter [24]. Regardless of this, a slit scan was performed in the vertical direction consisting of 500 steps. The slit width was then further decreased until it was approximately $1/20^{th}$ of the approximated beam diameter. Another scan in the vertical direction consisting of 500 steps was then performed using this slit width. The maximum slit transmitted energy was found to be very small at this slit width.

The normalised slit profiles, with average background noise deducted from both measurements, can be seen in Figure 7-10. It can be observed that the scan using the wide slit width did not have nearly as much noise superimposed on its profile as the one from the narrower slit width. The profile from the narrower slit, however, had a significantly smaller beam radius and also indicated that the beam had more structure closer to its energy density maximum. The wide slit therefore did not measure the beam adequately, generating a second moment radius that was too large. This error is well known and is classified as a convolution error (Section 4.2.3). On the other side, the signal to noise ratio of the profile from the narrower slit is so low that its second moment radius could not be adequately determined due to the large noise sensitivity of this method.

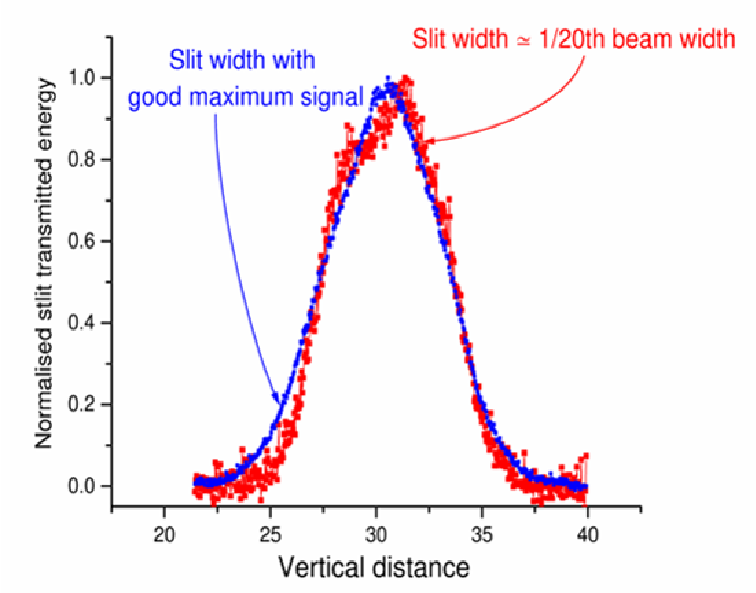

Figure 7-10:Vertical profiles using different slit widths of a beam originating from a resonator containing an 11mm aperture.

The set-up had to be adjusted to increase the signal to noise ratio by removing the partial reflector M3. The increased energy, however, caused plasma formation on the scanning surfaces at measuring positions close to the beam waist. Through more experimentation it was found that there was no energy setting or set-up configuration where a small signal to noise ratio and plasma formation could simultaneously be avoided for slit scanning. The beam characteristics could only be measured with the knife-edge method, which utilised the entire beam energy, using the available detector (which was a standard energy meter). The second moment and slit M -values could therefore not be directly measured since the entire beam propagation could not be determined using the slit method.

In subsequent slit scanning experiments, without the partial reflector, good slit signal to noise ratios were obtained and one or two slit scans were performed outside the troublesome waist region. The beam energy density profile could therefore be assessed before the time-consuming complete knife-edge characterisation commenced. Slit scans were carefully done in both principle directions of both beams using five hundred steps for each slit profile.

The angle between the laboratory and the beam system was also adjusted to zero using the intermediate 11mm aperture beam and the method described in Section 4.4.6. The kurtosis parameter remained reasonably constant at a value of close to 1.8 at two beam positions in the

vertical direction (close to and far from the laser) for the 11mm aperture beam. This beam could therefore be classified as simple astigmatic. The slit profile was not, however, measured in more than one z position for the near TEM_{00} and multimode beams. It was therefore assumed that these beams could also be classified as simple astigmatic. This assumption was incorrect as will later be seen in Chapter 8.

It was quite possible that the beam shifted between the two measurement techniques because the attenuator (which was wedged) had to be inserted each time for knife-edge scanning. The extra steps could be a source of additional errors making this method of determining the correlation factor very precarious, even though great pains were taken to minimise this shifting of the beam.

7.6 Knife-edge scanning

A complete automated knife-edge pre-scan was not feasible since it would have taken too long. Two knife-edge pre-scans, one manual, and the other semi-automated, were therefore done before the main detailed scan.

Quick manual pre-scans in both the transverse directions at every z position were first performed to determine preliminary scan ranges. These preliminary scan ranges were in fact a rough estimation of the beam radii and therefore of the beam propagation. An estimation of the waist position $z(0)$, and Rayleigh range z_0, could be made by plotting the preliminary pre-scan ranges versus propagation position z in an *Excel* graph. This is especially important since half the measuring points should fall within the waist region [24]. The measuring point distribution could therefore be adjusted after the first manual pre-scan.

The second pre-scans were semi-automated. The text program that instructed the computer and motion controller to move the translation stages (Section 7.4) were automatically generated by *Excel* using the range values of first manual pre-scans. The function of these pre-scans was to calculate relatively accurate ranges for the next detailed scans. They consisted of only 10 steps per transverse direction per z position and were therefore relatively quick. A Matlab fitting program was then used to fit the normalised second pre-scans with the knife-edge TEM_{00} energy function (Equation (4.9)). The final ranges were automatically determined by doubling the Gaussian radii from the fitting function and then

adding and subtracting these doubled values to the approximate centre positions of the beam at the various z positions.

A text program for accurate scans (using a large number of steps) was generated in Excel using the final calculated ranges. The program had the following steps in each transverse direction at each position:

- The first three measuring points were dedicated to measure the noise. The measurements were made one scanning distance from the minimum energy range value so that the beam was completely blocked off.
- The knife-edge was then moved to the minimum energy range position from where it traversed to the maximum energy range position in thirty-five steps recording the transmitted energy at every position.
- After the maximum energy range value was read in, the knife-edge was moved a further scanning range distance, ensuring that the whole beam was transmitted. The maximum energy was then accurately measured using fifteen measuring points. This large number of points was necessary because the beam radii were found to be sensitive to the normalising maximum energy. The degree of sensitivity was determined and is given in the next chapter in Section 8.2.6.

After a successful scan the data was copied into an Excel sheet where graphs were automatically generated for evaluation. Any erroneous point due to arcing in the laser could be deleted at this stage.

7.7 Matlab post processing

The output data in text files created by *LabView* and modified in *Excel* were read into the mathematical program *Matlab*.

The data sets for each one-dimensional knife-edge profile scan were made descending in energy values from low to high transverse distance values. This was necessary due to the physical orientation of the translation stages that made the data descending in energy values in the horizontal (x) direction and ascending in energy values in the vertical (y) direction. The same post-processing program could then be applied to data from both directions. The following actions were then performed on the data set of each one-dimensional scan.

The mean of the fifteen maximum energy (unobstructed beam) data points as well as the mean of the three noise data points (beam is completely obstructed by the scanning edges) were obtained. The mean noise was then subtracted from the data point values after which they were normalised by the mean (noise subtracted) maximum energy. The data points that were used to calculate the maximum energy and the noise were then discarded. The rest of the data points were fitted with TEM_{00} (Equation (4.9)) and the $TEM_{x,y}$ 00+01 (Equation (4.10)) functions. The data points were then plotted overlaying the fitted TEM_{00} function for final post-accuracy evaluation.

The three fitted parameters P_1, P_2 and P_3 had to be inserted back into the fitting function Equation (4.10), which was then solved for the minimum and maximum energy clip-levels (normally 16% and 84%, see 24). The difference between the two solutions was then taken as the beam energy radius (Section 4.4.4), which is used in all further calculations. Note that the beam radius was not immediately obtained from the fitting parameters as would be the case when the normal TEM_{00} knife-edge energy distribution (Equation (4.9)) is fitted.

The beam radii for all the z positions were calculated in this way to produce the beam propagation in both transverse directions. The M^2 parameters in any one of the transverse directions were then calculated as follows. The propagation hyperbola of Equation (2.12), with an extra parameter C_2 for the waist position, was used as a fitting function to obtain the beam parameters:

$$y = C_1\sqrt{1+\left((z-C_2)/C_3\right)^2} \tag{7.1}$$

with C_1 the beam waist radius, C_2 the position of the beam waist and C_3 the Rayleigh range.

Each beam radius data point was weighed inversely proportional to its value in order to ensure that the important smaller waist values were not neglected in the least squares calculations. It was further ensured that the waist values govern the least squares method by measuring approximately half of the beam radii within the waist region as advised and stated by the ISO [24]. The waist radius w_0 and Rayleigh range z_0 obtained from the fitted values of fitting function (7.1) were then inserted into Equation (2.23) to obtain the knife-edge M^2-value. Equation (2.23) with the fitted values substituted into it, appears as follows:

$$M_{knife}^{\ 2} = \frac{p C_1^{\ 2}}{l C_3} \tag{7.2}$$

7.8 Application of the theoretical calculations

7.8.1 The proportionality graphs

The knife-edge proportionality graphs of Chapter 6 could serve as a tool to evaluate the measured beams if both the knife-edge and specific proportionality factors of the beams are known (Section 6.4.3.2). Technically, only a complete camera or slit scan is able to determine both. A third alternative is to use the SPSM proportionality factors (Section 4.5.1). The slit profiles described in Section 7.5 were used to obtain the SPSM proportionality factors, which were then plotted versus their respective measured knife-edge M -values, overlaying some of the proportionality graphs of Chapter 6. The results are discussed in the next chapter.

7.8.2 Application of the newly proposed clip-level optimisation method

The clip-level optimisation method of Chapter 6 was applied to the data sets of the measured beams to evaluate the new theory's viability and to demonstrate the technical aspects of implementing it. This was possible because the entire beam energy profile was measured at each z position in both transverse directions. A program was written which incorporated the previous *Matlab* program that was described in Section 7.7. The knife-edge M -value was first calculated with a 16% clip-level. The clip-level was then changed in small steps until the maximum (35%) or minimum (4.16%) clip-levels defined in Section 6.4.4.1 were reached, thereby obtaining the relationship between knife-edge M -values and the clip-values. A polynomial function was then fitted through the data points to determine the 1.732 clip-level. This clip-level was then inserted into Equation (6.8) to obtain a degenerate error free second moment M^2 value. A flowchart for the program is shown in Figure 7-11.

7.9 Summary

The experimental set-up and conditions to characterise an experimental CO_2 TEA laser were examined. This included the laser, scanning hardware, scanning software as well as post-processing and analysing techniques. Methods to employ and evaluate the theory of Chapter 6

were also given. In the next chapter, the data obtained from the measurements will be presented and discussed.

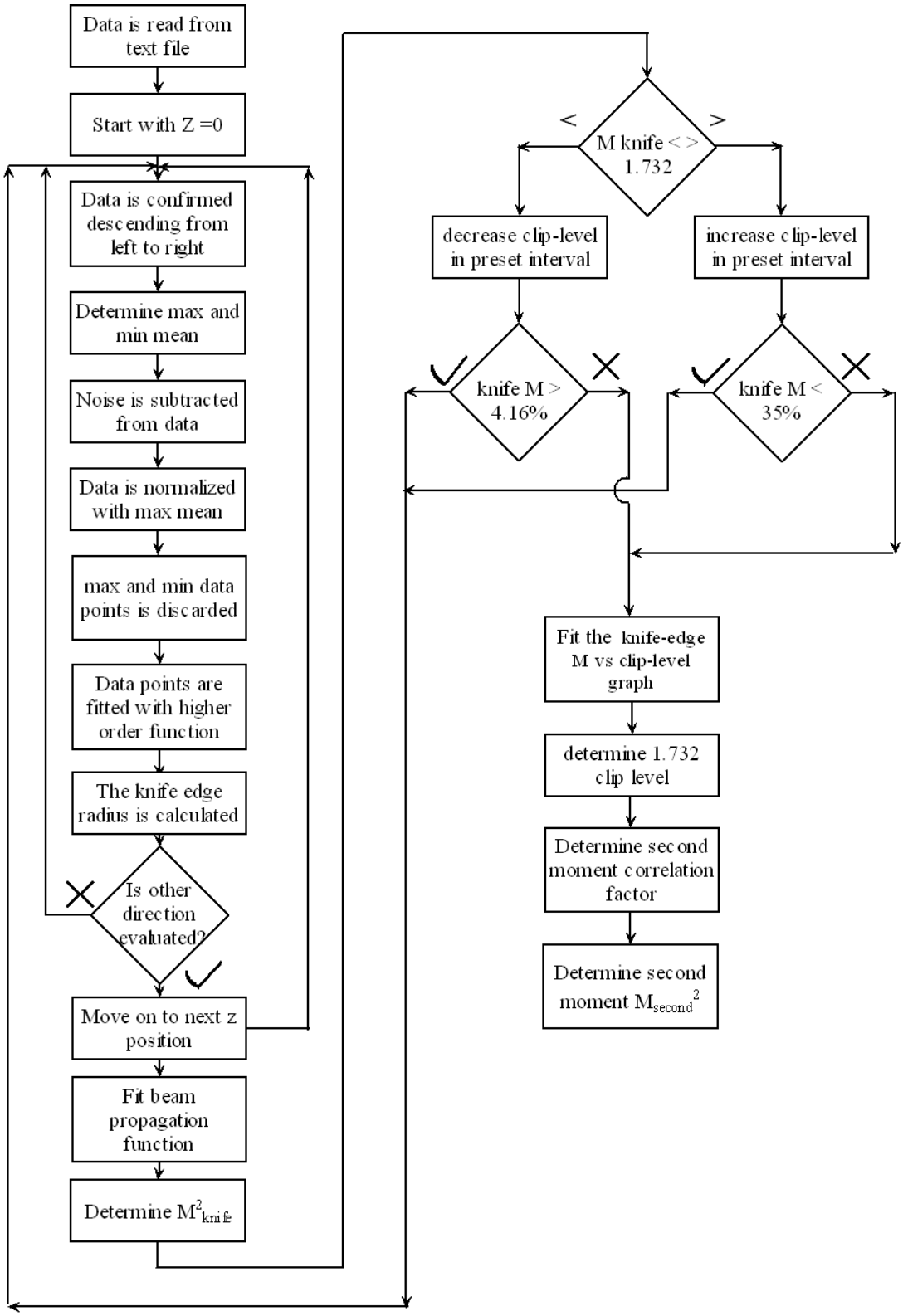

Figure 7-11:Flow chart illustrating the program for the implementation of the clip-level optimisation method.

Chapter 8

Experimental Results

In this chapter, results are presented from slit profiles and knife-edge characterisations of two beams from the CO_2 laser that was described in the Chapter 7. The beams will also be evaluated and correlated with the new and existing correlation theories. An attempt will be made to illustrate that the newly proposed clip-level optimisation method is viable. Results from the various correlation methods will be compared using the SPSM proportionality factors (Section 4.5.1) as reference.

8.1 Slit scan measurements

8.1.1 The multimode beam

The results from the slit scans of the multimode beam in the horizontal and vertical directions (see Section 7.1) can be seen in Figure 8-1 and Figure 8-2 respectively.

The horizontal slit profile has an almost TEM_{00} distribution. This is evident from the good correspondence between the scanned data profile and the fitted TEM_{00} function which only deviates significantly in the wings of the profile. This deviation, in conjunction with two small bulges on the side, reveals that a low percentage of the $TEM_{xy}10$ rectangular mode is present in the beam. The uneven top part of the beam is not due to noise, but is rather the result of slight imperfections on the output coupler.

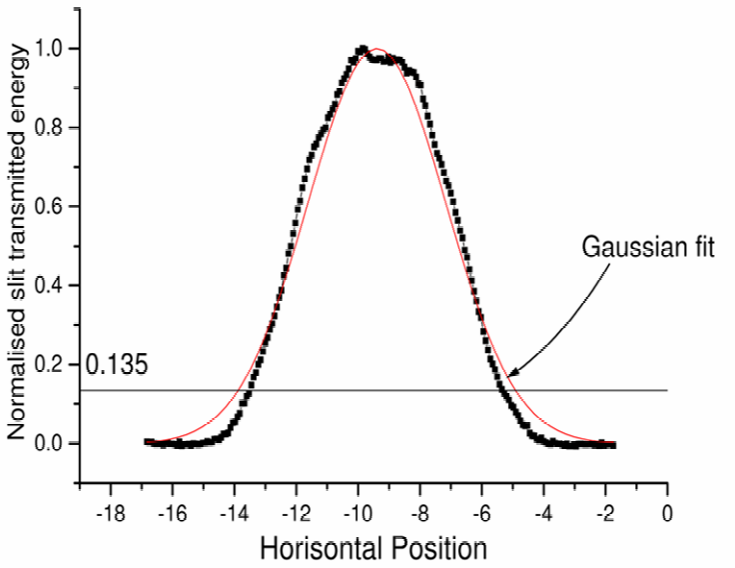

Figure 8-1: Slit profile of the multimode beam in the horizontal direction.

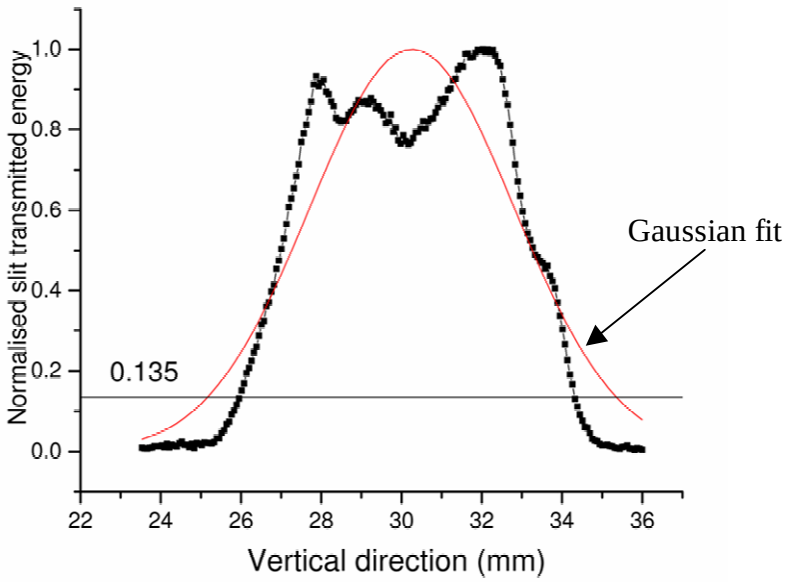

Figure 8-2: Slit profile of the multimode beam in the vertical direction.

The vertical slit profile reveals that the higher order modes dominate in this principle direction so that a relatively high M^2 factor can be expected. This is possibly due to higher gain closer to the electrodes. The vertical slit profile is asymmetrical and contains two local minima and an inflection point. The minima indicate the presence of the $TEM_{xy}02$ rectangular mode while the inflection point either indicates the possible presence of the $TEM_{xy}03$ mode or it can be the result of a slight shift in the centre of the higher order modes to better accommodate defects on the optics. The last is the most probable due to the asymmetrical shape of the vertical slit profile. The number of modes can also be approximated by determining the effective Fresnel number ($N = [a/w_{00}]^2[1/p\sqrt{1-G^2}]$) of the resonator and then using it in loss factor graphs as given in Reference 23. It is however easier to guess the number of modes from the beam energy density distribution due to the damage on the optics.

The two profiles differ considerably, implying that the beam is rectangular symmetric and astigmatic. This rectangular symmetry can be attributed to the flat shape of the electrodes, a non-uniformed gain profile due to pitting on the electrodes as well as defects on the resonator optics.

8.1.2 The near TEM_{00} beam

The slit profiles in the horizontal (transverse to discharge) and vertical directions (in direction of discharge) of the near TEM_{00} beam are given in Figure 8-3 and in Figure 8-4 respectively.

The horizontal slit profile data correspond well with a TEM_{00} fit, except for an inflection point on the left, at low positional values. The aperture radius does not, however, allow for significant oscillation of any higher modes. It was therefore expected that an almost perfect TEM_{00} beam should emanate from the laser, making the inflection point an anomaly. The measured flanks of the data are also significantly lower than those of the fitted TEM_{00} profile so that it would probably have a smaller than theoretically calculated second moment radius.

It is evident from the two elevated flanks of the vertical slit profile that the vertical part of the beam did not have a TEM_{00} distribution as expected, even though the TEM_{00} fit correspond well with the higher data values (energy values transmitted by the slit). The second moment

radius in the vertical direction is expected to be larger than that of the theoretically calculated TEM_{00} beam due to larger than expected energy values in the flanks.

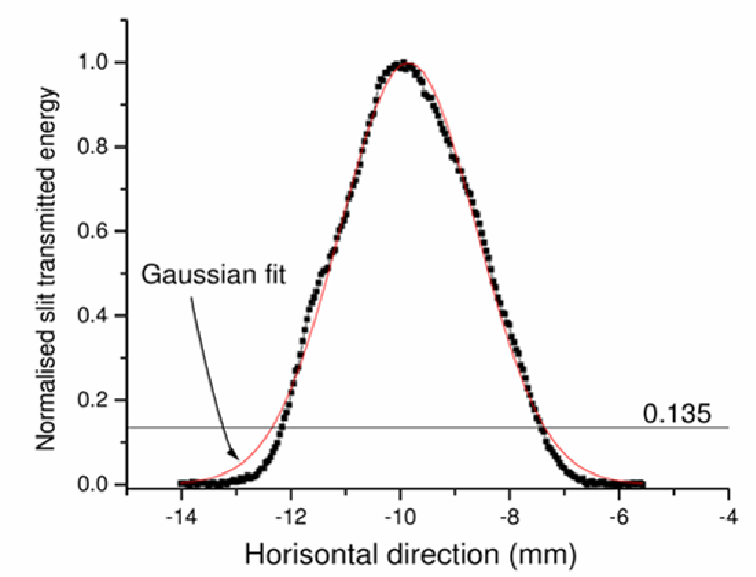

Figure 8-3: Slit profile of the near TEM_{00} in the horizontal direction.

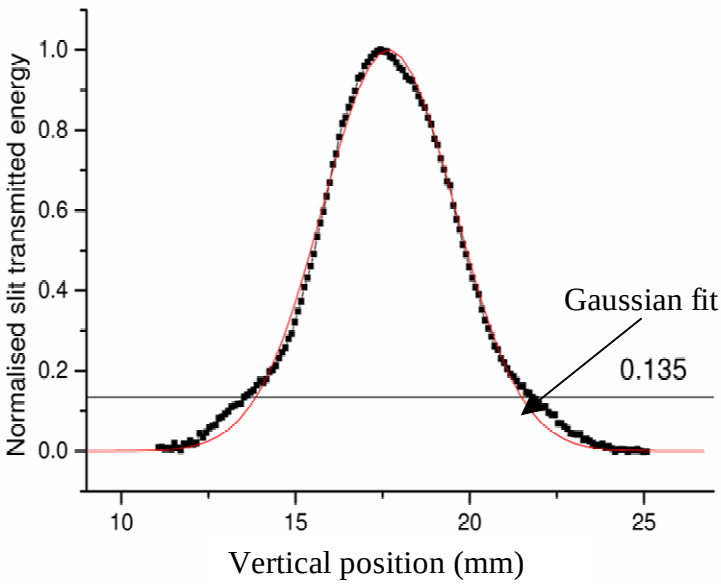

Figure 8-4: Slit profile of the near TEM_{00} in the vertical direction.

The horizontal inflection points and the deviation in the flanks of the two slit profiles suggest that the aperture is causing diffractive effects inside the resonator. Diffractive effects change the basis functions of a resonator so that its electric field distributions can no longer be described by the Hermitian or Laguerre functions. Diffractive effects can usually be avoided by careful adjustment of an iris. This is, however, not possible with the pre-manufactured aperture. This deviation in the flanks is significant and not the cause of a pointing instability which usually only occur in lasers that does not have a hard aperture. The use of a hard aperture is in fact the most common way to get rid of a pointing instability.

The 13.5% energy density radius of both beam profiles correspond well with their respected fitted TEM_{00} Gaussian functions. If the energy density definition of the beam radius is used to determine the M -value (Section 4.3.2) it would not reveal the diffractive effects caused by the internal aperture. For practical purposes, it is therefore judged to be a very good beam to use since it appeared TEM_{00}, except for small deviations in the flanks, which will not have any significant effects in most applications.

The second moment method is extremely sensitive to features in the flanks of the energy density profile. The second moment radius and M-values should therefore differ substantially from those determined by the alternative methods. Theoretically, this beam should therefore be of extremely poor quality

The use of a fixed mounted internal aperture is still an experimental technique. The lack of adjustability and the fact that extremely accurate alignment is crucial makes its beam not the ideal choice to evaluate the theory of Chapter 6. This might also be the case for the multimode beam due to its asymmetrical profile.

8.1.3 Single position slit measured (SPSM) proportionality factors

The vertical part of the multimode beam is used as an example of how a SPSM proportionality factor is obtained from a single slit scan measurement as described in Section 4.5.1 and Section 7.8.1. The vertical slit profile of the multimode beam in Figure **8-5** A was mathematically integrated to produce the knife-edge energy profile seen in Figure 8-5 B. The knife-edge energy profile was fitted with the higher order energy fitting function

(Equation (4.10)). This function was then solved using the 16% and 84% clip-levels to produce the knife-edge radius, which was found to be 4.57. It must once again be stressed that the beam radius is found by solving the fitted function for two clip-levels and not from fitted parameters. The better the functions fits the data the more accurate the beam radius is even though the fit is similar for different beams. The second moment radius was determined to be 4.19 from the slit profile, using Equation (2.4) and the method described in Section 5.2.1.4. The proportionality factor according to Equation (4.26) was therefore just the second moment radius divided by the knife–edge radius resulting in a value of 0.92. Table 8-1 lists the second moment and knife-edge radii as well as the proportionality factors of the two evaluated beams in both principle directions.

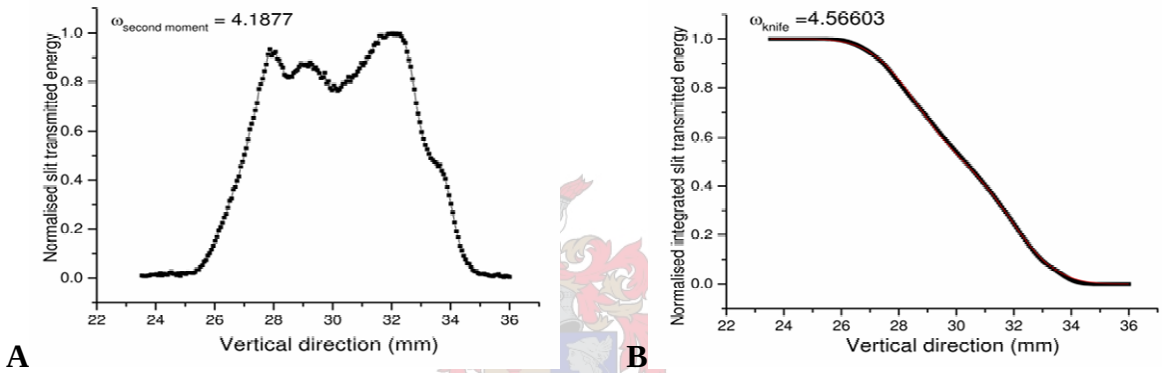

A **B**

Figure 8-5: The multimode beam's vertical slit profile on the left (A) and its mathematically integrated knife-edge energy profile on the right (B).

Beam	Second moment radius	Knife-edge radius	Proportionality factor 16% (measured)
6.5 mm Aperture Horizontal	2.31	2.40	0.96
6.5 mm Aperture Vertical	4.06	3.74	1.09
No aperture Horizontal	3.94	4.14	0.95
No aperture Vertical	4.19	4.57	0.92

Table 8-1: The second moment and knife-edge radii as well as proportionality factors of the two evaluated beams in both principle directions.

8.2 Knife-edge Measurements

8.2.1 Fitting of the energy functions

Figure 8-6 shows the *Matlab* output of a typical knife-edge scan data set. The TEM_{00} energy profile that best fitted these data values is also superimposed on the data set. The data points that were used to fit either the TEM_{00} or $TEM_{x,y}$ 00+01 energy fit functions (Section (4.10)) are encircled. The three data points that were used to determine the average noise can be seen to the right at higher position values. The fifteen unused data points that were recorded to calculate the average maximum energy can be seen to the left at lower position values. Such outputs were generated by the Matlab post-processing program described in Section 7.7 to determine if the correct data points were used and if they were correctly fitted with the TEM_{00} functions. If the $TEM_{x,y}$ 00+01 fitting functions produced comparable beam centres and radii, their fits were also deemed satisfactory.

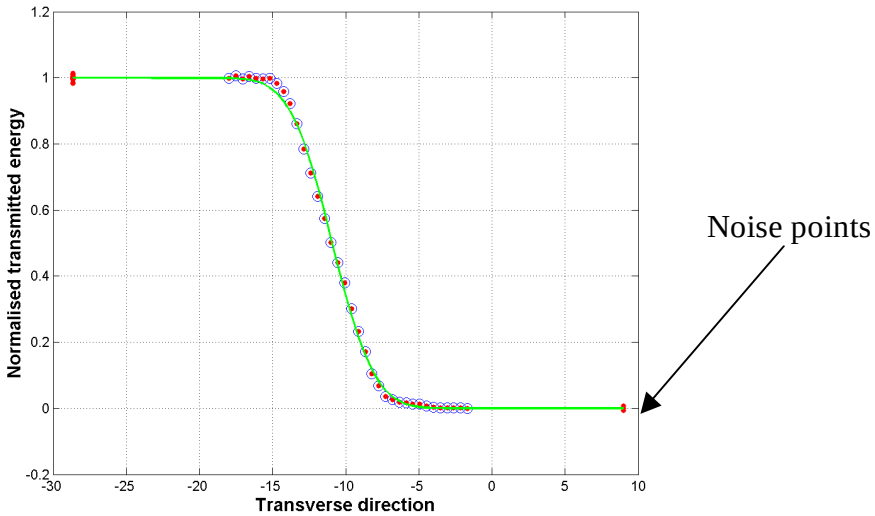

Figure 8-6: Typical output of a Matlab post-processed knife-edge scan fitted with a TEM_{00} function.

Figure 8-7 shows an inflated view of a knife-edge scan fitted with both the TEM_{00} and $TEM_{x,y}$00+01 energy functions. It can be seen that the latter fits the measured knife-edge data significantly better than the plain TEM_{00} function. Errors for low clip levels can typically be in order of 10 to 20% when the TEM_{00} function is fitted. This reduces an order of magnitude to approximately 1 to 2% when the TEM_{xy}00+01 function is fitted. For clip-level optimisation purposes, it is very important that the functions fit the measured data very well. It is therefore essential to use the $TEM_{x,y}$00+01 fitting functions for the clip-level optimisation method.

Knife-edge scans were done in both transverse directions at fifteen positions along the beam propagation direction. The beam radii in both principle directions for each measuring position were then calculated using a 16% clip-level. The propagation of the beams in each transverse direction can be observed by plotting the knife-edge radii versus their respective z positions. Figure 8-8 and Figure 8-9 show the beam propagation profiles (using the knife-edge radii) as well as the slit measured profiles in both principle directions for the two measured beams.

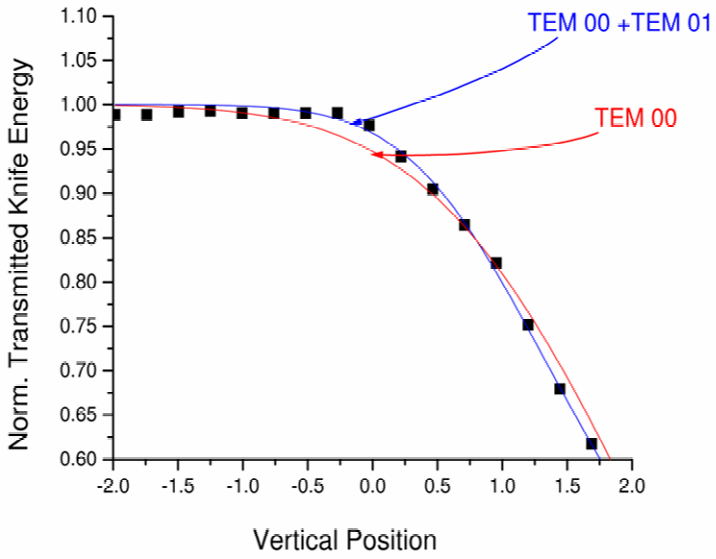

Figure 8-7: Inflated view of a typical knife-edge measured energy profile fitted with both TEM_{00} and a $TEM_{x,y}$ 00+01 fitting functions.

8.2.2 Beam propagation of the multimode beam

It can be seen from Figure 8-8 that the multimode beam is clearly asymmetric in the two principle directions. The vertical scan is only slightly less diverging than the horizontal, but has a significantly larger waist radius indicating that it has a larger M-value. This corresponds well with results from the slit scans which indicated that the vertical energy density profile had more structure due to a larger higher order mode content in that direction.

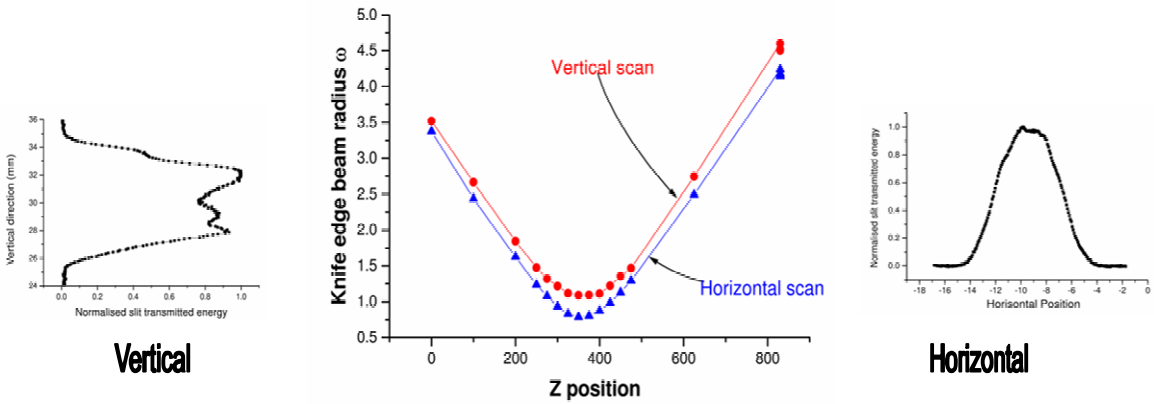

Figure 8-8: Beam propagation and slit profiles of the multimode beam. The vertical energy density profile can be seen to the left and the horizontal to the right.

8.2.3 Beam propagation of the near TEM_{00} beam

From Figure 8-9 it can be seen that the near TEM_{00} beam clearly is symmetrical at the waist. The circularity ratio was measured as 1.13:1 with the knife-edges positioned at a z position of 830 mm. At this position, differences in the radii were found to be more pronounced due to larger divergence of the beam in the vertical direction. The ISO specifies that the ratio should be less than 1.15:1 for a beam to be classified as circular [24]. The beam can therefore be classified as stigmatic.

From the perspective of the practical energy definition, this beam is ideally suited for applications where circular symmetry is required. The large Rayleigh range, circular symmetry and almost TEM_{00} profile makes it suitable for material processing applications such as drilling and cutting of Aluminium and plastics .

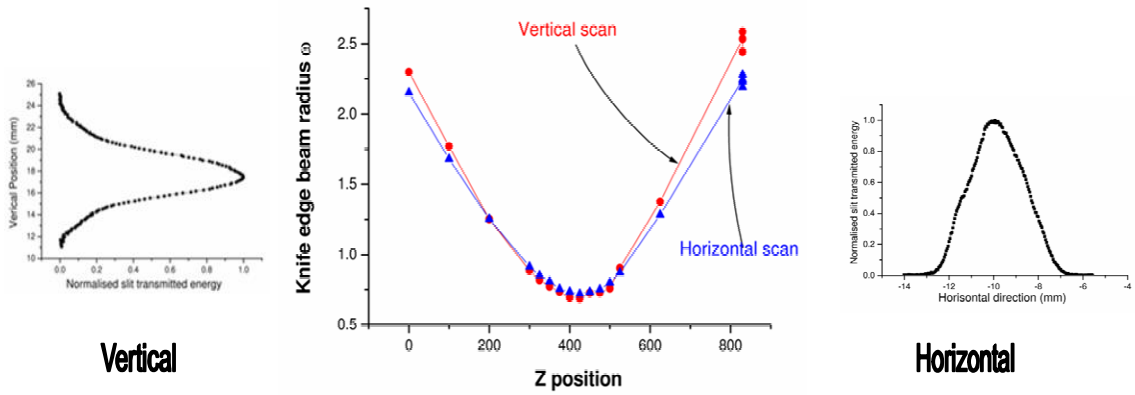

Figure 8-9: Beam propagation and slit scan of the near TEM_{00} beam. The vertical energy density profile can be seen to the left and the horizontal to the right.

8.2.4 Comparison between the propagation of the two beams

The knife-edge (16% clip-level) beam propagation graphs for both beams in the two principle directions are superimposed in

Figure 8-10. The near TEM_{00} beam is clearly less divergent, more symmetrical and focuses to smaller radii than the multimode beam. The two beams also have noticeably different waist positions $z(0)$. Spherical aberration of the focusing lens could be possible explanation for this [32]. This would imply that the multimode beam, which had a larger radius on the lens, focused closer to the lens than the near TEM_{00} beam. It is, however, likely that the effect is caused by aberation effects at the internal aperture.

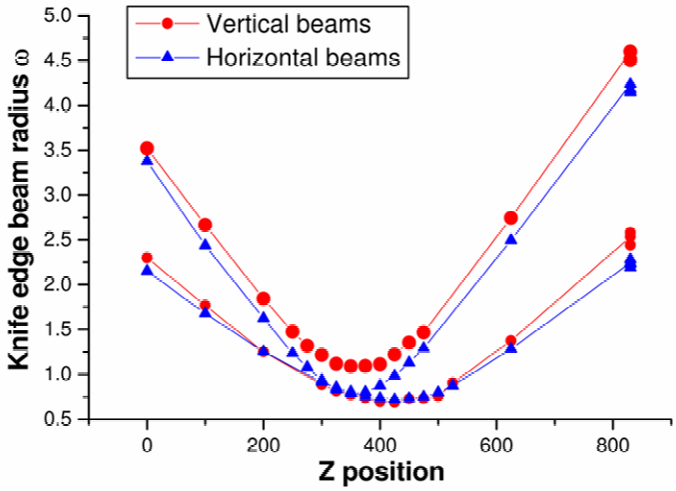

Figure 8-10:Combination graph of the propagation as measured by the knife-edge technique of the near TEM_{00} and multimode beams.

8.2.5 Fitting of the beam propagation equation

The radii of each beam in both principle directions were fitted with the hyperbolic beam propagation function (Equation (2.12)) to determine the knife-edge beam propagation. A typical output from such a fit can be seen in Figure 8-11. The beam radius w_0, Rayleigh Range z_0 and focal position $z(0)$ were then determined as described in Section 7.7. The M^2 values were determined from w_0 and z_0 by means of Equation (7.2).

The *Matlab*-computed values of these properties, the SPSM proportionality factors and correlated second moment M -value are listed in Table 8-2. As expected the M -value s in the two principle directions of the multimode beam differs substantially. No unexpected non-Gaussian behaviour could be noticed from the SPSM proportionality factors of the multimode beam.

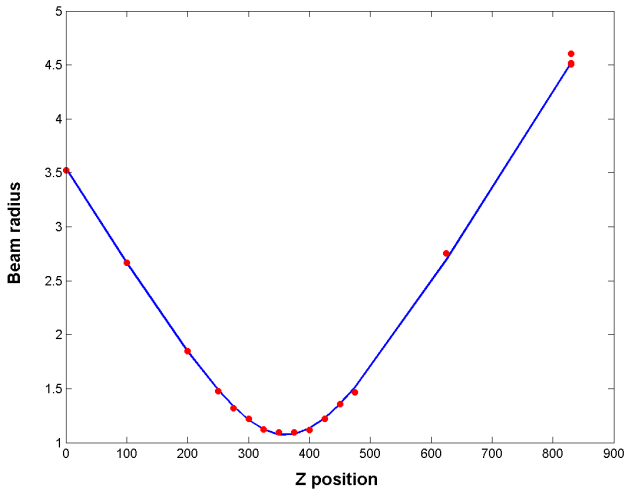

Figure 8-11:Typical fitting of the propagation equation on knife-edge radii versus Z position.

The knife-edge M -values in the two principle directions for the near TEM_{00} beam are almost identical and very close to one. According to the energy definition, the near TEM_{00} beam therefore had very good beam quality. A completely different picture emerges after multiplying these knife-edge M -values with the SPSM proportionality factors. The correlated second moment M -values of the near TEM_{00} beam are found to be much higher in the vertical direction than in the horizontal direction (Table 8-2). In fact, by multiplying with the SPSM proportionality factor, the second moment M -value in the horizontal direction decreases to a value that is less than one. This implies that its M^2 - value also decreases to less than one.

According to Gao and Weber [20] there are three possible explanations that would account for an M -value smaller than one. These are:

- errors in measurement,
- violation of the paraxial approximation,
- errors in calculating M^2.

Pectora roborant cultus recti

Beam	w_0	z_0	$z(0)$	$M_{knife-edge}$ 16%	Proportionality factor 16% (measured)	M_{second}
6.5 mm Aperture Horizontal	0.70	142	415	1.01	0.96	0.97
6.5 mm Aperture Vertical	0.66	124	406	1.02	1.09	1.11
No aperture Horizontal	0.78	89.4	359	1.43	0.95	1.36
No aperture Vertical	1.06	114	362	1.70	0.92	1.56

Table 8-2: The propagation properties of the near TEM_{00} and multimode beams. The SPSM correlated factor and its resulting second moment M-M -value is also given.

The last error is determined to be the cause in this particular case. The SPSM proportionality factor was determined very accurately from a single slit scan. The error on would typically be in order of 1% so that it does not account for this smaller than one value. The laser also had an insignificantly small pointing error (another source for the smaller than one M^2) due to the presence of the hard aperture. The most likely explanation would be that the beam rotated during propagation due to phase changes that are caused by the aperture that was too small (making it general astigmatic). The kurtosis parameter was not measured at different positions along the beam propagation direction (as was already mentioned in Section 7.5.2) so that it could not be verified if this was indeed the case. Using a single proportionality factor from one profile measurement can therefore lead to incorrect results. The only way such beams can be measured correctly is by the complete second moment method ([18] and Section 2.1). It is therefore crucial to establish the kurtosis parameter by measuring the slit profiles at several positions along the beam propagation direction before a scan is performed. For practical energy flux purposes, this rotation is inconsequential since the beam profiles are so similar in both directions. This beam therefore illustrates the limitations of all the correlation theories discussed and developed in the earlier chapters.

8.2.6 The influence of the normalizing energy on the beam radius

The sensitivity of the energy radii to changes in the normalising energy density was calculated using values from the measured horizontal multimode beam. The 100% transmitted normalizing energy was determined using the fifteen allotted maximum energy measuring points as described in Section 7.6. The maximum energy was then changed in fixed percentages while the other measured data values remained unchanged. The beam radius was calculated for each normalisation energy, using the TEM_{00} energy function (Equation (4.9)). The percentage change in radius was calculated and plotted in Figure 8-12 versus the normalisation energy, which is given in a percentage of the original normalising energy. It can be observed that the beam radius is inversely proportional to the full energy. The dependence of the change in beam radius e_{br} on a change of the full energy e_{fe} was measured to be

$$e_{br} = \frac{1}{1.89 e_{fe}} \approx \frac{1}{2 e_{fe}}.$$

Changing the full energy by set percentages therefore changes the beam radius by roughly double that percentage. It was therefore justified to allot fifteen points to the measurement of the full energy value.

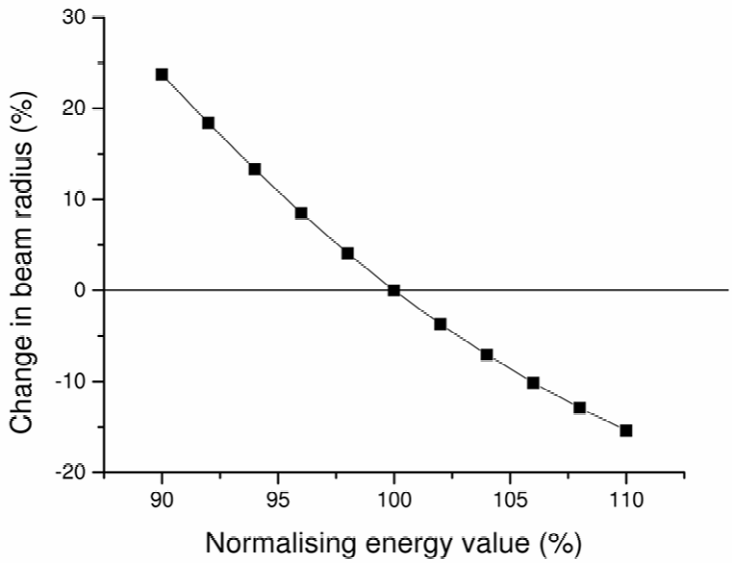

Figure 8-12:The effect a change in the normalizing maximum energy has on the calculated beam radius.

8.3 Evaluation of the beams using the proportionality graphs

It is demonstrated in this section how the proportionality graphs of Chapter 6 can be used as a tool to evaluate laser beams. The proportionality factors of Table 8-2 are plotted as a function of their respective knife-edge M -values and are superimposed on a few of the proportionality graphs. This can be seen in Figure 8-13 for the rectangular two and three-mode subclasses.

It is evident from the graph that the proportionality factor values of the near TEM_{00} beam do not correspond to any of the computed rectangular values. It can be seen from Figure 8-14, which also contains the proportionality graph of the rectangular four-mode subclass, that the vertical proportionality factor for the near TEM_{00} beams is only possible for other high mode content beams (that contain at least four modes). The horizontal proportionality factor for the near TEM_{00} beam is only possible for other beams that contain at least two modes, but having larger knife-edge M -values. Neither of these two conditions applies to the near TEM_{00} beam. The proportionality factors differ widely in the two directions because of the diffraction effects when one expects them to be almost identical. This beam can therefore not be described by Hermitian or Laguerrian functions and cannot be classified as Gaussian (the rectangular three-mode subclass proportionality graph's left lobe contains the proportionality values of the first four cylindrical subclasses (Section 6.4.3.3)). The graphs can therefore be used to assert whether a beam is indeed Gaussian or at the very least, behaves like a Gaussian beam. It is deemed quite possible that the two proportionality factors could have oscillated due to beam rotation as the beam propagated. This possible oscillating behaviour of the proportionality factors can potentially be verified in future.

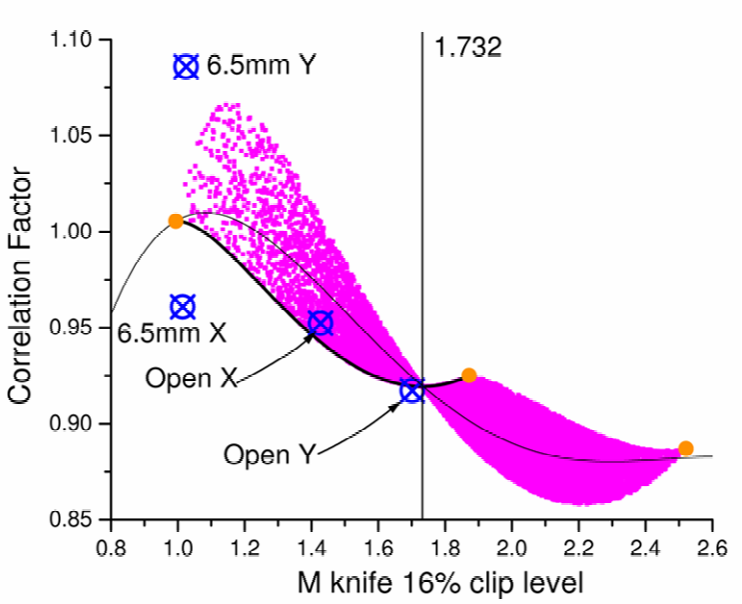

Figure 8-13:SPSM proportionality factors plotted as a function of their respective knife-edge M -values are superimposed on the two and rectangular three-mode subclasses' proportionality graphs.

The proportionality factors of the multimode beam correspond well with the computed values of the proportionality graphs of Figure 8-13. The horizontal proportionality factor indicates that the horizontal part of the beam consists of the fundamental, $TEM_{xy}10$, and a very small percentage of the $TEM_{xy}20$ horizontal modes. It is impossible to make any such assessment for the vertical measurement at this knife-edge clip-level, due to its close proximity to the zero error point. If it is vital to make such an assessment: the clip-level can be changed to move the beam sufficiently far away from the zero error point (Section 6.4.4.1). The high knife-edge M -value in the vertical direction indicates large percentages of the first, second and third rectangular higher order modes. Figure 8-14 shows that it is unlikely that the beam contains any substantial percentage of the fourth higher order mode in both principle directions.

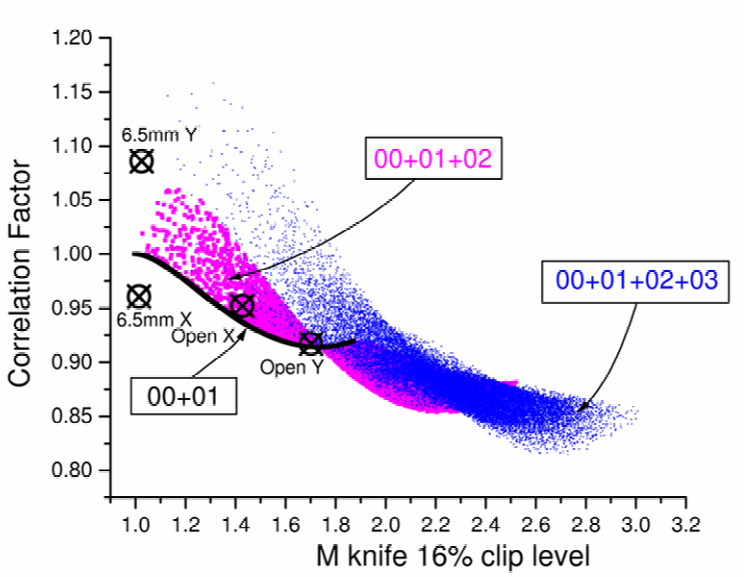

Figure 8-14:Proportionality factors (calculated from slit profiles) plotted versus Knife-edge M -value s superimposed on the cylindrical proportionality graphs (up to the fourth mode) of Chapter 6.

8.4 Application of the clip-level optimisation theory

The clip-level optimisation method is non-intuitive when it is considered that it was developed purely from proportionality graphs, which originated from theoretical energy density profiles. It will be a strong confirmation of the entire proportionality graph theory if the clip-level optimisation method provides good results. This is because the practical clip-level optimisation method utilizes energy (Section 4.4.4) and beam propagation (Section 7.7) fitting functions. Even an indication that this theory corresponds only reasonably with measurements will already indicate that it can be validated in future by additional careful and representative experiments.

The clip-level optimisation method was applied to the two beams in both directions. The knife-edge radii were calculated from the fitted $TEM_{x,y}$ 00+01 functions used previously in the 16% clip-level calculations of the knife-edge M -values. The clip-level was varied in fixed steps and the M -values were calculated as described in Section 7.8.2 by fitting the propagation equation. Figure 8-15 shows the knife-edge M -values as a function of clip-level of the two measured beams. The cross-marked values indicate the 16% clip-level M -values. The clip-levels clearly had to be decreased for all the beams to obtain the zero error knife-edge M -value of 1.732. The graphs in Figure 8-15 were fitted with a third order polynomial

to obtain the exact clip-level that produced a knife-edge M of 1.732 (indicated by the straight line).

The difference between knife-edge M -values in the two transverse directions of the near TEM_{00} beam remains almost constant for all clip-levels. This indicates that the knife-edge method is insensitive to changes or noise in the flanks of laser beams. It is therefore, once again, shown that this beam is very well suited for applications where circular symmetry is required.

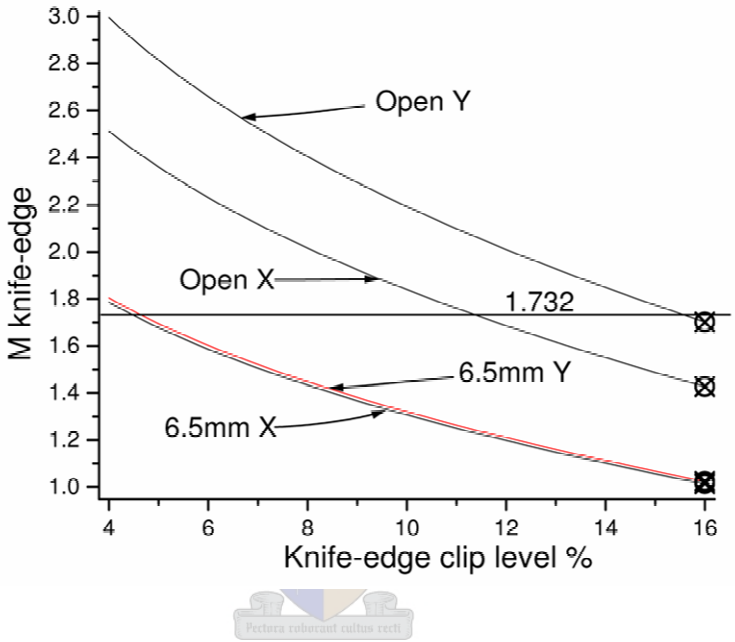

Figure 8-15:Knife-edge M -value as a function of clip-level for the two measured CO_2 laser beams in both principle directions.

A large difference is found in the M -values in the two principle directions of the multimode beam. This difference also remains relatively constant for all clip-levels. This beam is therefore highly asymmetric.

The clip-levels at which each of the graphs cross the 1.732 line are summarized in Table 8-3. The corresponding second moment M -values calculated from Equation (6.8) are also listed. The deviation of the near TEM_{00} clip-level optimisation M -values from the SPSM ones in Table 8-3 indicates that the clip-level theory also does not hold for beams that are affected by diffractive effects. This is because the measuring error of the M -values is typically in the order of 1 to 2 % which do not account for this large differences. The SPSM proportionality values were also very accurately measured.

Beam	1.732 clip-level	Second moment M (1.732)	Second moment M (measured)
Near $TEM_{00}X$	4.47	1.03	0.97
Near $TEM_{00}Y$	4.64	1.04	1.11
Multimode X	11.36	1.38	1.36
Multimode Y	15.55	1.57	1.56

Table 8-3: The 1.732 clip-levels, zero error point correlated second moment M -values and the measured M -value s of the two measured CO_2 laser beams in both principle directions

The M -values determined with the clip-level optimisation method of the multimode beam correspond very well to those of the measured M -values. This indicates that the clip-level optimisation method is viable as an accurate method to correlate the knife-edge and second moment definitions. It is recommended, however, that the method undergo extensive experimental verification by using a wide range of different laser systems.

8.5 Comparison between different knife-edge correlations

Table 8-4 lists the second moment M -values calculated by different knife-edge correlation methods. The SPSM proportionality values are taken as a reference even though they may be susceptible to measuring errors. Deviations from the SPSM-values are therefore taken as errors. Table 8-5 lists the percentage difference (error) between the different correlated M -values and the SPSM correlated values. These errors are also presented graphically in Figure 8-16. The knife-edge correlation methods that are compared are:

- the knife-edge function of the ISO standard (Section 4.5.3),
- the rectangular two-mode fit (Equation (6.2)),
- the rectangular three-mode fit (Equation (6.3)),
- the rectangular four-mode fit (Equation (6.4)),
- the single cylindrical fit (Equation (6.6)), and the
- the clip-level optimisation method described in Section 6.4.4.

The near TEM_{00} beam is deemed non-Gaussian because its SPSM proportionality values do not correspond to those of the computed proportionality values. None of the methods

developed in Chapter 6 could therefore be used to find appropriate proportionality factors for the near TEM_{00} beam. This could also have been anticipated from the extra energy density in flanks of the vertical energy density profile. The theory has nevertheless been applied for the sake of completeness. Large, but expected, errors are therefore found for this beam when all the correlation methods are applied to it.

Beam	M sec (measured)	M knife-edge16 % clip	2mode	3mode	4mode	circ all	ISO	Clip-level optimi-sation
Near $TEM_{00}X$	0.97	1.01	1.02	1.02	1.02	1.01	1.01	1.03
Near $TEM_{00}Y$	1.11	1.02	1.03	1.03	1.04	1.02	1.02	1.04
Multimode X	1.36	1.43	1.35	1.39	1.46	1.37	1.35	1.38
Multimode Y	1.56	1.70	1.56	1.57	1.64	1.57	1.57	1.57

Table 8-4:The second moment M -values calculated by different knife-edge correlation methods.

Beam	2mode	3mode	4mode	circ all	ISO	Clip-level optimi-sation
Near $TEM_{00}X$	4.66	4.85	5.45	4.52	3.93	6.47
Near $TEM_{00}Y$	-7.67	-7.40	-6.55	-7.87	-8.45	-6.11
Multimode X	-0.94	2.09	7.52	0.45	-0.86	1.63
Multimode Y	0.21	0.75	4.81	0.72	0.45	0.71

Table 8-5:The percentage difference between these correlated M -value s and the SPSM second moment M -value s.

The rectangular two-mode, single cylindrical and the ISO correlation functions all correspond very well with measured values. It can therefore not be experimentally shown that the ISO

method produces less accurate correlations than the newly proposed methods. An extensive test is needed to prove or disprove this, involving a large number of diverse beams.

It was already proven in Section 8.3 that none of the beams are part of the rectangular four-mode subclass. The errors using its correlation function are therefore quite high for the beams in both principle directions. A graphical comparison of the remaining correlation methods can therefore be made by expanding the error graph only around the values of the multimode beam and omitting the values for the rectangular four-mode subclass. This can be seen in the insert of Figure 8-16.

The ISO method produces good results because the two knife-edge M -values fall in a region where this method is accurate. At other knife-edge M -values, the ISO method will probably become far less accurate. In the vertical direction, all the remaining methods produce more accurate proportionality factors than in the horizontal direction. This is surprising, given the fact that the energy density profile has visibly poorer quality and is more asymmetrical in this direction. The reason for the overall good correlation of the vertical part is due to its close proximity to the 16% clip-level zero error point.

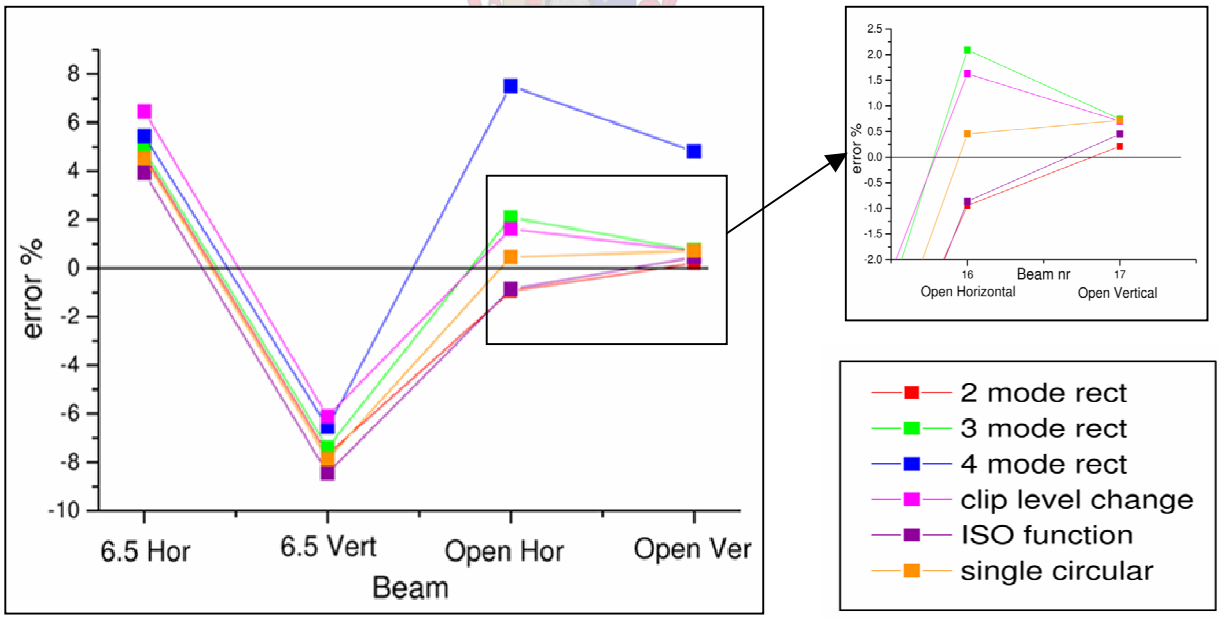

Figure 8-16:A graphical comparison of the correlation methods.

The newly proposed clip-level optimisation method produces results that are consistently accurate in error ranges that are comparable and in some cases even better than those of other

methods. This method, therefore, shows great promise. As mentioned before, these measurements are too small a sample from which to draw conclusions on the relative accuracy of each correlation method.

8.6 Summary

By evaluating a general astigmatic beam, the limits of the theory were shown. The near TEM_{00} beam and the resonator that produced it, although they produced a non-Gaussian diffracted beam, were shown to have practical value for material processing applications. Although the presented results did not indicate a significant improvement over the ISO method, they did indicate that the new theories are viable. The proposed clip-level optimisation theory, in particular, was shown to be practical.

Chapter 9

Summary and future work

In this chapter, conclusions are drawn concerning the three aims set out in Chapter 1. These aims were:

- the development of new correlation theory,
- the modification of a CO_2 TEA laser resonator,
- the design and use of a low frequency beam scanner.

Possible future experimental work and directions to be investigated are also presented.

9.1 Computational results

The computational results provided a means to:

- verify the accuracy of existing methods,
- develop new correlation methods,
- provide a better understanding of energy density of beams,
- evaluate if a beam is Gaussian (not TEM_{00}),
- determine the mode content of a laser beam,
- select the TEM_{00} mode and to
- determine the M^2 factor for certain beams from a single energy density measurement.

It could be seen from the computational results that the ISO correlations are fairly accurate for cylindrical symmetric beams in the alternative M ranges they specify (Section 6.3). The ISO knife-edge correlation functions were found to agree for rectangular symmetric beams at low knife-edge M -values, but deviated substantially for higher M -values (Section 6.3.1).

It was also found that a general one-to-one linear relationship between the second moment and alternative M definitions as assumed by Johnston and the ISO [27], [24] does not exist. Instead, it was illustrated that multiple second moment M -values could exist for a single alternative M -value (Sections 6.1 and 6.2), a fact that was already well documented by Siegman [46]. This degeneracy was found to be larger for rectangular symmetric beams and grew progressively worse as the number of modes in the beams was increased.

The theoretical knife-edge degenerate errors reach unacceptably high values for rectangular symmetric beams containing more than three modes (Section 6.4.1). Correlating them with any function was found to produce highly inaccurate results. These large degenerate errors can also seriously affect the reproducibility of experiments in which high mode-content beams are used (Section 6.4.5.3).

New correlation methods were developed, taking into account the degeneracy as well as the deviation of the second moment values from a single linear function for both the knife-edge and slit methods (Section 6.4). These correlation methods are comprehensive since they incorporate techniques of both the ISO and Siegman. The ISO's method only uses a few modelled cylindrical energy density profiles based on real laser beams [27]. The new methods incorporate much larger numbers of practical beams. Siegman [46] used pure Hermitian modes and an optimum clip-level in his correlation method. The new methods incorporate pure modes and in one case employ a clip-level optimisation method to obtain an optimal proportionality factor (Section 6.4.3.3). The new methods are therefore improvements on both the ISO's and Siegman's methods.

A problem with most of the new knife-edge correlation methods, when used for rectangular symmetric beams, is that the number of modes in the laser had to be known to give accurate results. Knife-edge correlation was also found to be accurate only for rectangular symmetric beams containing three modes or less, due to large degenerate errors (as shown in Section 6.4.5.3).

A new clip-level optimisation method is proposed that correlates the knife-edge with the second moment definitions theoretically without introducing any degenerate errors (Section 6.4.3.3). This theory is valid for beams belonging to subclasses consisting of up to three rectangular and four cylindrical symmetric modes. This new clip-level optimisation

theory was shown to be best suited for high frequency scanners because they measure accurate energy profiles. It was demonstrated that the clip-level optimisation method can also be used for low frequency pulsed laser systems, but requires longer measurements and more post-processing to give accurate results (also see Appendix F).

A comparison between the knife-edge and slit proportionality graphs demonstrated that the knife-edge method is better suited for correlation purposes (Section 6.5). This is due to lower degenerate errors for both rectangular and cylindrical symmetric beams, a more linear relationship between the second moment and the knife-edge M -values and the existence of a useable zero error point for a few important subclasses.

9.2 The laser

Optical degradation and discharge instability were encountered during the operation of the experimental CO_2 TEA laser. The single cause of both of these problems was eventually found to be the steel pre-ionisation pins, which left an iron oxide residue within the laser (Section 7.1). The investigative work, which led to this discovery and the measures that were taken to fix it, provided valuable experience in the field of gas lasers and resonators. The most notable was the development of an experimental fixed internal aperture.

The near TEM_{00} laser beam from the fixed internal aperture was shown to be highly suitable for use in material processing since it provided excellent beam quality from an energy content perspective (Section 8.1.2 and 8.2.3). This indicates that internal aperture resonators can be used to make gas lasers less expensive and more rugged. However, a quality assessment of the near TEM_{00} beam indicated that it was far from ideal due to diffractive effects (Section 8.3). More development work will therefore be necessary. This type of internal aperture resonator is, therefore, not yet marketable. The near TEM_{00} beam was later used in preliminary laser generated plasma experiments [1], [11] due to its good energy qualities.

9.3 Beam scanner

The beam scanner developed during the project performed sufficiently accurate knife-edge scans of the experimental laser beams (Section 8.2). These scans could be used in practical experiments and for a feasibility study of the clip-level optimisation method. This scanner can

be used on other low frequency pulsed laser systems in the department like Nd:YAG, eximer and dye lasers. Valuable experience was gained in the development of the scanner and accompanying automation and post-processing software (Sections 7.3 and 7.4). The only real drawback of the scanner is its slow scanning speed.

9.4 Proposed future work

The ISO specified that at least half the radii measuring points in the beam propagation direction should be within the waist area and the other half should be distributed beyond two Rayleigh range lengths from the beam waist position $z(0)$ [24]. This ratio has not been proven (Section 4.1). Calculations to determine the optimal ratio of measuring points in these two regions for maximum accuracy remain to be done.

The validity of the proportionality graphs over a wide range of laser systems remains unproven (Section 6.6). It is especially important to test this for solid-state lasers, which are currently at the forefront of laser development. It is suggested that this be proven using a fast CCD camera where the second moment, slit and knife-edge radii can easily be obtained from the two-dimensional energy density distributions (Section 4.2.1). New noise deduction techniques make it possible to determine the second moment radii much more accurately than in the past [48]. Large numbers of sample beams can easily be obtained if a pulsed CO_2 TEA laser (Section 7.1) and a fast camera or linear diode array (rise time <1ns) are used for initial measurements since different temporal parts of the pulses can have different mode combinations [15], [16], [17], [31]. Different parts of the pulse can then be analysed as independent beams. The superiority of the new correlation methods over the ISO correlation functions also awaits further testing and approval (Section 8.5).

The possible oscillating behaviour of the proportionality factors of general astigmatic beams could also be examined in camera verification experiments (Section 8.3). It still needs to be investigated whether the proportionality factors can be incorporated into camera software (Section 6.4.3.2) to test for Gaussian behaviour and to select the TEM_{00} mode.

The applicability of the computational results in other parts of physics are open to investigation since the Laguerre basis functions for cylindrical symmetric beams are also found in the electron probability distributions of atomic physics. The rectangular Hermitian

functions are found in the probability distributions of the simple quantum harmonic oscillator [22]. It is therefore quite possible that these results will be useful to describe other phenomena as well.

A new position and diameter adjustable internal aperture for the CO_2 TEA laser is already in the design phase. It is currently being investigated whether this aperture unit can be combined with a SF_6 cell to make the laser wavelength interchangeable between 10.6 and 9.6 mm [51] and to possibly mode lock the laser [47]. The slit profiles of beams emanating from this resonator will be measured at several positions to ensure that no diffractive effects occur inside the resonator. To further prevent this possibility, the setup of this resonator will be done with the rectangular two-mode proportionality graph described earlier (Section 6.4.1). The resulting beam (or beams) can then be used to complete the laser generated plasma experiments.

Chapter 10

Appendices

10.1 Appendix A

Knife–edge analytically integrated functions of the rectangular Hermitian modes up to $TEM_{xy}05$

All the knife-edge energy functions of the pure modes that are listed below were obtained by integrating the energy density functions of Equation (3.19) with Equation (4.5) in the mathematical program Mathematica.

TEM_{00}

$$E_{\text{knife}}\left(\frac{x}{w}\right)=\frac{1}{2}\left(erf\left(\frac{-x\sqrt{2}}{w(z)}\right)+1\right)$$

$TEM_{xy}01$

$$E_{\text{knife}}\left(\frac{x}{w}\right)=\frac{1}{2}\left(erf\left(\frac{-\sqrt{2}(x)}{w}\right)+1\right)+\sqrt{\frac{2}{p}}e^{-2\left(\frac{x}{w}\right)^2}\left(\frac{x}{w}\right)$$

$TEM_{xy}02$

$$E_{\text{knife}}\left(\frac{x}{w}\right)=\frac{1}{2}\left(erf\left(\frac{-\sqrt{2}(x)}{w}\right)+1\right)+\frac{1}{4\sqrt{2p}}e^{-2\left(\frac{x}{w}\right)^2}\left(4\left(\frac{x}{w}\right)+16\left(\frac{x}{w}\right)^3\right)$$

$\mathrm{TEM}_{xy}03$

$$E_{\text{knife}}\left(\frac{x}{w}\right)=\frac{1}{2}\left(erf\left(\frac{-\sqrt{2}(x)}{w}\right)+1\right)+\frac{1}{6\sqrt{2p}}e^{-2\left(\frac{x}{w}\right)^2}\left(12\left(\frac{x}{w}\right)-8\left(\frac{x}{w}\right)^3+32\left(\frac{x}{w}\right)^5\right)$$

$\mathrm{TEM}_{xy}04$

$$E_{\text{knife}}\left(\frac{x}{w}\right)=\frac{1}{2}\left(erf\left(\frac{-\sqrt{2}(x)}{w}\right)+1\right)+\frac{1}{12\sqrt{2p}}e^{-2\left(\frac{x}{w}\right)^2}\left(15\left(\frac{x}{w}\right)-68\left(\frac{x}{w}\right)^3+80\left(\frac{x}{w}\right)^5+64\left(\frac{x}{w}\right)^7\right)$$

$\mathrm{TEM}_{xy}05$

$$E_{\text{knife}}\left(\frac{x}{w}\right)=\frac{1}{2}\left(erf\left(\frac{-\sqrt{2}(x)}{w}\right)+1\right)+\frac{1}{30\sqrt{2p}}e^{-2\left(\frac{x}{w}\right)^2}\left(\begin{array}{l}60\left(\frac{x}{w}\right)-70\left(\frac{x}{w}\right)^3+424\left(\frac{x}{w}\right)^5-325\left(\frac{x}{w}\right)^7\\+128\left(\frac{x}{w}\right)^9\end{array}\right)$$

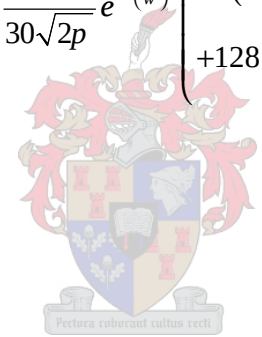

The preceding energy functions were plotted (right) versus their source energy density profiles (left).

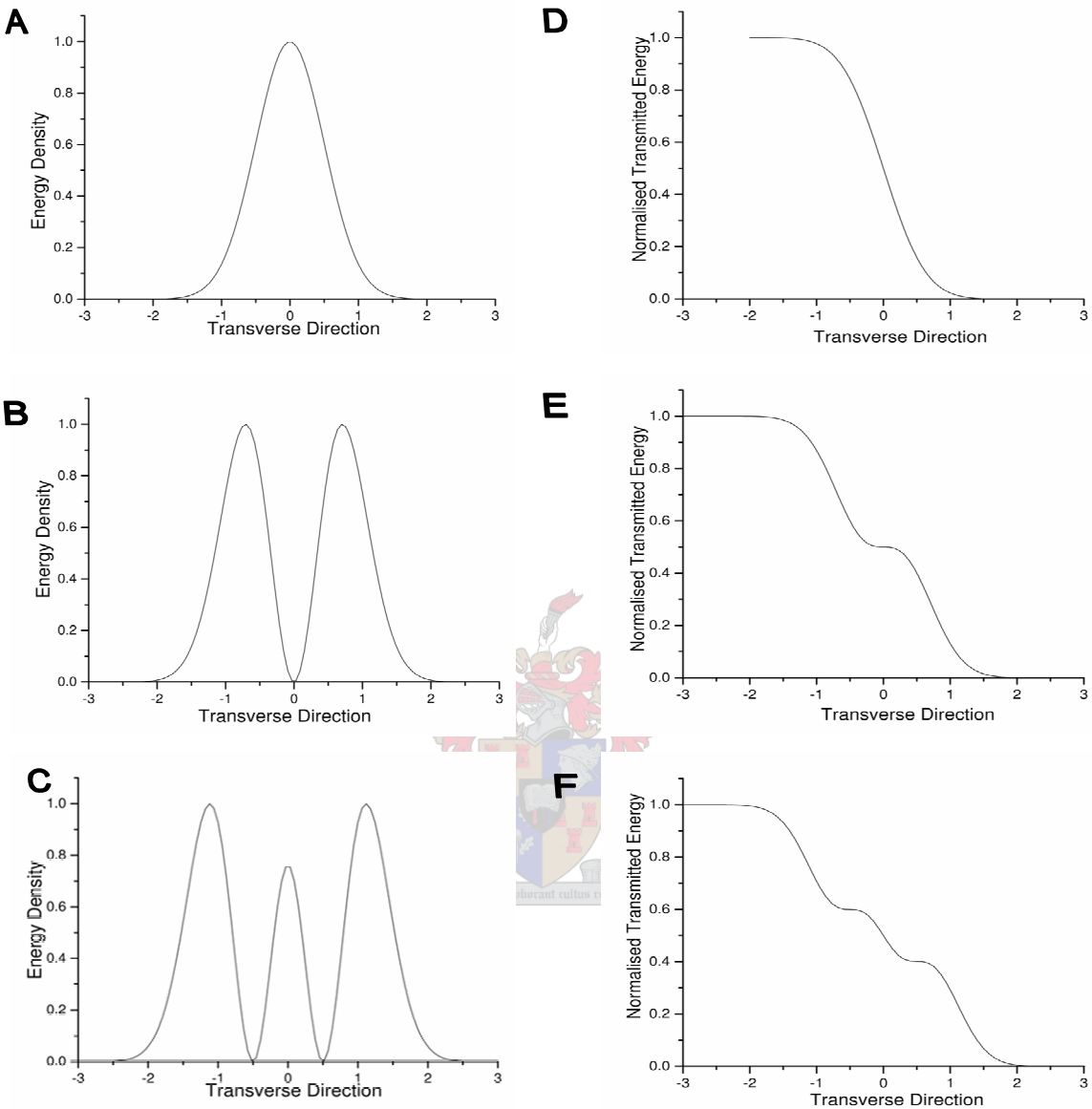

Figure 10-1:Energy density graphs of pure rectangular modes TEM_{00} to $TEM_{xy}02$ (A-C) plotted alongside their respective knife-edge integrated energy graphs (D-F).

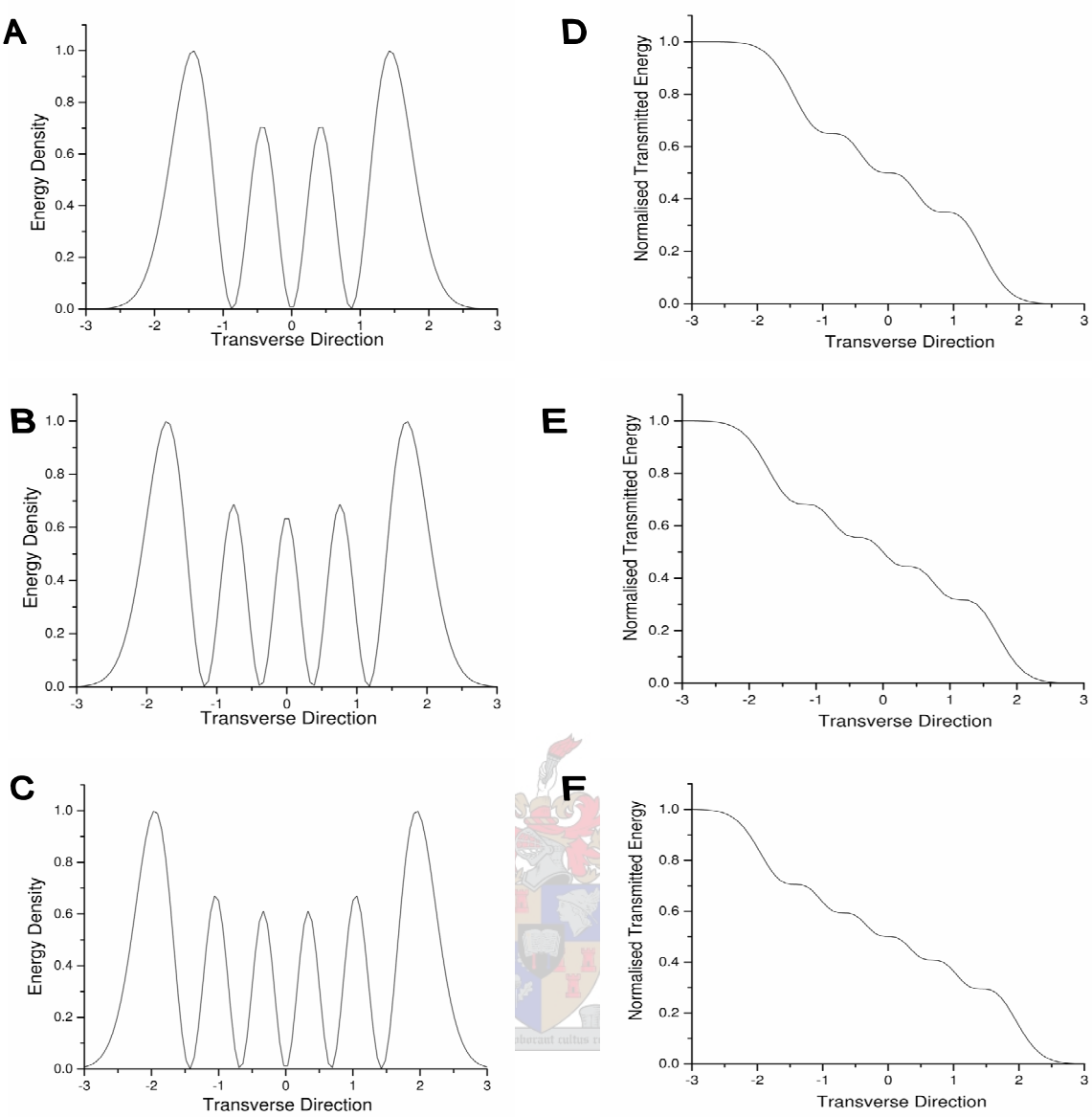

Figure 10-2:Energy density graphs of pure rectangular modes $TEM_{xy}03$ to $TEM_{xy}05$ (left from top to bottom) plotted alongside their respective knife-edge integrated energy graphs (right).

10.2 Appendix B

Example of two-dimensional value matrices in *Excel*

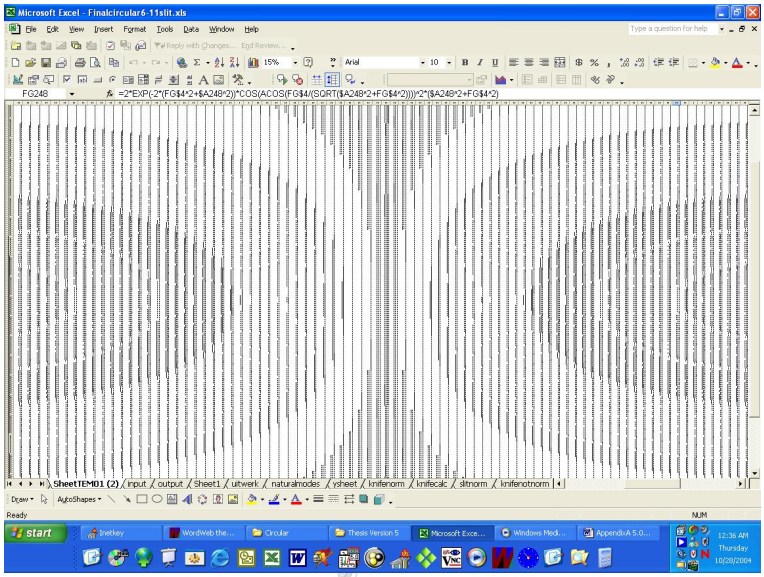

Figure 10-3:The two-dimensional value matrix of the normal $TEM_{pl}01$ mode.

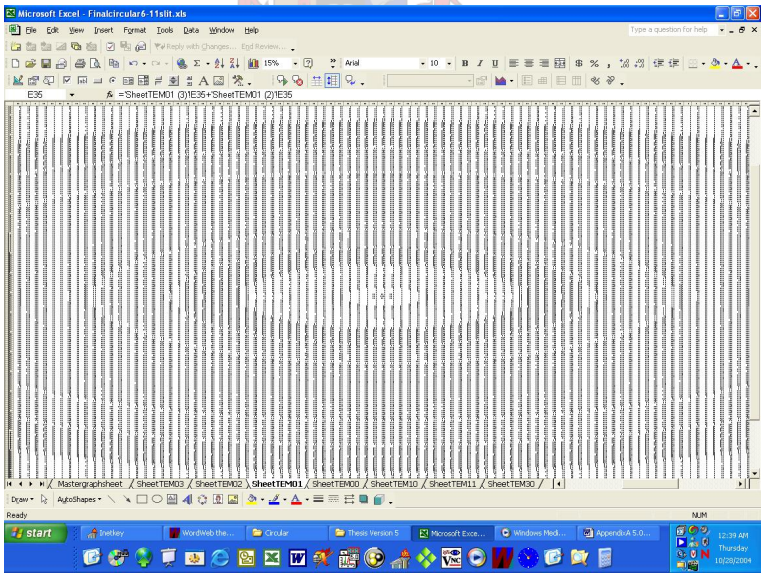

Figure 10-4:The two-dimensional value matrix of the doughnut (B) $TEM_{pl}01$ mode.

10.3 Appendix C

Graphical proof of the separability of the rectangular modes

In Figure 10-5 two different rectangular modes $TEM_{xy}11$ and $TEM_{xy}12$ are both slit scanned in the direction of the arrow (x direction). Both slit profiles are normalised and plotted overlaying the profiles obtained by setting the other directions values equal to zero (a one-dimensional pinhole profile). All the graphs in the bottom figure are clearly indistinguishable from each other. They are also indistinguishable from the one-dimensional pinhole profile of $TEM_{xy}10$. The generation of two-dimensional energy density distributions is therefore unnecessary due to the Cartesian separability of the Hermitian functions.

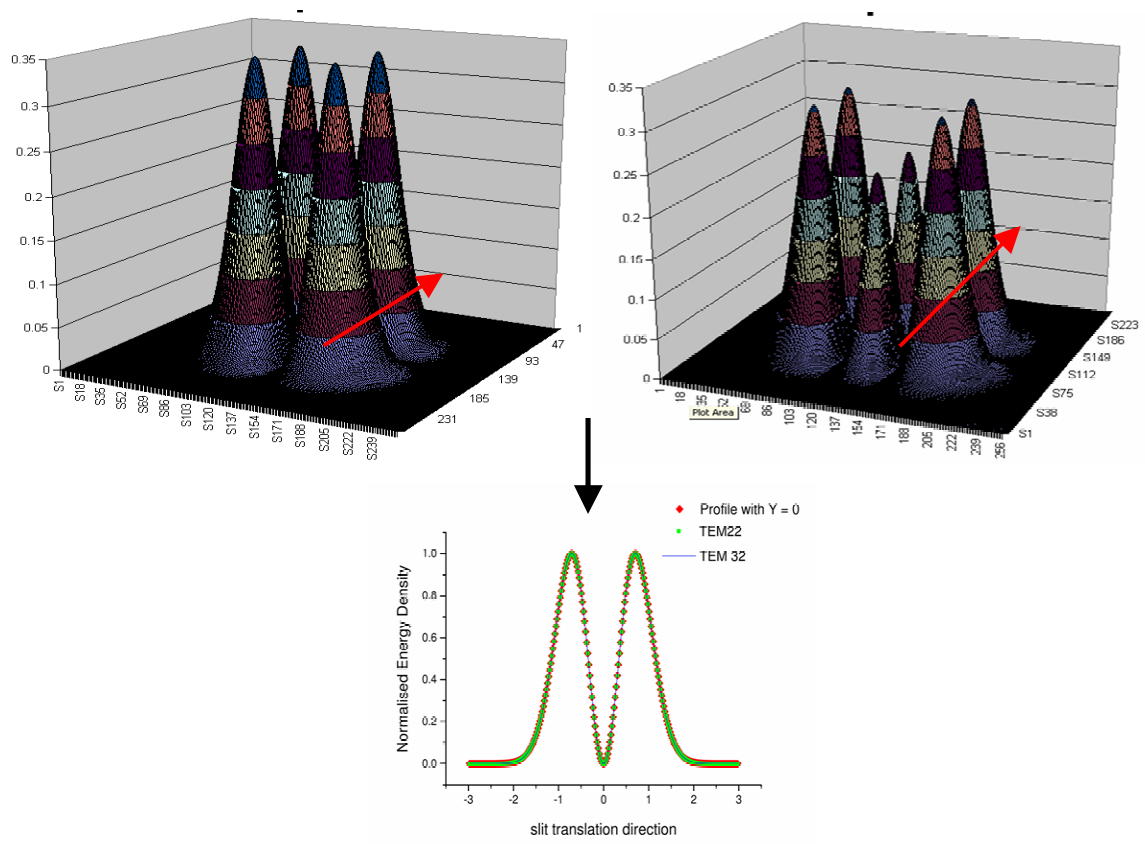

Figure 10-5:Slit addition of two different two-dimensional rectangular modes ($TEM_{xy}11$ and $TEM_{xy}12$) in the direction of the arrow (x) producing the exact same slit profile which is identical to the one-dimensional pinhole profile of $TEM_{xy}10$ illustrating the Hermitian separability in the Cartesian directions.

10.4 Appendix D

Newly proposed correlation functions

The general fifth order polynomial that was fitted through the knife-edge proportionality graphs was:

$$M_{knife} \times (+1.00557 - a(M_{knife} - 0.994458) + b(M_{knife} - 0.994458)^2 + c(M_{knife} - 0.994458)^3 + d(M_{knife} - 0.994458)^4 + e(M_{knife} - 0.994458)^5) \quad \text{(D.1)}$$

The general fifth order polynomial that was fitted through the slit proportionality graphs was:

$$M_{knife} \times (+0.9994 - a(M_{knife} - 1.000619) + b(M_{knife} - 1.000619)^2 + c(M_{knife} - 1.000619)^3 + d(M_{knife} - 1.000619)^4 + e(M_{knife} - 1.000619)^5) \quad \text{(D.2)}$$

The following correlation factors should be inserted into the corresponding functions D1 and D2 to obtain the correlation functions.

Beam subclass	**a**	**b**	**c**	**d**	**e**	**Range** Knife-edge M
TEM_{xy} 00+01	-0.01312	-0.79973	+1.63888	-1.3571	+0.46948	M>0.9946 M<1.8724
TEM_{xy} 00+01+02	+0.1004	-0.64557	+0.62304	-0.21434	+0.02117	M>0.9946 M<2.5211
TEM_{xy} 00+01+02+03	+0.48487	-1.60911	1.64479	-0.74665	+0.12859	M>0.9946 M<3.0600
TEM_{xy} 00+01+02+03+04	+0.30742	-0.67211	+0.41293	-0.10735	+0.01023	M>0.9946 M<3.5310

Table 10-1:Newly proposed knife-edge correlation factors (which must be inserted into Equation (D.1) for the first four rectangular mode subclasses.

Beam subclass	**a**	**b**	**c**	**d**	**e**	**Range** Knife-edge M
TEM_{pl} 00+01	-0.12712	+0.40283	-3.27354	+7.45889	-5.36761	M>0.9946 M<1.53
TEM_{pl} 00+01 +02	+0.21395	-2.21383	+5.28299	-5.4693	+2.09481	M>0.9946 M<1.92
TEM_{pl} 00+01+ 02+10	0.39839	-2.6454	+5.1731	-4.56367	+1.52275	M>0.9946 M<1.99
TEM_{pl} 00+01+ 02+10+03	+0.47011	-2.75246	+4.89901	-3.86241	+1.13883	M>0.9946 M<2.26

Table 10-2:Newly proposed knife-edge correlation factors (which must be inserted into Equation (D.1) for the first four cylindrical mode subclasses.

Beam subclass	**a**	**b**	**c**	**d**	**e**	**Range** Knife-edge M
TEM_{xy} 00+01	+0.1441	-4.2175	28.122	-80.3660	84.388	M>1.00062 M<1.50140
TEM_{xy} 00+01+ 02	+0.543	-5.9171	+20.296	-28.3914	+14.351	M>1.00062 M<1.84337
TEM_{xy} 00+01+ 02+03	+1.20063	-7.958	+18.296	-17.776	+6.291	M>1.00062 M<2.12269
TEM_{xy} 00+01+ 02+03+04	2.023	-9.410	+15.941	-11.754	+3.214	M>1.00062 M<2.3652

Table 10-3:Newly proposed slit correlation factors (which must be inserted into Equation (D.2) for the first four rectangular mode subclasses.

Beam subclass	**a**	**b**	**c**	**d**	**e**	**Range** Knife-edge M
TEM_{pl} 00+01	0.03260	-2.3346	+17.110	-54.0110	+62.210	M>0.9946 M<1.42
TEM_{pl} 00+01 +02	+0.2560	-3.295	+11.766	-17.766	+10.099	M>0.9946 M<1.68
TEM_{pl} 00+01+ 02+10	0.3175	-3.0343	+8.8195	-11.1603	+5.5281	M>0.9946 M<1.68
TEM_{pl} 00+01+ 02+10+03	+0.2285	-2.1249	+5.6743	-6.4392	+2.7952	M>0.9946 M<1.88

Table 10-4:Newly proposed slit correlation factors (which must be inserted into Equation (D.2) for the first four cylindrical mode subclasses.

10.5 Appendix E

Clip-level optimisation graphs

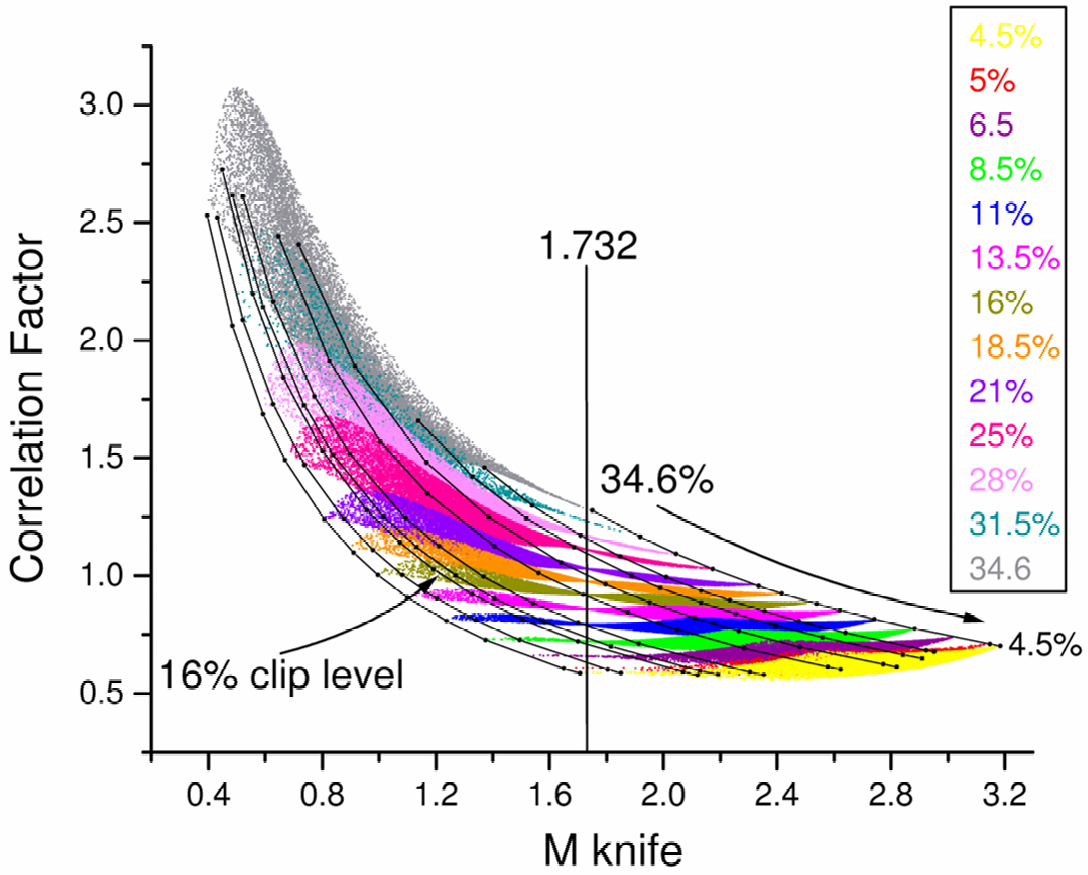

Figure 10-6:Knife-edge proportionality factor graphs for the rectangular three-mode subclass calculated using different clip-levels.

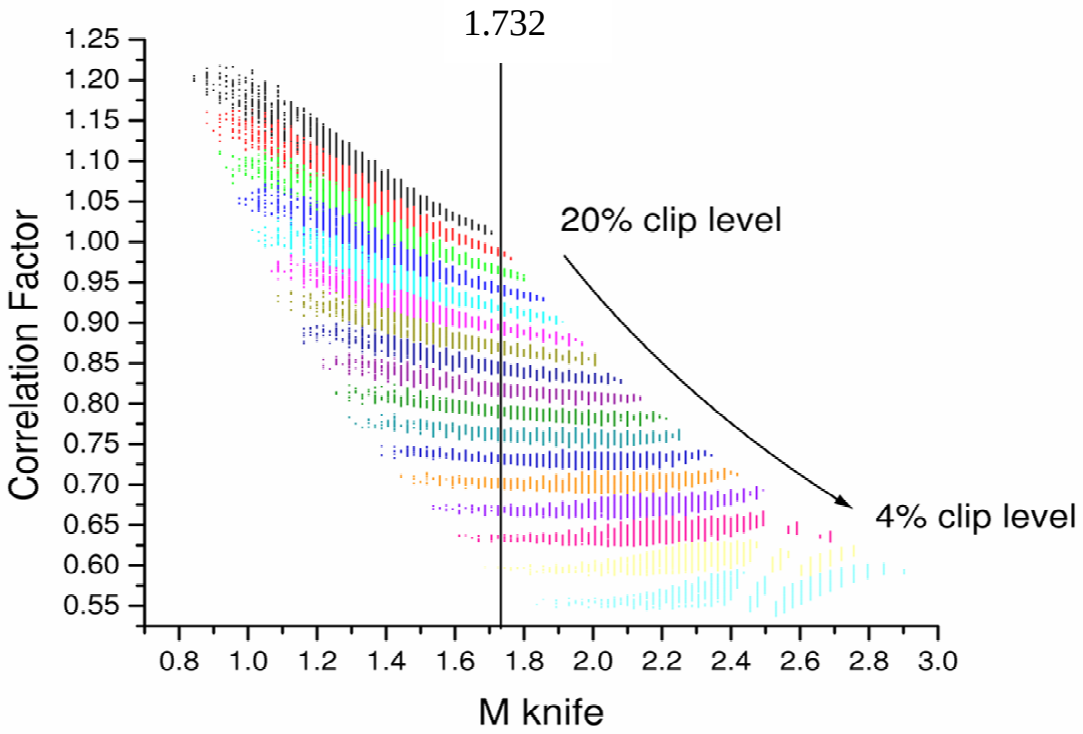

Figure 10-7:Knife-edge proportionality factor graphs for the cylindrical three-mode subclass ($TEM_{pl}00+01+02$) calculated using different clip-levels.

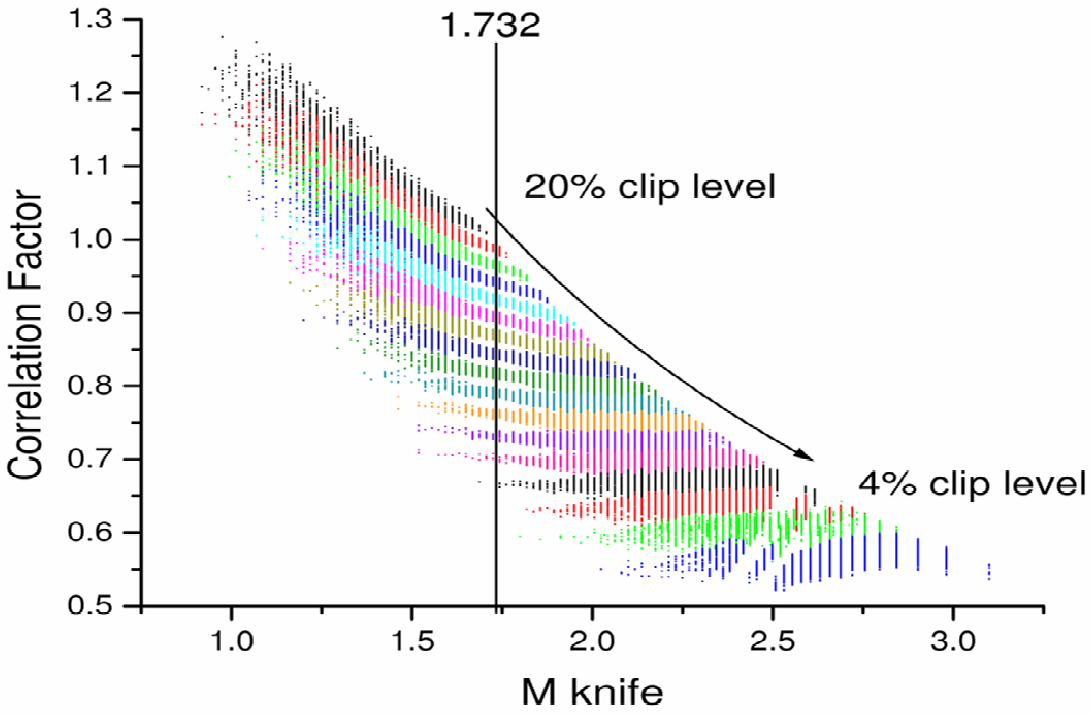

Figure 10-8:Knife-edge proportionality factor graphs for the cylindrical four-mode subclass ($TEM_{pl}00+01+02+10$) calculated using different clip-levels.

10.6 Appendix F

Below measuring error correlation functions

This clip-level optimisation method can be used for rectangular symmetric pulsed lasers and for hand scanning techniques involving rectangular symmetric lasers.

The proportionality factors with knife-edge M -values close to 1.732 can also be used since their degenerate errors are much lower than the measuring error. Set given clip-levels with known correlation functions, which were fitted only close to the zero error point, are used to determine the second moment M^2 value. Such a fitting is illustrated in Figure 10-9.

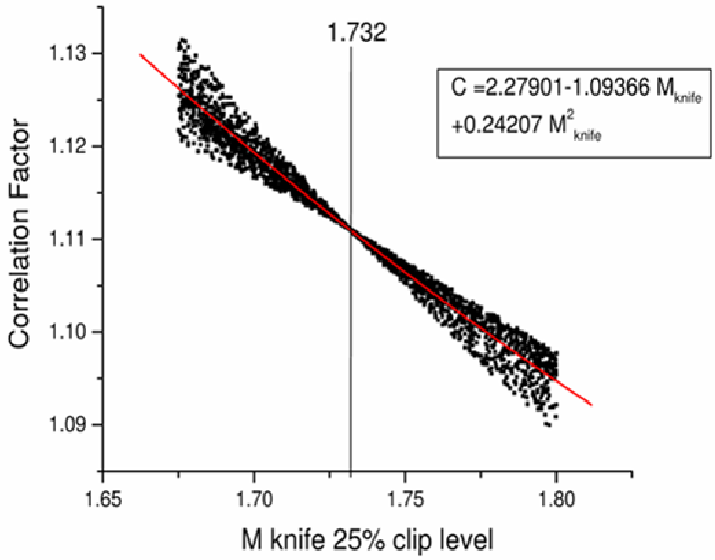

Figure 10-9:Fitting of the correlation function close to the zero error point of the rectangular three-mode subclass using a 25% clip-level.

The "below measuring error" proportionality factor can be determined as follows.

- The 16% knife-edge M -value is measured.
- The user choose a certain given clip-level value that will give knife-edge M -value closer to 1.732.
- This process is repeated until the clip-level is determined that gives a knife-edge M -value that is the closest to 1.732.

- The correlation function given in Table 10-5 for that specific clip-level is used to obtain the "below measuring error" second moment M -value.

4.5	$M_{\text{sec},4.5\%} = M_{knife} \times 0.58983$
5	$M_{\text{sec},5\%} = M_{knife} \times 0.60899$
6.5	$M_{\text{sec},6.5\%} = M_{knife} \times (0.69777 - 0.02236\, M_{knife})$
8.5	$M_{\text{sec},8.5\%} = M_{knife} \times (0.90067 - 0.15875\, M_{knife} + 0.03201\, M_{knife}^2)$
11	$M_{\text{sec},11\%} = M_{knife} \times (1.39809 - 0.63865\, M_{knife} + 0.16707\, M_{knife}^2)$
13.5	$M_{\text{sec},13.5\%} = M_{knife} \times (1.03149 - 0.11663\, M_{knife} + 0.00971\, M_{knife}^2)$
16	$M_{\text{sec},16\%} = M_{knife} \times (1.3607 - 0.38634\, M_{knife} + 0.07593\, M_{knife}^2)$
18	$M_{\text{sec},18\%} = M_{knife} \times (1.39281 - 0.31758\, M_{knife} + 0.04453\, M_{knife}^2)$
21	$M_{\text{sec},21\%} = M_{knife} \times (1.85884 - 0.75621\, M_{knife} + 0.16039\, M_{knife}^2)$
25	$M_{\text{sec},25\%} = M_{knife} \times (2.14775 - 0.94243\, M_{knife} + 0.19853 M_{knife}^2)$
28	$M_{\text{sec},28\%} = M_{knife} \times (2.243 - 0.93123\, M_{knife} + 0.17921\, M_{knife}^2)$
31.5	$M_{\text{sec},31.5\%} = M_{knife} \times (2.44201 - 1.01501\, M_{knife} + 0.18244\, M_{knife}^2)$
34.6	$M_{\text{sec},34.6\%} = M_{knife} \times (2.9026 - 1.40115\, M_{knife} + 0.26923\, M_{knife}^2)$

Table 10-5:Correlation functions close to the zero error points of the rectangular three-mode subclass using various clip-levels.

10.7 Appendix G

Analytical Mathematica Program

```
cls = 13.5                    (*clip-level of slit*)
clk = 16                      (*clip-level of knife-edge*)
drs = 0.2                     (*lower range for slit search*)
urs = 2.5                     (*upper range for slit search*)
sk = 3                        (*position for knife search*)
steps = 1                     (*number of full calculations*)
For[i = 0, i < steps,         (*for loop*)
 Clear[aa, bb, cc, dd, ee, ff, tt, ss, uu, vv, ww, xx, kk,
  sa, sb, sc, sd, se, sf, ned, pp, smr, sr, temp, kp, hh, ii, jj, kw, kr];
                              (*clears variables*)
 tt = Random[];               (*Random weights of pure modes*)
 ss = Random[];
 uu = 0;
 vv = 0;
 ww = 0;
 xx = 0;
```

$$aa = tt * \frac{\left(\text{HermiteH}\left[0, \sqrt{2}\, x\right]\right)^2 * e^{-2x^2}}{\int_{-\infty}^{\infty} \left(\text{HermiteH}\left[0, \sqrt{2}\, x\right]\right)^2 * e^{-2x^2}\, dx};$$

(*muliplies random weight by energy normailsed pure Hermitian modes*)

$$bb = ss * \frac{\left(\text{HermiteH}\left[1, \sqrt{2}\, x\right]\right)^2 * e^{-2x^2}}{\int_{-\infty}^{\infty} \left(\text{HermiteH}\left[1, \sqrt{2}\, x\right]\right)^2 * e^{-2x^2}\, dx};$$

$$cc = uu * \frac{\left(\text{HermiteH}\left[2, \sqrt{2}\, x\right]\right)^2 * e^{-2x^2}}{\int_{-\infty}^{\infty} \left(\text{HermiteH}\left[2, \sqrt{2}\, x\right]\right)^2 * e^{-2x^2}\, dx};$$

$$dd = vv * \frac{\left(\text{HermiteH}\left[3, \sqrt{2}\, x\right]\right)^2 * e^{-2x^2}}{\int_{-\infty}^{\infty} \left(\text{HermiteH}\left[3, \sqrt{2}\, x\right]\right)^2 * e^{-2x^2}\, dx};$$

$$ee = ww * \frac{\left(\text{HermiteH}\left[4, \sqrt{2}\, x\right]\right)^2 * e^{-2x^2}}{\int_{-\infty}^{\infty} \left(\text{HermiteH}\left[4, \sqrt{2}\, x\right]\right)^2 * e^{-2x^2}\, dx};$$

$$ff = xx * \frac{\left(\text{HermiteH}\left[5, \sqrt{2}\, x\right]\right)^2 * e^{-2x^2}}{\int_{-\infty}^{\infty} \left(\text{HermiteH}\left[5, \sqrt{2}\, x\right]\right)^2 * e^{-2x^2}\, dx};$$

```
 kk = Simplify[aa + bb + cc + dd + ee + ff];
                              (*Add the randomised modes together in a linear superposition
                                and simplies the function → this is th enrgy density function*)
```

```
sa = FindMinimum[-kk, {x, 3}];                    (*Finds the local maximum values of the
                                                  energy density function *)
sa = -sa[[1]];
sb = FindMinimum[-kk, {x, 2.5}];
sb = -sb[[1]];
sc = FindMinimum[-kk, {x, 2}];
sc = -sc[[1]];
sd = FindMinimum[-kk, {x, 1.5}];
sd = -sd[[1]];
se = FindMinimum[-kk, {x, 0.5}];
se = -se[[1]];
sf = FindMinimum[-kk, {x, 0.1}];
sf = -sf[[1]];
ned = Max[sa, sb, sc, sd, se, sf];                (*finds the overall maximum value*)
pp = (ned)^-1 * kk;                               (*normalises the energy density function *)
```

$$\text{smr} = \sqrt{\left(4 * \left(\int_{-\infty}^{\infty} (aa + bb + cc + dd + ee + ff) * x^2 \, dx\right) \Big/ \left(\int_{-\infty}^{\infty} (aa + bb + cc + dd + ee + ff) \, dx\right)\right)};$$

```
                                                  (*finds the second moment radius*)
Print[smr]; (*prints the second moment  radius*)
```

$$\text{sr} = \text{FindRoot}\left[\text{pp} - \frac{\text{cls}}{100} == 0, \{x, 1.4, \text{drs}, \text{urs}\}, \text{MaxIterations} \to 50\right];$$

```
(*finds the slit radius*)
temp = x /. sr[[1]];                              (*extracts the value from the Mathematica output*)
If[temp < 0, sr = -temp, sr = temp];              (*ensures that the slit radius is positive*)
Plot[pp, {x, -urs, urs}];                         (*plots the normalised energy density function*)
Print[sr];                                        (*prints the slit radius*)
```

$$\text{kp} = \int_{-\infty}^{p} (aa + bb + cc + dd + ee + ff) \, dx;$$

```
                                                  (*knife-edge integrates the energy density function*)
hh = ReplaceAll[kp, p → 1000];                    (*finds the maximum normalising value*)
ii = ReplaceAll[kp, p → -p];                      (*reverse the orientation of the knife-edge integrated energy function*)
jj = hh^-1 * ii;                                  (*normalises the knife-edge integrated energy function*)
```

$$\text{kw} = \text{FindRoot}\left[\text{jj} - \frac{\text{clk}}{100} == 0, \{p, \text{sk}\}\right];$$

```
                                                  (*find the position where the knife-edge clip-level which
                                                  intersects the knife-edge integrated energy graph*)
kr = 2 * p /. kw[[1]];                            (*extracts the value from the Mathematica output
                                                  and multiplies it by two to obtain the knife-edge radius*)
Plot[jj, {p, -urs, urs}]; (*plots the normalised knife-edge energy distribution*)
Print[kr];                                        (*prints the knife-edge radius*)
Print[i];                                         (*prints the iteration number calculation*)

PutAppend[smr, "filesecondmoment"];               (*Appends the second moment radius to a file*)
PutAppend[sr, "fileslit"];                        (*Appends the slit radius to a file*)
PutAppend[kr, "fileknife"];                       (*Appends the knife-edge radius to a file*)
, i++]                                            (*Closes for loop*)
```

Typical output

```
13.5
16
0.2
2.5
3
1
1.43036
```

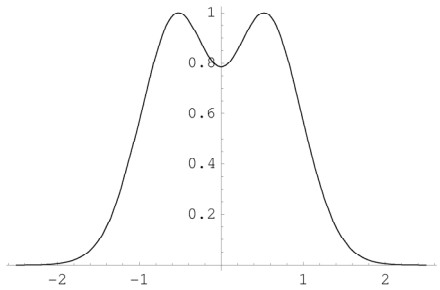


```
1.42343
```

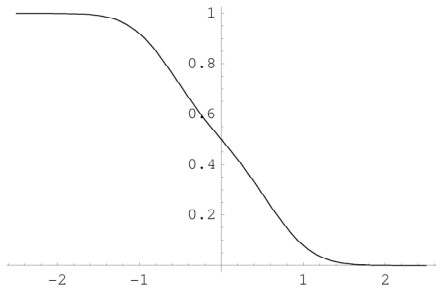


```
1.53969
1
```

10.8 Appendix H

k factor intensity based radii

In Equations (3.19) and (3.20) both the Hermitian and Laguerre polynomials are functions of $x/w_{00}(z)$. Consider for instance now a node or zero intensity point of an arbitrary higher order mode. The position of this node can be found by setting the appropriate polynomial equal to zero. One could therefore find a solution for position *x* of this node that depends directly on $w_{00}(z)$. The beam profile also scales with $w_{00}(z)$ as it propagates. But according to Equations (3.31) and (3.32) the second moment radii are also directly dependent or scale with $w_{00}(z)$. The relationship between the position of the node and the second moment radius is therefore also constant for the specific beam as it propagates. Because the shape of the

beam profile is constant and scales with $w_{00}(z)$ it will also be true for all other intensity points.

k factor energy based radii

It is even simpler to prove that a constant factor *k* exists between energy based and second moment radii. Appendix A gives the normalised energy or knife-edge distributions of the rectangular modes, which are all functions of x/w_{00} . One would solve each of these for a specific value between 0 and 0.5 (the clip level) to obtain half the beam energy radius. (this is because they are centred on zero). Any beam energy radius therefore scales with $w_{00}(z)$ which in turn scales with the second moment radius. The value of k is therefore also constant for energy radii as the beam propagates.

Bibliography

[1] Aguilera, J.A., Aragon, C., et al., 1998. Plasma shielding effects in laser ablation of metallic samples and its influence on LIBS analysis. *Applied surface science,* 127-129, pp 309-314.

[2] Amarande, S.A., 1996. Beam propagation factor and the kurtosis parameter of flattened Gaussian beams. *Optics Communications.* 129, pp 311-317.

[3] Cutolo, A., Allesandra, E., et al., 1992. Characterization of the transverse modes in a laser beam: analysis and application to a q-switched Nd:YAG laser. *Applied Optics,* 31 (15), pp 2722-2733.

[4] Arnaud, J.A., Hubbard, W.M., et al., 1971. Technique for fast measurement of Gaussian laser beam parameters. *Applied Optics,* 10 (12), pp 2775-2776.

[5] Baida, L., Hong, M., 2000. A comparative study of elegant and standard Hermite-Gaussian beams. *Optics Communications,* 174, pp 99-104.

[6] Belanger, P.A., 1991. Beam propagation and the ABCD ray matrices. *Optics Letters,* 16 (4), pp 196-198.

[7] Bridges, W.B., 1975. Divergence of high order Gaussian modes. *Applied Optics,* 14 (10), pp 2346-2347.

[8] Carter, W.H., 1980. Spot size and divergence for Hermite Gaussian beams of any order. *Applied Optics,* 19, pp 1027-1029.

[9] Coherent, 2004. *Beam Diagnostic Cameras* [online]. Available from: http://www.coherent.com/Products/index.cfm?fuseaction=Interfaces.Product&PCID=4&PLID=23&PDID=268 [Accessed 19 October 2004].

[10] Roundy, C.B., 1996. Laser beam quality characterization. *In* CLEO LEAP June 1996, Anaheim CA., Copyright 1996 by Optical Society of America.

[11] Corsi, M., Cristoforetti, G., et al., 2004. Three-dimensional analysis of laser induced plasmas in single and double pulse configuration. *Spectrochimica Acta Part B*, 59 (2), pp 729-735.

[12] Crystran UV-Visible-IR specialist Optics, 2004. *Germanium (Ge) data sheet*, [online]. Available from http://www.crystran.co.uk/germdata.htm [Accessed 20 October 2004].

[13] Crystran UV-Visible-IR specialist Optics, 2004, *Zinc Selenide (ZnSe) data sheet*, [online]. Available from http://www.crystran.co.uk/znsedata.htm [Accessed 20 October 2004].

[14] Diso, D., Perrone, M.R., et al., 1999. Beam width measurements of asymmetric multi-mode laser beams. *Optics & Laser Technolog.*, 31, pp 411-418.

[15] Encinas-Sanz, F., Calderon, O.G., et al., 1999. Measurement of the spatiotemporal dynamics of simple transverse patterns in a pulsed transversely excited CO_2 laser. *Physical review A*, 59 (6), pp 4764-4772.

[16] Encinas-Sanz, F., Serna, J., et al., 2001. Time-resolved spatial profile of TEA CO_2 laser pulses: influence of the gas mixture and intrcavity apertures. *Journal of the Optical Society of America A*, 18 (7), pp 1731-1740.

[17] Encinas-Sanz, F., Serna, J., et al., 1998. Time-varying beam quality factor and mode evolution in TEA CO_2 laser pulses. *Journal of Quantum Electronics*, 34 (10), pp 1835-1838.

[18] Eppich, B., Gao, C., et al., 1998. Determination of the ten second order intensity moments. *Optics & Laser Technology*, 30 , pp 337-340.

[19] Fox, A.G., Li, T., 1963. Modes in a Maser Interferometer with Curved and Tilted Mirrors. *Proceedings of the IEEE*, pp 80-89.

[20] Gao, C., Weber, H., 2000. The problems with M^2. *Optics and Laser Technology*, 32 , pp 221-224.

[21] Goldsborough, J.P., 1964. Beat frequencies between modes of a concave-mirror optical resonator. *Applied Optics*, 3 (2), pp 267-275.

[22] Goswami, A., 1992. Quantum Mechanics. Wm.C.Brown Publishers.

[23] Hodgson, N., Weber, H., 1997. Optical Resonators: fundamentals, advanced concepts and applications, Springer-Verlag.

[24] ISO 11146, 1999. Lasers and Laser related equipment-Test methods for laser beam parameters-Beam widths, divergence angle and beam propagation factor, International Organisation for Standardisation.

[25] Johnston, T. F., 1998. Beam propagation (M^2) measurement made as easy as it gets: the four cuts method. *Applied Optics*, 37 (21), pp 4840-4850.

[26] Johnston, T.F., Siegman, A.E., et al, 1992. Laser beam quality versus aperture size in a cw argon-ion laser. *Optics Letters*, 17 (3), pp 198-200.

[27] Johnston, T.F., Sasnett, M.W., et al, Measurement of “standard” beam diameters Coherent Instruments Division, Auburn Ca USA.

[28] Katrich, A.B., 2002. Shape invariance parameters in laser beam diagnostics. *Optics Communications*, 211, pp 9–14.

[29] Kogelnik, H., Li, T., 1966. Laser Beams and Resonators. *Applied Optics*, 5 (10), pp 1550-1567.

[30] Martinez, C., Encinas-Sanz, F., et al., 1997. On the Parametric characterization of the transversal spatial structure of laser pulses. *Optics Communications*, 139 , pp 299–305.

[31] Mejias, P. M., Martinez-Herrero, R., 1995. Time resolved spatial parametric characterization of pulsed light beams. *Optics Letters*, 20 (7), pp 660-662.

[32] Melles Griot Optics Guide, 2002, *Aberrations , Spherical Aberration* , [online] Availible from: http://www.mellesgriot.com/products/optics/fo_3_2_1.htm, [Accessed 20 October 2004].

[33] Milonni, P.W., Eberley, J.H., 1988. Lasers, John Wley & Sons.

[34] Nemoto, S., Makimoto, T., 1979. Generalized spot size for a higher-order beam mode. *Journal of the Optical Society of America* ,69 , pp 578-580.

[35] Piche, M., Lavigne, P., 1983. Modes of resonators with internal apertures. *Applied Optics*, 22 (13) , pp 1999-2006.

[36] Popov, E.P., 1990. Engineering Mechanics of Solids, Prentice Hall.

[37] Rigrod, W.W, 1983. Diffraction loss of stable optical resonators with internal limiting apertures. *IEEE Journal of Quantum Electronics*, 19 (11), pp 1679-1685.

[38] Saghafi, S., Sheppard, C.J.R., et al, 2001. Characterising elegant and standard Hermite-Gaussian beam modes. *Optics communications*, 191, pp 173–179.

[39] Salamon, T. I., 1998. Technical note, Apertures in laser resonator.

[40] Sam's Laser FAQ, 2004. *Carbon dioxide Lasers* [online]. Available from: http://repairfaq.ece.drexel.edu/sam/laserco2.htm#co2typ0 [Accesed 19 October 2004].

[41] Sanderson, R. L., Streifer, W., 1969. Comparison of laser mode calculations. *Applied Optics*, 8 (1), pp 131-136.

[42] SDI homepage, 2002. *Scientific Development and Integration* [online]. Avalable from: http://www.sdi.co.za [Accessed 20 October 2004].

[43] Serna, J., Martinez-Herrero, R., et al., 1991. Parametric characterization of general partially coherent beams propagating through ABCD optical systems. *Journal of the Optical Society of America A*, 8 (7), pp 1094-1098.

[44] Siegman, A.E., 1973. Hermite-Gaussian functions of complex arguments as optical beam eigen functions. *Journal of the Optical Society of America*, 63, pp 1093.

[45] Siegman, A.E, 1986. Lasers, University Science Books.

[46] Siegman, A. E., 1991. Choice of Clip-levels for Beam Width Measurements Using Knife-Edge Techniques. *IEEE Journal of Quantum Electronics*, 27 (4), pp 1098-1104.

[47] Soukieh, M., Abdul Ghani, B., et al., 1999. Mathematical modelling of TE CO_2 laser with SF_6 as a saturable absorber. *Optics & Laser Technology*, 31, pp 601-611.

[48] Spiricon, 1996. *Laser beam quality characterization* [online]. Available from: http://www.spiricon.com/techinfo/publications/scientific/laser_beam_quality_characterization.shtml [Accessed 19 October 2004].

[49] Spiricon, 2003. *Advanced PC propagation Analyzer* [online]. Available from: http://www.spiricon.com/techinfo/product_data/analizer_instruments/m2_beam_propagation_analizer/m2-200.shtml [Accessed 19 October 2004].

[50] Spiricon, 2003. *Pyrocam III Enhanced Pyroelectric Camera for IR & UV Laser Beam Diagnostics and Thermal Imaging* [online]. Available from: http://www.spiricon.com/selectionguide/scientific_technology/cameras/pyrocamiii.shtml [Accessed 20October 2004].

[51] Stafast, H., Schmid, W.E., et al. 1977. Absorption of CO_2 laser pulses at different wavelengths by ground-state and vibrationally heated SF_6, *Optics Communications*, 21**,** pp 121-126.

[52] Wolfram Research Inc, 1999. *Hermite polynomial*. [online]. Availible from: http://mathworld.wolfram.com/HermitePolynomial.html [Accessed 20 ctober 2004].

[53] Wolfram Research Inc, 1999. *Laguerre polynomial*. [online]. Availible from: http://mathworld.wolfram.com/LaguerrePolynomial.html [Accessed 20 October 2004].

[54] Yasuzi, S., Atsushi, T., 1977. Measurement of the Gaussian laser beam divergence. *Applied Optics*, 16 (6), pp 1481-1482.

[55] Yasuzi, S., Atsushi, T., 1975. Measurement of the mm sized radius of Gaussian beam using the scanning knife-edge. *Applied Optics*, 14 (12), pp 2809-2810.

[56] Zheng, J., Shengzi, Z., et al., 2001. Measurement of beam quality factor (M^2) by slit-scanning method. *Optics &Laser Technology*, 33, pp 231-217.